ANKARA YILDIRIM BEYAZIT UNIVERSITY

GRADUATE SCHOOL OF NATURAL AND APPLIED SCIENCES



FABRICATION OF SnO_2/p-Si HETEROSTRUCTURES FOR UV PHOTODETECTOR AND PHOTOVOLTAIC APPLICATIONS

Ph.D. Thesis by

Kenan ÖZEL

Department of Energy Systems Engineering

January, 2022

ANKARA

FABRICATION OF SnO_2/p-Si HETEROSTRUCTURES FOR UV PHOTODETECTOR AND PHOTOVOLTAIC APPLICATIONS

A Thesis Submitted to

The Graduate School of Natural and Applied Sciences of

Ankara Yıldırım Beyazıt University

In Partial Fulfillment of the Requirements for the Degree of Doctor of Philosophy in Energy Systems Engineering, Department of Energy Systems Engineering

by

Kenan ÖZEL

January, 2022

ANKARA

Ph.D. THESIS EXAMINATION RESULT FORM

We have read the thesis entitled **"FABRICATION OF SnO_2/p-Si HETEROSRUCTURES FOR UV PHOTODETECTOR AND PHOTOVOLTAIC APPLICATIONS"** completed by **KENAN ÖZEL** under the supervision of **PROF. DR. ABDULLAH YILDIZ** and we certify that in our opinion it is fully adequate, in scope and in quality, as a thesis for the degree of Ph.D.

Prof. Dr. Abdullah YILDIZ

Supervisor

Prof. Dr. Fahrettin GÖKTAŞ

Jury Member

Prof. Dr. Adem TATAROĞLU

Jury Member

Prof. Dr. İlhan KOŞALAY

Jury Member

Prof. Dr. Hüseyin CANBOLAT

Jury Member

Prof. Dr. Sadettin ORHAN

Director

Graduate School of Natural and Applied Sciences

ETHICAL DECLARATION

I hereby declare that, in this thesis which has been prepared in accordance with the Thesis Writing Manual of Graduate School of Natural and Applied Sciences,

- All data, information and documents are obtained in the framework of academic and ethical rules,
- All information, documents and assessments are presented in accordance with scientific ethics and morals,
- All the materials that have been utilized are fully cited and referenced,
- No change has been made on the utilized materials,
- All the works presented are original,

and in any contrary case of above statements, I accept to renounce all my legal rights.

Date: **Signature:……..**

Name&Surname:……..

ACKNOWLEDGEMENTS

It is my pleasure to express my deep sense of thanks and sincere gratitude to my supervisor, Prof. Abdullah Yıldız for his valuable guidance, encouragement, and continuous support for my PhD study. With his immense knowledge and vast experience, he encouraged me in every moment of my academic and daily life. It is an honor to work with him, and I will continue to be impressed by his passion for science, and his professional integrity.

I would like to give special thanks to Prof. Fahrettin Göktaş and Prof. Adem Tataroğlu for their useful suggestions and valuable contributions to my PhD thesis as thesis progress committee members.

I would like to express my thanks to Prof. İlhan Koşalay from Ankara University and Prof Hüseyin Canbolat from Ankara Yildirim Beyazit University for being committee members.

I would like to express my thanks to all my colleagues at Ankara Yildirim Beyazit University, especially Abdullah Atılgan and Aycan Atlı, for their supports, technical help and valuable comments.

Finally, I would like to thank my family for their understanding and endless support. Very special thanks to my wife Tuğba and my brother Selim.

January, 2022 **Kenan ÖZEL**

FABRICATION OF SnO_2/p-Si HETEROSTRUCTURES FOR UV PHOTODETECTOR AND PHOTOVOLTAIC APPLICATIONS

ABSTRACT

Developing a low-cost and high-performance UV photodetector is critically substantial for various applications in military and for civilian purposes. In recent years, numerous efforts have been devoted to accomplishing UV photodetectors based on wide band gap metal-oxide semiconductor/Silicon (Si) heterojunctions. Due to its superior optical and electrical properties, SnO_2 has attracted tremendous attention for the fabrication of *p*-*n* heterostructure-based optoelectronic devices. The aim of enhanced light harvesting and improving light-material interaction has prompted us to develop the SnO_2/*p*-Si *p*-*n* heterostructure-based UV photodetectors with nanostructures integration.

Herein, *n*-SnO_2 (Nanostructured)/*n*-SnO_2 (thin film)/*p*-Si heterostructures are designed to fabricate p-n heterojunction based optoelectronic devices. The characterization results reveal that the architecture of the devices plays a decisive role in UV photodetector and photovoltaic behavior of the produced devices. The critical performance parameters of the devices are calculated to evaluate the light-sensing performance of the devices. The best performing device exhibits an admirably high photo-responsivity of 43.91 A/W, a large detectivity of $2.66x10^{13}$ Jones, and an extremely low power consumption of $3.76x10^{-14}$. As for the photovoltaic performance, the device with SnO_2 thickness of 391 nm exhibits the best power conversion efficiency (*PCE*) of 3.09%.

Ultimately, this thesis work has revealed a route for the fabrication of *n*-SnO_2/*p*-Si heterostructures for UV photodetectors and photovoltaic cell applications. The experimental results are interpreted in all aspects and the thesis is completed by presenting the further modifications to improve the performance of the devices.

Keywords: Heterojunctions, UV photodetectors, Nanostructures, Solar cells.

UV FOTODEDEKTÖR VE FOTOVOLTAİK UYGULAMALAR İÇİN SnO_2/p-Si HETEROYAPILARIN ÜRETİLMESİ

ÖZ

Düşük maliyetli ve yüksek performanslı bir UV fotodetektörü geliştirmek, askeri ve sivil amaçlı çeşitli uygulamalar için kritik öneme sahiptir. Son yıllarda, geniş bant aralıklı metal oksit yarı iletken/Silikon (Si) heteroeklemlerine dayalı UV fotodedektörlerini gerçekleştirmek için çok çaba sarf edilmiştir. Üstün optik ve elektriksel özelliklerinden dolayı SnO_2, *p-n* heteroeklem tabanlı optoelektronik cihazların imalatında büyük ilgi görmüştür. Gelişmiş ışık hasadı ve ışık-malzeme etkileşimini iyileştirme amacı, bizi nanoyapı entegrasyonuna sahip SnO_2/p-Si *p-n* heteroeklem tabanlı UV fotodedektörleri geliştirmeye sevk etti.

Burada *n*-SnO_2 (Nanoyapılı)/*n*-SnO_2 (ince film)/*p*-Si heteroyapıları *p-n* heteroeklem tabanlı optoelektronik cihazları imal etmek için tasarlanmıştır. Karakterizasyon sonuçları, cihaz mimarisinin üretilen cihazların UV fotodetektör ve fotovoltaik davranışında belirleyici bir rol oynadığını ortaya koymaktadır. Cihazların ışık algılama performansını değerlendirmek için cihazların kritik performans parametreleri hesaplanmıştır. En iyi performans gösteren cihaz, 43,91 A/W gibi takdire şayan yüksek bir foto-duyarlılık, $2{,}66 \times 10^{13}$ Jones gibi büyük bir dedektiflik ve $3{,}76 \times 10^{-14}$ gibi son derece düşük bir güç tüketimi sergilemiştir. Fotovoltaik performansa gelince, 391 nm SnO_2 kalınlığına sahip cihaz, % 3.09 ile en iyi güç dönüşüm verimini (*PCE*) göstermektedir.

Sonuç olarak, bu tez çalışması, UV fotodedektörleri ve fotovoltaik hücre uygulamaları için *n*-SnO_2/*p*-Si heteroyapılarının üretimi için bir yol ortaya çıkarmıştır. Deneysel sonuçlar tüm yönleriyle yorumlanmış ve cihazların performansını artırmak için ilave modifikasyonlar sunularak tez tamamlanmıştır.

Anahtar Kelimeler: Heteroeklemler, UV fotodedektörler, Nanoyapılar, Güneş Hücreleri.

CONTENTS

Ph.D. THESIS EXAMINATION RESULT FORM ii
ETHICAL DECLARATION iii
ACKNOWLEDGMENTS iv
ABSTRACT v
ÖZ vi
NOMENCLATURE ix
LIST OF TABLES xiii
LIST OF FIGURES xiv

CHAPTER 1-INTRODUCTION 1
CHAPTER 2-THEORETICAL BACKGROUND 6
2.1 Tin oxide (SnO_2) semiconductor 6
2.2 Deposition of SnO_2 semiconductor 7
2.2.1 Formation of SnO_2 thin film with sol-gel spin-coating method 8
2.2.2 Growth of SnO_2 nanostructures with hydrothermal method 8
2.3 SnO2/p-Si heterostructure-based optoelectronic devices 9
CHAPTER 3 FABRICATION AND CHARACTERIZATION 17
3.1 Fabrication of SnO_2/p-Si heterostructure-based optoelectronic devices 17
3.1.1 Experimental steps of the devices 17
3.2 Characterization of the devices 22
3.2.1 Evaluation of the properties of SnO_2 thin films and nanostructures 23
3.2.2 Determination of the UV photo-response and photovoltaic characteristics of the devices 25
CHAPTER 4 RESULTS AND DISCUSSION 28
4.1 Investigation of the effect of seed layer type on the performance of the devices 30
4.2 Optimization of seed layer and hydrothermal deposition 36
4.3 Determination of performance limits of n-SnO_2/p-Si heterostructure-based UV photodetectors 43
4.4 Investigation of the photovoltaic (PV) performance of the devices 50
CHAPTER 5 CONCLUSION 57

REFERENCES 60

NOMENCLATURE

Roman Letter Symbols

ΔE_c	Conduction band offset
ΔE_g	Bandgap energy difference
ΔE_v	Valence band offset
A	Active area
A	Absorbance
A^*	Richardson constant
c	Light velocity
d	Interplanar spacing
D^*	Specific detectivity (Jones)
D_n	Minority carrier electron diffusion coefficient (cm^2/s)
D_p	Minority carrier hole diffusion coefficient (cm^2/s)
E_c	Conduction band
E_f	Fermi energy
E_g	Bandgap energy
E_v	Valence band
EQE	External quantum efficiency
f_{3db}	Frequency at 3 decibels
FF	Fill factor
G	Generation rate of electron-hole pairs
h	Planck's constant
I_d, J_d	Diode current, diode current density
I_{dark}	Dark-current
I_{light}	Light current
I_{max}, J_{max}	Current, current density at maximum power point
I_{ph}	Photo-current
I_s, J_s	Reverse saturation current, reverse saturation current density
I_{sc}, J_{sc}	Short circuit current, short circuit current density
k	Boltzmann's constant

LDR	Linear dynamic range
L_n	Thermal-equilibrium minority carrier electron diffusion length (cm)
L_p	Thermal-equilibrium minority carrier hole diffusion length (cm)
m_e^*	Effective mass of electron
m_h^*	Effective mass of hole
n	Refractive index or ideality factor
N_a	Acceptor concentration
N_c	Effective density of the conduction band
N_d	Donor concentration
N_v	Effective density of the valence band
NEP	Noise equivalent power
n_{po}	Minority electron concentration (cm^{-3})
P_{in}	Illumination power
P_{max}	Maximum power
p_{no}	Minority hole concentration (cm^{-3})
PCE	Power conversion efficiency
PR	Photoresponsivity
PS	Photosensitivity
q	Charge of electron
RR	Rejection Ratio
t	Thickness
T	Temperature
T	Transmittance
t_r	Rise time
t_d	Decay time
V_{bi}	Built-in potential
V_{Dn}	Built-in potentials on the n-side
V_{Dp}	Built-in potentials on the p-side
V_{max}	Voltage at maximum power point
V_{oc}	Open circuit voltage
W	Width of depletion region

Greek Letter Symbols

α	Absorption coefficient, power exponent
δ	Penetration depth
χ_{Si}	Electron affinity of Si
χ_{SnO_2}	Electron affinity of SnO_2
$\mathcal{E}_n$	Dielectric permitivity of n-SnO_2
$\mathcal{E}_p$	Dielectric permitivity of p-Si
θ	Bragg's angle
λ	Wavelength
μ	Electron mobility
ρ	Density
$Ø_{bi}$	Zero-bias barrier height

Acronyms

DIW	Deionized Water
DSSCs	Dye-Sensitized Solar Cells
EDS	Energy Dispersive Spectroscopy
EtOH	Ethanol
HCI	Hydrochloric Acid
HF	Hydrofluoric Acid
MOx	Metal Oxides
NAs	Nanoarrays
NaOH	Sodium Hydroxide
NFs	Nanoflowers
NRs	Nanorods
NsL	Nanostructured Layer
p-Si	p-type Silicon
PV	Photovoltaic
rpm	Revolution per minute
SEM	Scanning Electronic Microscopy
SL	Seed Layer

UV	Ultraviolet
UV-Vis	Ultraviolet-visible
WBG	Wideband gap
XRD	X-Ray Diffractometer

LIST OF TABLES

Table 2.1 List of material properties of SnO_2 semiconductors 6

Table 4.1 Summary of the fabricated device structures 29

Table 4.2 Fabrication characteristics of designed photodetectors..... 32

Table 4.3 Comparison of the diode and photodetection parameters of the fabricated devices..... 35

Table 4.4 The performance parameters of the samples..... 40

Table 4.5 The obtained parameters displayed by each device. 48

Table 4.6 Comparison of calculated parameters of the result of sample (S15) and other reported UV photodetectors..... 50

Table 4.7 Photovoltaic parameters of the cells..... 54

LIST OF FIGURES

Figure 1.1 Schematic representation of the proposed optoelectronic device 4

Figure 2.1 The crystalline structure of SnO_2 unit cell 6

Figure 2.2 The schematic view of spin-coating method 8

Figure 2.3 The schematic view of hydrothermal method 9

Figure 2.4 The working principles of n-SnO_2/p-Si heterostructure-based optoelectronic devices 10

Figure 2.5 The energy-band diagram of the SnO_2/p-Si-based p-n heterojunction in thermal equilibrium 11

Figure 2.6 The ideal I–V curve of a p-n junction 12

Figure 2.7 (a) The linear-scale plotted and (b) the log-scale plotted I-V characteristics of p-n heterostructure-based photodetector under dark and illumination conditions. 13

Figure 2.8 Typical J-V curves of a photovoltaic cell 15

Figure 3.1 Schematic representation of the device and its components 17

Figure 3.2 Fabrication steps for n-SnO_2/p-Si heterostructure-based devices 18

Figure 3.3 Schematics of preparation process of SnO_2 solution 19

Figure 3.4 The schematic representation of p-Si wafer dicing 19

Figure 3.5 The surface cleaning process of diced wafers 20

Figure 3.6 Schematics of SnO_2 thin film fabrication by spin coating method 20

Figure 3.7 The growth of SnO_2 nanostructures by hydrothermal method 21

Figure 3.8 The back-side metallization process and linear I-V relation through the Ag/p-Si interface 21

Figure 3.9 The front-side metallization process and linear I-V relation through the Ag/n-SnO_2 interface 22

Figure 3.10 The schematic of SnO_2/p-Si heterostructure-based optoelectronic device 22

Figure 3.11 a) XRD measurement system b) An example of XRD pattern for SnO_2 film 23

Figure 3.12 a) FE-SEM measurement system b) An example of top-view SEM images of n-SnO_2 (Nanostructured) /n-SnO_2 (thin film) /p-Si 24

Figure 3.13 a) UV-Vis measurement system b) An example of absorbance and transmittance profile of n-SnO_2 (thin film) / glass 25

Figure 3.14 The schematic representation of I-V measurement system 26

Figure 3.15 The schematic representation of I-t measurement system 27

Figure 4.1 The optical transmittance profile of emitter layers of the samples The inset figure shows the Tauc plots to determine the band gap value of samples 33

Figure 4.2 Cross-sectional SEM images of (a) SnO_2 nanostructured layer (NsL)/p-Si, (b) SnO_2 nanostructured layer (NsL)/SnO_2 seed layer (SL)/p-Si, (c) SnO_2 nanostructured layer (NsL)/ZnO seed layer (SL)/p-Si, and (d) SnO_2 nanostructured layer (NsL)/TiO_2 seed layer (SL)/p-Si 34

Figure 4.3 The semi-logarithmic plotted current-voltage (I-V) curves of the devices under dark and UV irradiation conditions. 35

Figure 4.4 Top-surface SEM images of (a) S6, (b) S7, (c) S8, (d) S9, (e) S10, and (f) the cross-sectional SEM image of the device (S7). 38

Figure 4.5 Transmittance spectra for the samples. The inset depicts the Tauc plots to extract the band gap size of samples. 39

Figure 4.6 The log-scale current–voltage (I–V) characteristics for the samples 40

Figure 4.7 The time-dependent photoresponse plots of the devices (S6) and (S7) ... 41

Figure 4.8 The $1/C^2$-V characteristics of S6 and S7 42

Figure 4.9 The energy band alignment of S6 (a) and S7 (b) in thermal equilibrium 43

Figure 4.10 (a) XRD pattern and (b) EDS spectra of the sample (S15) 44

Figure 4.11 SEM micrographs of a) S11, b) S12, c) S13, d) S14, e) S15, and cross-sectional SEM images of the SnO_2 layer (S15). 45

Figure 4.12 The semi-logarithmic current-voltage (I-V) curves of the photodetectors measured under dark and UV irradiation (311 nm) condition. Inset shows the ohmic characteristics between Ag contact and n-SnO_2 46

Figure 4.13 Graph of PR values of the samples with respect to $1/P_{in}$ 47

Figure 4.14 Plot of PR values with respect to α values of the samples 48

Figure 4.15 The transient-response characteristics of the sample (S15). The inset shows the enlarged figure of the response behavior of the sample (S15) 49

Figure 4.16 Top-view and side-view SEM images of n-SnO_2 layer of the cells. 51

Figure 4.17 The absorbance and transmittance profiles of n-SnO_2 (206 nm), n-SnO_2 (304 nm), and n-SnO_2 (396 nm). The inset shows the Tauc plots of the samples 52

Figure 4.18 The dark current-voltage (I-V) plots of the samples 53

Figure 4.19 P-V and I-V characteristics of cells 53

Figure 4.20 $1/C^2$-V graphs of the fabricated devices 54

Figure 4.21 Energy band diagram of n-SnO_2/p-Si heterojunction based solar cell under equilibrium condition. 55

CHAPTER 1

INTRODUCTION

Photodetectors (PDs) are devices that work similar to the working principles of the human eye, perceive light signals, and convert the perceived light signals into electrical signals. These devices can detect lights in different spectrum depending on the characteristics of their architecture and components. For instance, the term "UV photodetector" describes photodetectors designed to detect the ultraviolet (UV) spectrum. Detection of short wavelength and high energy photons falling into the UV region is critical for a wide range of applications such as environmental surveillance, flame sensing, sterilization of biological and chemical substances, engine monitoring, national defense, and optical communication [1-2]. In the last decade, the development of metal-oxide-based low-cost high-performance *p-n* heterojunction UV photodetectors has attracted great attention as it will provide great convenience for military and commercial applications, as well as detect and monitor UV radiation that has hazardous effects on human health [3]. According to the International Commission on Illumination, the UV radiation spectrum is divided into three main categories: UV-A ($400 > \lambda > 320$ nm), UV-B ($320 > \lambda > 280$ nm), and UV-C ($280 > \lambda > 200$ nm) [4]. As visible spectrum covers the wavelengths from 400 to 700 nm, PDs with a cut-off wavelength shorter than 400nm are called ‘visible-blind’ [5].

Over the years, UV PDs have been designed in a variety of device structures, such as the *p-n* homojunction, the *p-n* heterojunction, Schottky junction, the metal-semiconductor-metal junction, etc. [6]. Among them, the *p-n* heterostructure-based UV PDs have become core component of continuous research for new-generation electronic and optoelectronic devices thanks to their simple and low-cost fabrication process [7]. Taking advantage of intrinsic visible-blind sensitivity and high radiation resistance, the *p-n* heterojunctions designed by coating wideband gap (WBG) semiconductors onto Silicon (Si) provide a promising approach for precise detection of UV radiation [8].

WBG semiconductors such as TiO_2 [9,10] ZnO [11,12] and SnO_2 [13,14] are extensively preferred for developing various optoelectronic devices and can be coated in high-quality with affordable coating techniques [15–17]. Amongst WBG semiconductors, SnO_2 has become the focus of intense research thanks to the outstanding properties, such as large band gap value of 3.5-4 eV, high chemical and radiation hardness, and low resistance. Therefore, it has been widely employed for gas sensing [18-20], thin-film transistors [21], solar cells [22], supercapacitors [23], and photo-catalyst [24]. To date, SnO_2 thin film and nanostructures have been deposited on a wide range of substrates, including silicon wafers, glass slides, conductive oxide layers via various methods, such as hydrothermal method [25], spray pyrolysis [18], sputtering [26], pulsed laser deposition [27], sol-gel spin coating [28], and chemical vapor deposition [29]. In particular, hydrothermal method and sol-gel spin coating technique offers superior homogeneity, fabrication simplicity and low-cost production [30].

Up to now, a number of investigations have been reported to present the fabrication of optical and electronic devices having SnO_2 layer. Nagatomo et al. produced Al/SnO_2/*n*-Si solar cells and investigated the effects of current- voltage (*I*-*V*), capacitance-voltage (*C*-*V*) characteristics, interface states and series resistance on the performance of these devices [31]. Persin et al. achieved to fabricate SnO_2/*n*-Si heterojunction based solar cell exhibiting open circuit voltage (V_{oc}) of 0.450 V and short circuit current (I_{sc}) of 6 mA [32]. They suggested that the photovoltaic performance of the devices would be improved by applying mesh-shaped front contact to SnO_2 and using thicker SnO_2 films with lower layer resistance. Altındal et al. discussed the role of density of interface states and resistance values on the performance of Al/SnO_2/*p*-Si Schottky diodes [33].

Liu et al. reported the fabrication of gas sensors based on nanostructured SnO_2 thin film. The fabricated sensors were highly sensitive and fast-responding with a sensitivity of 1075 to 500 ppm ethanol vapor [29]. Ling et al. achieved to obtain SnO2 thin film-based gas sensors for monitoring of alcohol vapor [34]. Juybari et al. designed p-n and p-i-n heterojunctions based on metal oxides including *n*-SnO_2, *i*-ZnO, and *p*-NiO [35]. They investigated the effects of annealing and intrinsic layer

on the properties of p-n heterojunctions. Maleki et al. reported to fabricate SnO_2/Si heterojunction-based diodes by depositing SnO_2 thin films on mono- and poly-crystalline silicon substrates under different deposition temperatures [36]. Their findings showed that samples with SnO_2/mono-c Si architecture had lower resistivity than samples with SnO_2/poly-c Si architecture at high deposition temperature.

Zheng et al. reported the fabrication of flexible UV photodetectors based on ZnO-SnO_2 nanoarrays [37]. Recent progresses on SnO_2-based perovskite solar cells were summarized by Jiang et al., highlighting the wonderful potential of SnO_2 as an electron transport layer for such devices [38]. Dimarco et al. compared the photoelectric conversion performance of SnO_2-Based Dye-Sensitized Solar Cells (DSSCs) with TiO_2-Based DSSCs [39]. They made recommendations to improve the performance of SnO2-based DSSCs.

As mentioned before, there are many reported investigations on *n*-SnO_2/*p*-Si heterojunctions in literature, but most of them have focused on the structural, optical, and electrical properties of the aforementioned semiconductors and their heterojunctions rather than the device performance of SnO_2/*p*-Si structure [40-41]. The performance of any photodetectors depends upon the device structure and light-matter interaction, as well as the properties of semiconductor layers. Generally, tailoring the properties of emitter layer such as thickness, morphology, architecture etc. promotes the detection capacity of *p*-*n* heterostructure-based devices. Moreover, the enhanced light-matter interaction can be achieved by the integration of nanostructures of metal oxide semiconductors into the device structure.

The aim of this thesis is to fabricate low-cost and high-performance UV photodetectors with *n*-SnO_2(Nanostructured)/*n*-SnO_2(thin film)/*p*-Si heterostructure whose architecture are designed by nanostructures for the first time in the literature. Figure 1.1 illustrates the schematic representation of the proposed photodetector.

Although there are many reports in the literature about the formation of SnO_2 thin film by sol-gel spin coating and the growth of SnO_2 nanostructures via hydrothermal method, the growth of SnO_2 nanostructures on SnO_2 thin film has rarely been studied. In fact, a UV photodetector designed by constructing these layers on a p-

type silicon substrate has not been found. In addition, it has been reported that the growth mechanism of a nanostructured layer is affected by the nature of the seed layer. In the light of these information, we gained motivation to design optoelectronic devices having structure of *n*-SnO_2(Nanostructured)/*n*-SnO_2(thin film)/*p*-Si.

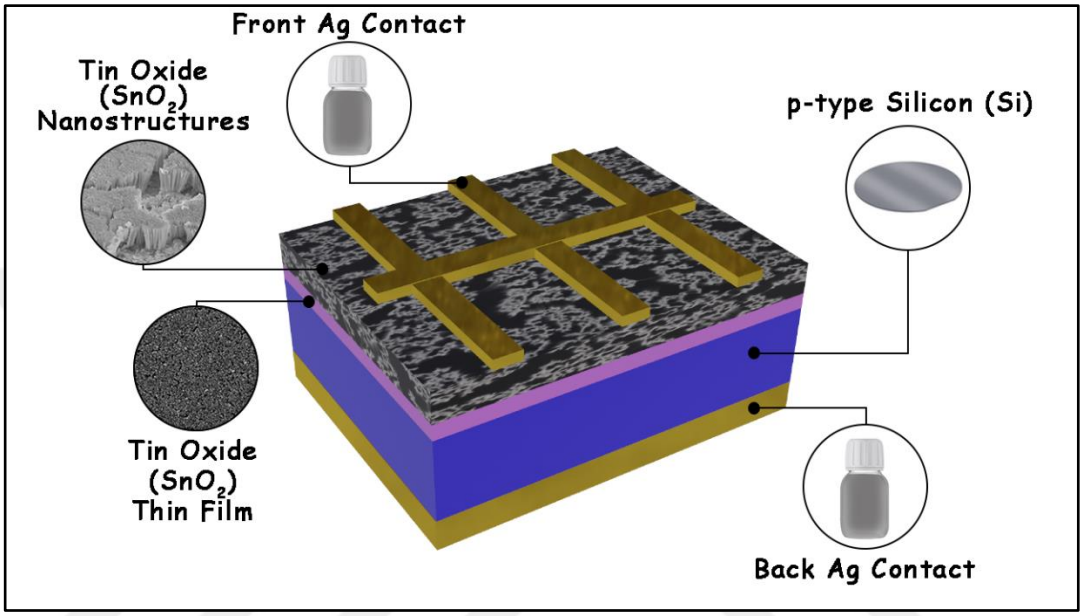


Figure 1.1 Schematic representation of the proposed optoelectronic device

The remainder of this thesis is organized as follows:

In Chapter 2, the properties, and applications of tin oxide (SnO_2) semiconductor, deposition techniques for SnO_2 thin films and nanostructures and the basic concepts of SnO_2/*p*-Si heterostructure-based optoelectronic devices are introduced for gaining in-depth insight into the SnO_2/*p*-Si heterostructure-based ultraviolet (UV) photodetectors. Then, the detail of light-matter interaction, the diagram of energy-band alignment, the ideal current-voltage (*I*-*V*) characteristics of a *p*-*n* junction are described to explain the working principles of *n*-SnO_2/*p*-Si heterostructure-based photodetectors. Finally, the performance parameters of photodetectors and solar cells are given to evaluate the light harvesting performance of any photodetectors or solar cells.

In Chapter 3, the fabrication and characterization of *n*-SnO_2/*p*-Si heterostructure-based optoelectronic devices are handled in two sub-topics as: the fabrication

processes of proposed optoelectronic device and the characterization techniques for SnO_2 semiconductor and fabricated optoelectronic devices.

In chapter 4, results and discussions are presented to assess the performances of fabricated optoelectronic devices and to compare them with their reported counterparts. In addition, the effect of experimental parameters on the performances of fabricated devices are investigated in terms of structural and optoelectrical aspects. Ultimately, a route is proposed to fabricate low-cost and high-performance UV photodetectors and heterojunction based solar cells.

In Chapter 5, all results are comprehensively evaluated. The results are interpreted in all aspects and the thesis is completed by presenting the further modifications to improve the performance of *p-n* heterostructure-based devices.

CHAPTER 2

THEORETICAL BACKGROUND

2.1 Tin oxide (SnO_2) semiconductor

Tin oxide (SnO_2) is a direct bandgap semiconductor crystallizing the tetragonal rutile structure, as delineated in Figure 2.1. In this structure, Sn atoms are situated at the center of a distorted octahedral consisting of O atoms [42].

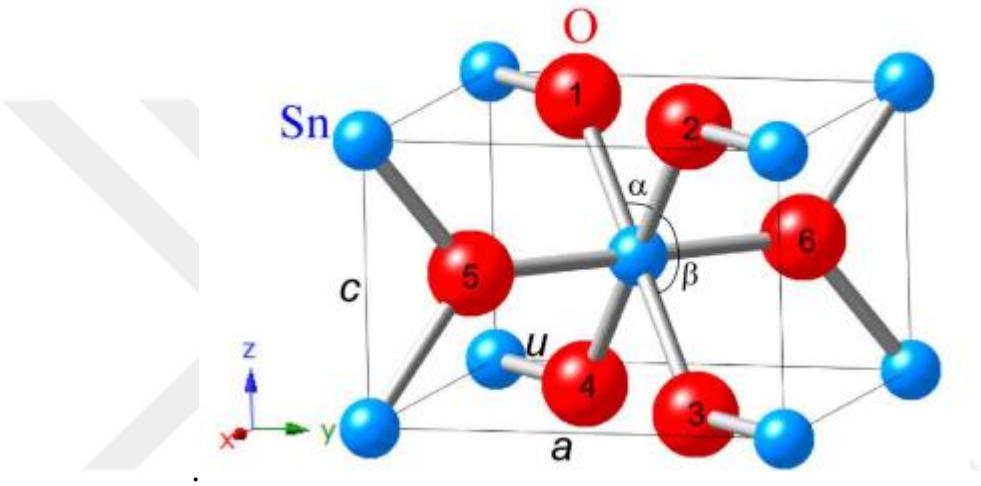


Figure 2.1 The crystalline structure of SnO_2 unit cell [43].

SnO_2 is an attractive semiconductor with wide band gap (3.5-4.6 eV), high electron mobility, strong exciton binding energy [44-48]. Table 2.1 lists the material properties of SnO_2 semiconductors.

Table 2.1 List of material properties of SnO_2 semiconductors

Property	Unit	Value	Refs
Density (ρ)	kg/m^3	6990	[49]
Electron mobility (μ)	$cm^2/(V{\cdot}s)$	23-106	[50]
Thermal conductivity (K)	W/(m·K)	0.98-17.5	[51]
Resistivity	Ω·cm	1-100	[52]
Electron affinity (χ)	eV	4.53	[53]
Relative permitivity (Ɛ)	F/m	9.86	[54]

Among all the metal oxides, SnO_2 metal oxide semiconductors stand out as promising material thanks to their enthralling chemical, thermal, optical, and electrical properties [55]. Therefore, they are widely employed in the production of many optical and electronic devices, including displays [56], bio-sensing devices [57], protective coatings [57], anti-reflective coatings [59], chemical sensors [60], solar cells [47], window heaters [61], diodes [62], photodiodes [63], and photodetectors [64].

The structural, electrical, and optical properties of SnO_2 semiconductors are varied depending on the deposition method, the deposition conditions of the method, the type and number of doping atoms. In particular, the intrinsic n-type characteristics of SnO_2 semiconductor can be tuned by extrinsic dopants. In this regards, antimony (Sb), niobium (Nb), and tantalum (Ta) are commonly utilized dopant materials to improve the n-type characteristics [65]. Apart from SnO2 thin films, SnO_2 nanostructures and nanoparticles can be utilized in the design of different types of optoelectronic devices. One dimensional SnO2 nanostructures, such as nanowires, nanoarrays, nanobelts, nanorods, and nanotubes are attracting particular interest thanks to their promising optical and electrical properties [66]. These nanostructures, with their large surface areas and improved transport characteristics endow the devices with superior optoelectrical properties. Additionally, SnO_2 nanoparticles can be used in sensor-based applications, providing an effective approach to improve the sensitivity of the devices [67].

2.2 Deposition of SnO_2 semiconductor

Until now, a number of deposition techniques such as sputtering [68], spray pyrolysis [69], chemical vapor deposition [70], vacuum evaporation [71], dip coating [72], spin coating [73], and hydrothermal method [74] have been used for the growth of film and nanostructures of SnO_2. Among these methods, the sol-gel spin coating and hydrothermal method offer some superiorities such as moderate deposition condition, homogenous and uniform growth, scalability, and low-cost production [30]. Utilizing these methods, n-SnO2 layers of optoelectronic devices can be effectively grown with reproducible quality. Therefore, the emitter layers of the p-n junction-based

devices can be produced repeatedly with high structural uniformity in large-scale production.

2.2.1 Formation of SnO_2 thin film with sol-gel spin-coating method

Spin-coating is a route to obtain a thin film on a substrate. The spin coating process is usually carried out by dropping the solution onto the surface of the sample rotating at low speed or not rotating at all, and then spreading it by rotating at high speed. The schematic of spin-coating method is shown in Figure 2.2. In this method, the thickness of the film depends on some experimental conditions such as the amount of dropped solution, solution molarity, spin speed, spin acceleration time, and rotation time [75].

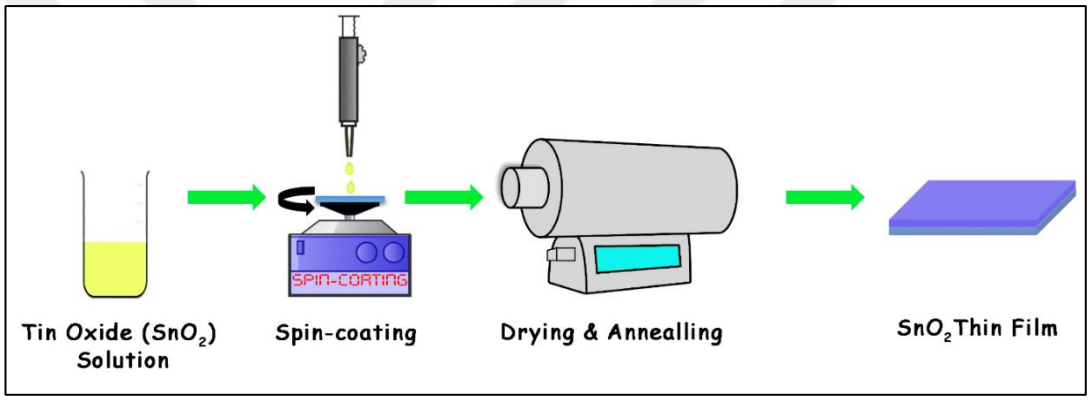


Figure 2.2 The schematic view of spin-coating method.

2.2.2 Growth of SnO_2 nanostructures with hydrothermal method

Hydrothermal deposition method has been employed to grow different morphologies of the nanostructures, including such as nanoarrays (NAs), nanorods (NRs), and nanoflowers (NFs) etc. This method is performed in a hydrothermal autoclave under a certain temperature and pressure reaction condition for a specified time. Figure 2.3 represents the schematic of hydrothermal growth process. In this method, the morphology of the nanostructures can be tailored by optimizing the reaction parameters such as hydrothermal solution, temperature, reaction duration etc. [76]. Moreover, the deposition of seed layer underneath the nanostructured layer promotes the uniform growth of nanostructures [77].

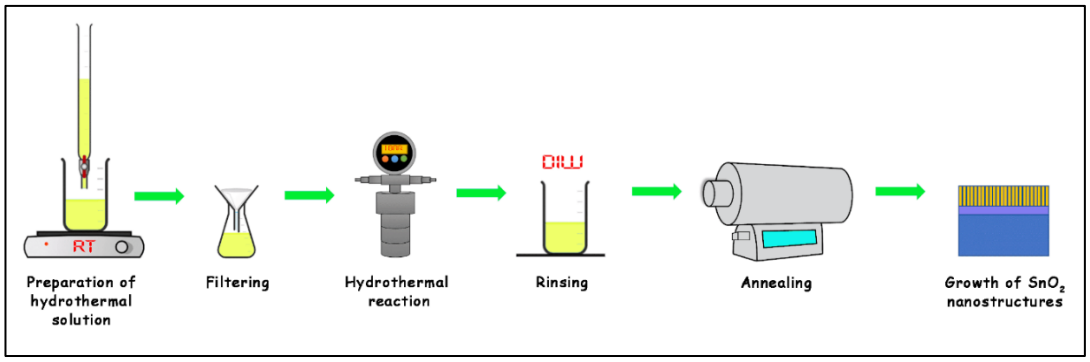


Figure 2.3 The schematic view of hydrothermal method.

2.3 SnO_2/p-Si heterostructure-based optoelectronic devices

In the last decade, *n*-SnO_2/*p*-Si heterojunctions have been widely used to manufacture optoelectronic devices, including solar cells, photodiodes, photodetectors, and thin- film transistors [78-81]. Unlike *p-n* homojunctions, composed of bringing together similar semiconductor material, the *p-n* heterojunctions are usually created by combining different semiconductor materials. Simply, a *p-n* heterojunction is obtained by coating metal oxide semiconductor on top of a different semiconductor layer. To fabricate SnO_2/*p*-Si based *p-n* heterojunctions, SnO_2 thin films and/or nanostructures can be grown on *p*-Si substrate to form the *n*-type layer of the *p-n* heterostructure-based devices. When *n*-SnO_2 and *p*-Si semiconductors are placed together, the depletion region formed at the interface acts like a semi-permeable membrane, affecting the carrier transport mechanisms of the device.

Figure 2.4 displays the working principles of *n*-SnO_2/*p*-Si heterostructure-based optoelectronic devices. When the light impinges on the *n*-SnO_2/*p*-Si heterojunction, the photons might be absorbed or transmitted through the semiconductor layers. Provided that the energy of incident photon is greater than the bandgap of semiconductor layer, the photon can be absorbed, enabling the generation of electron-hole pairs. For the *n*-SnO_2/*p*-Si based *p-n* heterojunctions, the low wavelength photons can be absorbed by *n*-SnO_2, while the remaining photons pass through *n*-SnO_2 and are absorbed by *p*-Si. Afterwards, the photogenerated electron-hole pairs can be separated thanks to the built-in electric field at the interface of *n*-SnO_2 and *p*-Si. Finally, the separated electrons and holes are extracted from the *p-n*

heterostructure-based device with metal contacts to obtain the electric current in an external circuit. For the case of UV irradiation, the UV sensing performance of the SnO_2/*p*-Si based *p*-*n* heterojunction can be enhanced by tuning the electrical and optical properties of SnO_2 layer. Apart from its role as an *n*-type semiconductor layer, *n*-SnO_2 can also be used as an anti-reflection coating layer thanks to the refractive index (n=2.33-2.80) close to the optimal refractive index (n_{opt}=2.1) value required for a layer deposited between air and *p*-Si [82]. In case of solar irradiation, the main part of the solar spectrum is absorbed by p-Si layer, so the p-Si layer is called the absorber layer. Absorption, separation, and collection processes play a pivotal role in determining the power conversion efficiency of the solar cells.

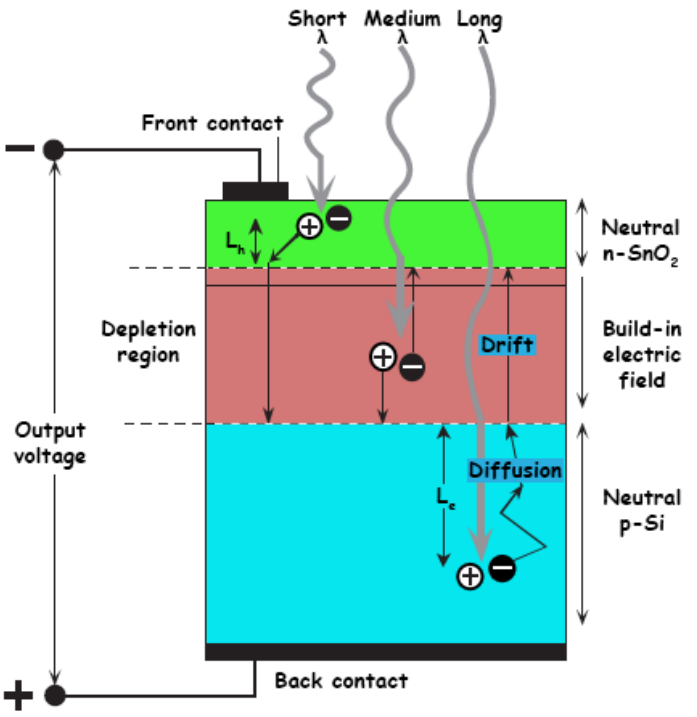


Figure 2.4 The working principles of *n*-SnO_2/*p*-Si heterostructure-based optoelectronic devices.

The performance of any *p*-*n* heterostructure-based device depends significantly on the energy band alignment of the *p*-type and *n*-type semiconductor layers. The staggered gap (Type II) band alignment between semiconductor interfaces provides an advantage for high performance by promoting the separation, and transportation of photogenerated electron-hole pairs [83]. Figure 2.5 illustrates the energy-band diagram of the SnO_2/*p*-Si-based *p*-*n* heterojunction in thermal equilibrium.

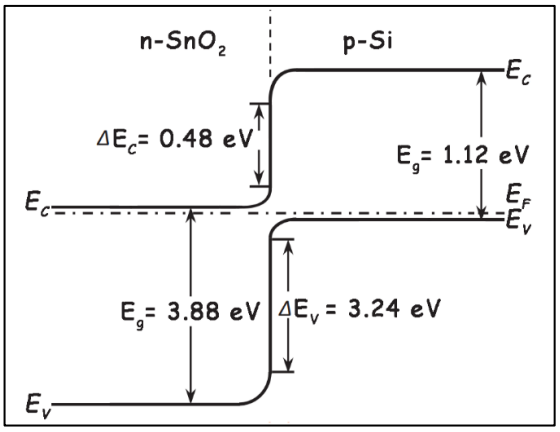


Figure 2.5 The energy-band diagram of the SnO_2/*p*-Si-based *p-n* heterojunction in thermal equilibrium

As observed in Figure 2.5, the combination of *n*-SnO_2 and *p*-Si semiconductors is suitable for achieving type II energy band alignment. The conduction and valence band energies on both sides of the heterojunction can curve up or down within the vicinity of heterointerface. This phenomenon, known as band bending, plays an important role in the separation of electron-hole pairs, and its depth can be calculated by solving the Poisson's equation [84]. Also, the difference in valence and conduction band energies and bandgap values of both semiconductors cause conduction band (ΔE_c) and valence band discontinuities (ΔE_v). The values of ΔE_c and ΔE_v can be calculated based on the equations (2.1) and (2.2), respectively [85].

$$\Delta E_c = \chi_{SnO_2} - \chi_{Si} \tag{2.1}$$

$$\Delta E_v = (\chi_{SnO_2} + E_{g_{SnO2}}) - (\chi_{Si} + E_{g_{Si}}) \tag{2.2}$$

where χ_{SnO_2} and χ_{Si} are the electron affinity of *n*-SnO_2 and *p*-Si, respectively. $E_{g_{SnO2}}$ and $E_{g_{Si}}$ are the band-gap of *n*-SnO_2 and *p*-Si, respectively. The values of χ_{SnO_2} , χ_{Si}, and $E_{g_{Si}}$ are known to be 4.53 eV, 4.05 eV and 1.12 eV from the literature [86].

Let us now take a closer look at the current-voltage (*I-V*) characteristics of any *p-n* junction based devices. If an external driver power is applied to the *p-n* heterojuncion, the equilibrium condition is disturbed and the electric current starts to flow through the device depending on the transport characteristics of the charge carriers and the connection terminals of the external source. The total current (*I*)

passing through the *p-n* heterojunction under dark condition is expressed by the diode characteristics [84].

$$I = I_s \left[exp\left(\frac{qV}{nk_BT}\right) - 1 \right] \quad (2.3)$$

where I_s, V, n, k_B, and T refer to the reverse saturation current, the applied voltage, ideality factor, Boltzmann's constant, and temperature. Herein, I_s is defined as [84]:

$$I_s = AA^*T^2 \exp\left(\frac{-q\emptyset_{bi}}{k_BT}\right) \quad (2.4)$$

where A, A^*, and $\emptyset_{bi}$ stand for the active area, Richardson constant, and the zero-bias barrier height, respectively. There are mainly two types of transport mechanisms through a *p-n* junction-based semiconductor device, which are drift and diffusion. The dominant transport mechanism of photodetectors is diffusion. Hence, for the ideal *I–V* relationship of a *p-n* junction, the reverse saturation current (I_s) can be written as the following [87]:

$$I_s = qA\left[\frac{D_p}{L_p}p_{no} + \frac{D_n}{L_n}n_{po}\right] \quad (2.5)$$

where D is the diffusion coefficient (cm^2/s), L is the diffusion length (cm), and subscript p and n indicate that they belong to hole and electron, respectively. Under equilibrium condition, n_{po} is the minority electron concentration (cm^{-3}), and p_{no} is the minority hole concentration (cm^{-3}). The ideal *I–V* curve of a *p-n* junction is shown in Figure 2.6.

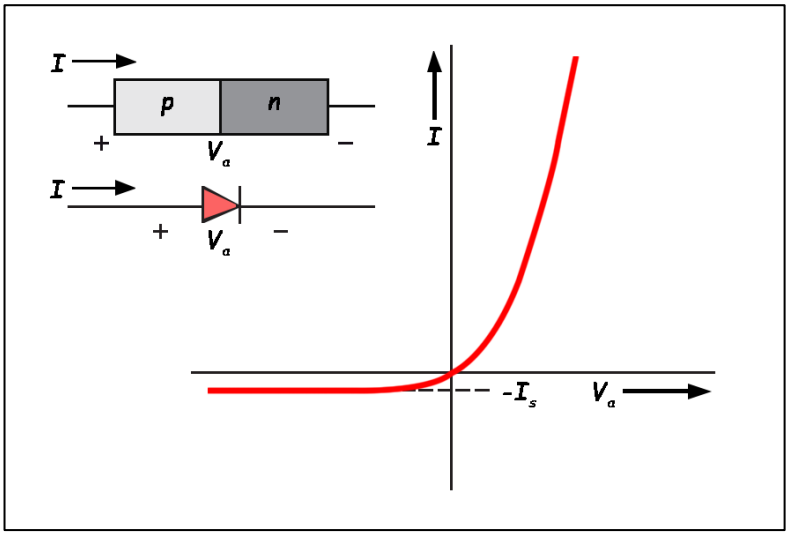


Figure 2.6 The ideal *I–V* curve of a p-n junction

Under illumination condition, the concentration of minority carriers starts to heighten noticeably. Due to strong dependence of the recombination-generation rate on the depletion layer width, the increase in the concentration of minority carriers becomes evident thanks to the increased depletion width for the case of reverse bias. Therefore, the operating characteristics of *p-n* heterostructure-based photodetectors are examined under the reverse bias condition. Figure 2.7 (a)-(b) depict the linear-scale and the log-scale plotted *I-V* characteristics of *p-n* heterostructure-based photodetector under dark and illumination conditions.

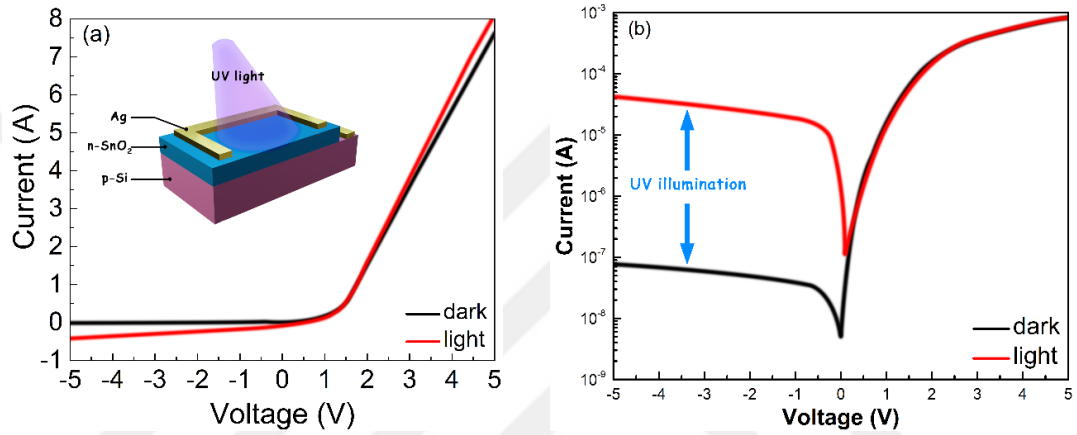


Figure 2.7 (a) The linear-scale plotted and (b) the log-scale plotted *I-V* characteristics of *p-n* heterostructure-based photodetector under dark and illumination conditions.

Let us now focus on important parameters that are used to characterize the sensing performance of photodetectors. The light detection performance of any photodetector is quantified by photo-sensitivity (*PS*), photo-responsivity (*PR*), spesific detectivity (*D**), external quantum efficiency (*EQE*), noise equivalent power (*NEP*), and rejection ratio (*RR*). In addition, the response speed of any photodetector to the changes in the status of incident light source (on/off) is evaluated by the rise time (t_r) and the decay or fall time (t_d) [88].

* Photo-sensitivity (*PS*) can be defined as the ratio of photo-current (I_{ph}) to dark-current (I_{dark}) at a certain value of reverse applied bias. It is expressed as [89]:

$$PS = \frac{I_{ph}}{I_{dark}} \qquad (2.6)$$

* Photo-responsivity (*PR(ƛ)*) defines the generation of photo-current (I_{ph}) as a function of illumination power (P_{in}) at a specific value of wavelenght. It is given by [89]:

$$PR = \frac{I_{ph}}{P_{in}\,A} = \frac{I_{light} - I_{dark}}{P_{in}\,A} \quad (A/W) \tag{2.7}$$

*Specific detectivity (*D**) characterizes the smallest detectable signal and input signal-noise relationship. It is defined by [89]:

$$D^* = \frac{PR\sqrt{A}}{\sqrt{2qI_{dark}}} \quad (Jones) \tag{2.8}$$

* External quantum efficiency (*EQE (ƛ)*) quantifies the efficiency of converting incident light into electrical signals at a given wavelength . It is determined as [90]:

$$EQE\ (\lambda) = \frac{hc}{q\lambda} PR_{\lambda} x 100\% \tag{2.9}$$

* Noise equivalent power (*NEP*) is expressed as the signal power that yields a signal-to-noise ratio at an output bandwidth of one hertz. The lower the value of *NEP*, the better the device detection performance. It is represented by [89]:

$$NEP = \frac{\sqrt{2qI_{dark}}}{PR_{\lambda}} \quad (W/Hz^{\frac{1}{2}}) \tag{2.10}$$

* Rejection ratio (*RR*) is a measure of the spectral sensitivity of any photodetector. For the case of UV photodetectors, it is defined as the ratio of ultraviolet photo-responsivity to visible photo-responsivity. It can expressed by [91]:

$$RR_{UV/Vis} = \frac{PR_{UV}}{PR_{Vis}} \tag{2.11}$$

*The rise time (t_r)/decay time (t_d) characterize the response speed of a photodetector. t_r/t_d is the time taken by photo-current to change from 10% to 90% or vica versa. The rise time (t_r) can also be estimated from the photodetector frequency response, in this case it is calculated using the 3 dB bandwidth. The formula is given by [92]:

$$t_r \cong \frac{0.35}{f_{3db}}\ (s) \tag{2.12}$$

Typical current density-voltage (*J-V*) curves of a photovoltaic cell are given in Figure 2.8, showing the change in current values with respect to the applied voltage to the device under dark and solar illumination conditions. While the *J-V* characteristics of a photodetector is drawn in the third quadrant, the *J-V* characteristics of a photovoltaic cell is drawn in the fourth quadrant [93-94]. This characteristic curve shows us that a photovoltaic cell produces a current without applying any external voltage, or produces a voltage without transferring any current to an external circuit. In conclusion, it can be said that a photovoltaic cell works as a power source while a photodetector works as a receiver or sensor.

If the fabricated heterojunctions exhibits good photovoltaic behavior, then important key parameters, the maximum power (P_{max}), the short circuit current density (J_{sc}), and the open circuit voltage (V_{oc}) can be determined to assess the photovoltaic characteristics of the devices. In addition, the values of fill factor (*FF*) and power conversion efficiency (*PCE*) of a solar cell can be calculated by utilizing these parameters [87].

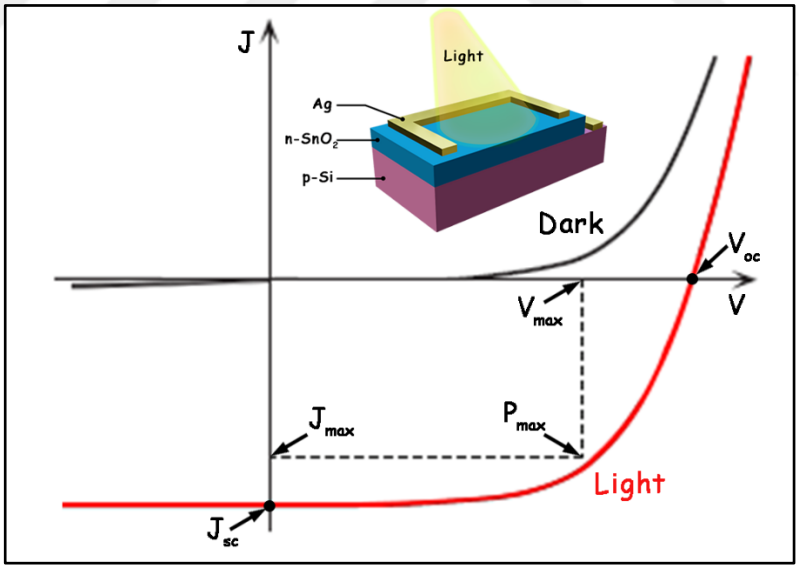


Figure 2.8 Typical J-V curves of a photovoltaic cell

* The maximum power (P_{max}) is the peak electrical output that a photovoltaic cell can deliver under illumination condition. The values of current density and voltage at the maximum power point (MPP) are given as J_{max} and V_{max}, respectively [87].

* The short-circuit current density (J_{sc}) is the parameter obtained by dividing the short circuit current (I_{sc}) produced in the photovoltaic cell by the cell area. I_{sc} is a area-dependent parameter and corresponds to the current flowing through a photovoltaic cell when the terminals of the cell is short circuited. J_{sc} values of the photovoltaic cells are directly related to the optoelectronic properties of the devices [87].

* The open circuit voltage (V_{oc}) corresponds to the voltage obtained when the terminals of the cell is open circuited. Multiple factors including temperature, leakage current and bandgap values of the devices, etc., significanty affect the V_{oc} values [87].

* Fill factor (*FF*) is a measure of quality of any photovoltaic cell. Even though the value of *FF* is unity for an ideal case (rectangular shape), but it is inevitable to deviate from unity due to the exponantial behavior of *p-n* junction. It is defined as the ratio of maximum power to theoretical power. It can expressed by [95]:

$$FF = \frac{V_{max} \times J_{max}}{V_{oc} \times J_{sc}} = \frac{P_{max}}{V_{oc} \times J_{sc}} \qquad (2.13)$$

* Power conversion efficiency (*PCE*) is a measure of the photovoltaic performance of any solar cell. It is defined as the ratio of is defined as the ratio of the electrical power output (P_{max}) to the optical power in (P_{in}). For reliable measurement of the photovoltaic performance of the cells, the measurements should be performed under standard test conditions (AM1.5, P_{in} =1000 W/m^2 or 100 mW/cm^2, T=25 °C) It is represented by [95]:

$$PCE\ (\%) = \frac{V_{oc} \times J_{sc} \times FF}{P_{in}} \times 100 \qquad (2.14)$$

CHAPTER 3

FABRICATION AND CHARACTERIZATION

3.1 Fabrication of SnO_2/*p*-Si heterostructure-based optoelectronic devices

To manufacture the *p*-*n* junction of the *n*-SnO_2/*p*-Si heterojunction based optoelectronic device shown in Figure 3.1, the spin coating method was employed to coat the *n*-SnO_2 thin film known as the seed layer on *p*-Si substrate. Herein, SnO_2 seed layer improves the growth of *n*-SnO_2 nanostructures, in addition to the role of *n*-type layer of the device structure, and also ensures the homogeneous distribution of the nanostructures by forming a buffer layer between the *n*-SnO_2 nanostructured layer and *p*-Si. Throughout this thesis, the manufacturing process was optimized to fabricate high performance *n*-SnO_2/*p*-Si heterojunction based optoelectronic devices.

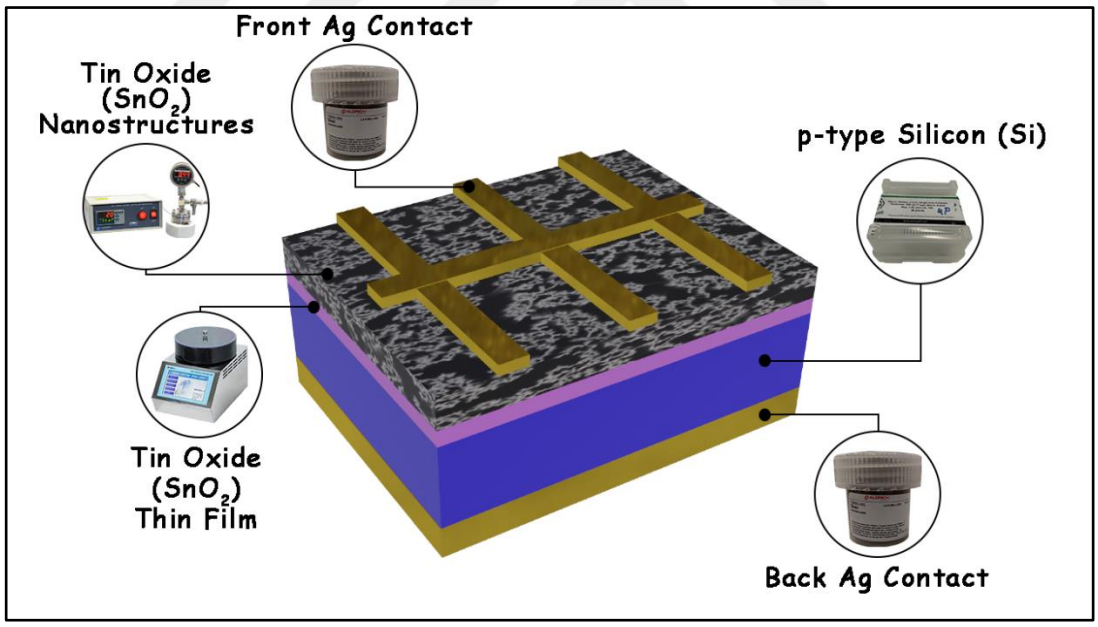


Figure 3.1 Schematic representation of the device and its components

3.1.1 Experimental steps of the devices

The fabrication steps followed to produce SnO_2/*p*-Si heterostructure-based devices by the integration of SnO_2 nanostructures are presented in Figure 3.2.

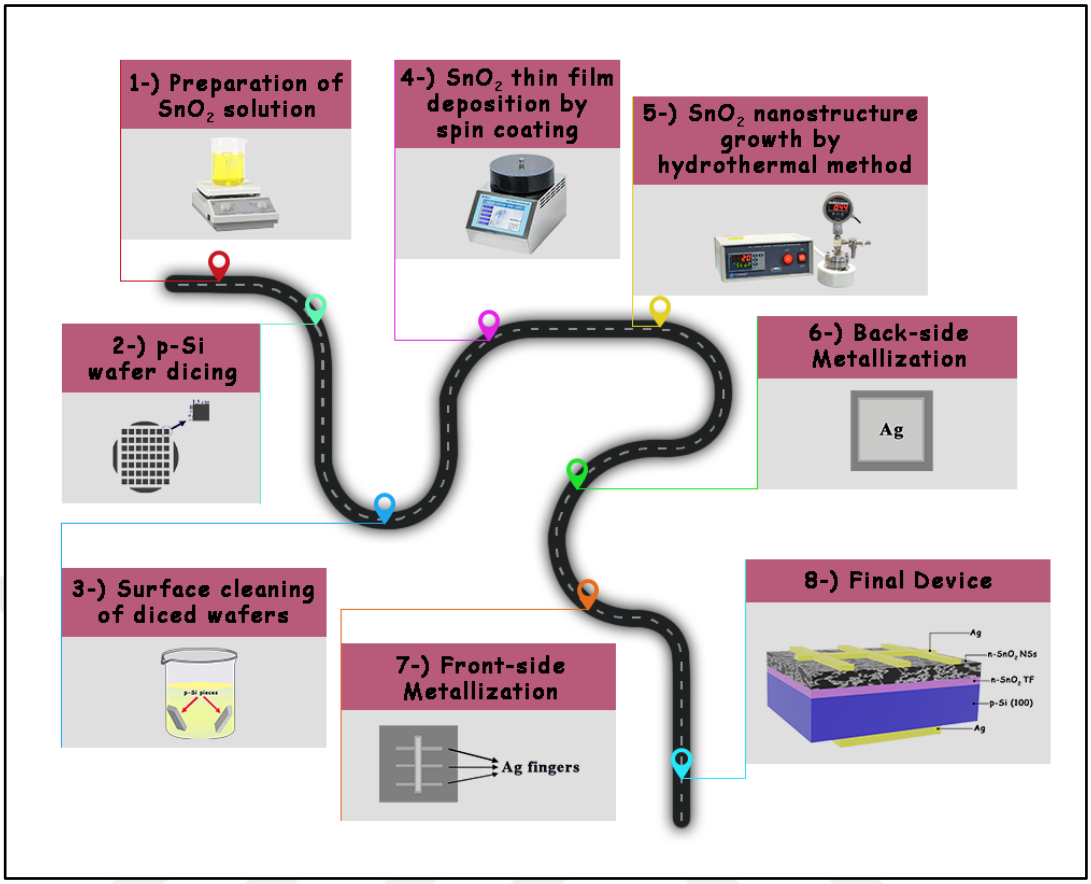


Figure 3.2 Fabrication steps for *n*-SnO_2/*p*-Si heterostructure-based devices

i) Preparation of SnO_2 solution

Tin(II) chloride dihydrate ($SnCl_2 \cdot 2H_2O$) and ethanol (C_2H_5OH) were used for the preparation of SnO_2 seeding solution. After dissolving 3.348 g of tin(II) chloride dihydrate in 40 ml of ethanol, the prepared mixture was stirred at 80°C for 2 hours in a closed vessel. After opening vessel, solvent was evaporated to obtain powder. Finally, the obtained powder was again dissolved in 20 ml of ethanol and stirred at 50°C for 2 hours to obtain SnO_2 seeding solution [96]. Figure 3.3 schematically shows the preparation process of the SnO_2 solution.

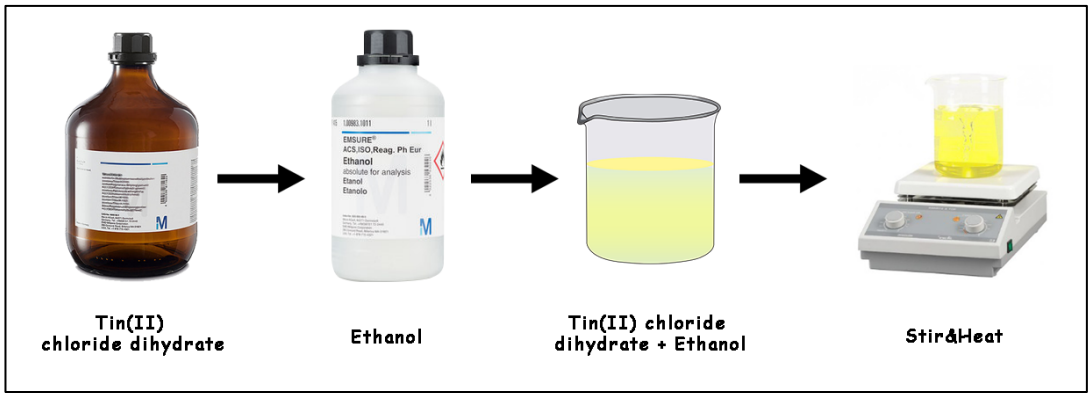


Figure 3.3 Schematics of preparation process of SnO_2 solution

ii) p-Si wafer dicing

p-type Silicon (Si) wafers having 525 μm thickness were diced to obtain square pieces of 1.5 x 1.5 cm^2. Figure 3.4 shows the schematic representation of *p*-Si wafer dicing using a diamond scribe.

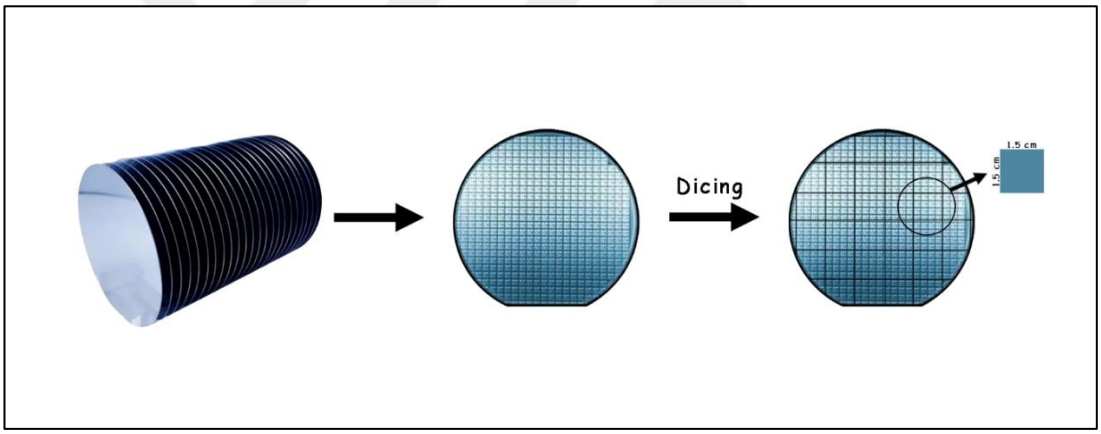


Figure 3.4 The schematic representation of *p*-Si wafer dicing

iii) Surface cleaning of diced wafers

The removal of surface contaminations of Si wafers is crucial task to eliminate the possibility of defects in the devices to be produced. Firstly, diced *p*-Si wafers were cleaned with piranha solution prepared by mixing 30 ml of sulfuric acid (H_2SO_4) and 10 ml of hydrogen peroxide (H_2O_2) and left at 80°C for 15 minutes. Following the immersion process in piranha solution, the samples were rinsed with deionized water (DIW). Afterwards, they were again immersed in hydrofluoric acid solution obtained by mixing 1.75 ml of hydrofluoric acid (HF) and 38.3 ml of deionized water for 1 minute. Finally, the samples were again rinsed with deionized water, and then

dried at 150°C for 15 minutes. This cleaning process eliminates the organic contamination and native silicon dioxides from Si pieces as well as makes the surface of the pieces hydrophilic. Figure 3.5 represents the surface cleaning process of diced wafers.

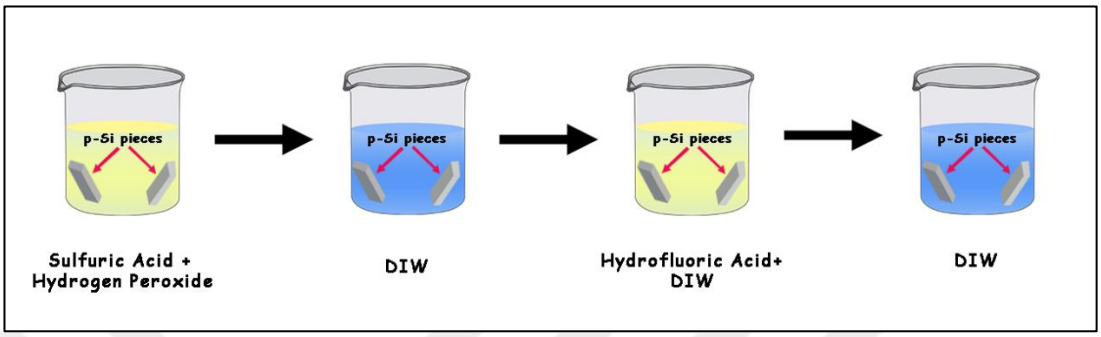


Figure 3.5 The surface cleaning process of diced wafers.

iv) SnO_2 thin film deposition by spin coating

The prepared SnO_2 seeding solution was coated on clean *p*-Si wafers via spin-coating process. The coating process was achieved by two cycles of coating at 2500 rpm spinning speed for 30 seconds. After deposition, the samples were annealed to obtain SnO_2 seed layer. Figure 3.6 shows the schematics of SnO_2 thin film fabrication by spin coating method.

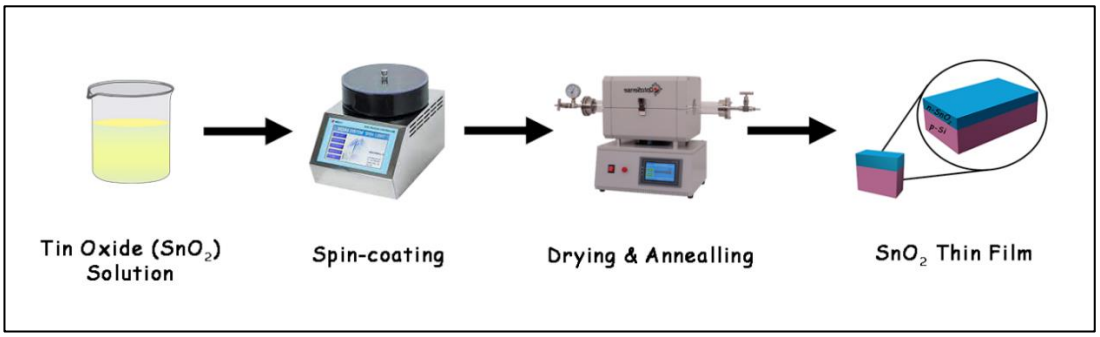


Figure 3.6 Schematics of SnO_2 thin film fabrication by spin coating method.

v) SnO_2 nanostructure growth by hydrothermal method

The growth of nanostructures upon the SnO_2 seed layer coated *p*-Si samples was accomplished by hydrothermal method. After putting the samples into a hydrothermal autoclave, hydrothermal solution was added, and then deposition

process was completed at 95°C for 18 hours. Figure 3.7 shows the schematic representation of the growth of SnO_2 nanostructures by hydrothermal method.

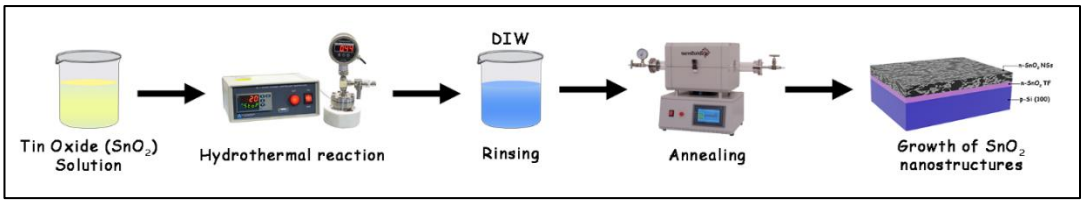


Figure 3.7 The growth of SnO_2 nanostructures by hydrothermal method

vi) Back -side metallization

The formation of ohmic contact between a metal and a semiconductor layer is highly desirable so as not to adversely affect the magnitude of the current extracted from the devices. Here, silver (Ag) conductive paste was screen-printed to the entire back side of *p*-Si substrate. After applying Ag paste onto the back surface of the devices, they were cured at 150°C for 30 minutes. Figure 3.8 demonstrates the back-side metallization process and linear *I-V* relation through the Ag/*p*-Si interface, implying the formation of ohmic contact.

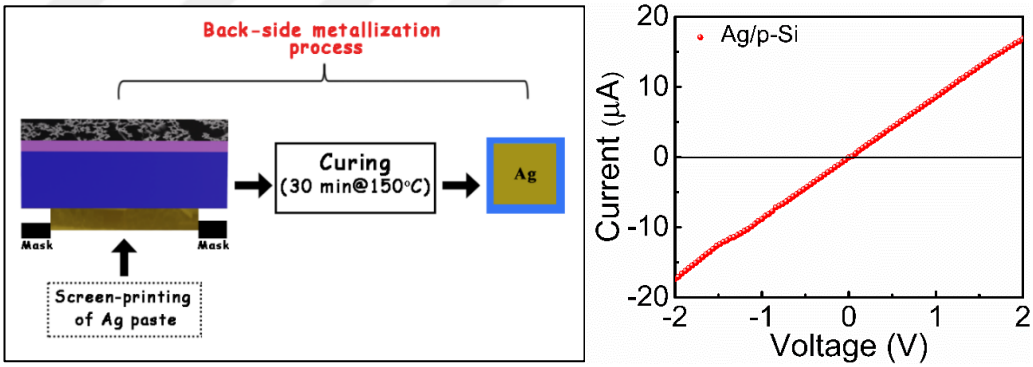


Figure 3.8 The back-side metallization process and linear *I-V* relation through the Ag/*p*-Si interface

vii) Front-side metallization

To complete the device fabrication, silver (Ag) conductive paste was screen-printed to the top of SnO_2 nanostructured layer with a finger-shaped shadowing mask. After applying Ag paste onto the front surface of the devices, they were cured at 150°C for 30 minutes. Figure 3.9 displays the front-side metallization process and linear I-V relation through the Ag/*n*-SnO_2 interface, implying the formation of ohmic contact.

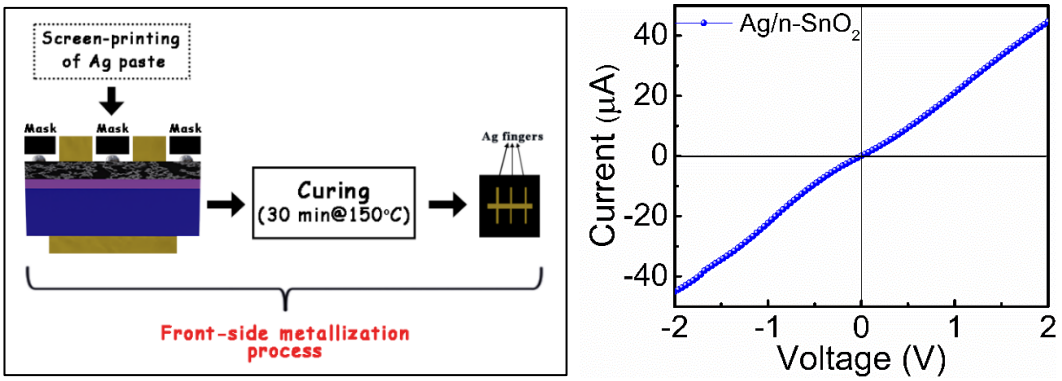


Figure 3.9 The front-side metallization process and linear *I-V* relation through the Ag/*n*-SnO_2 interface.

vii) Final device

Figure 3.10 shows the schematic of SnO_2/*p*-Si heterojunction optoelectronic device produced within the scope of this thesis. As mentioned before, the *n*-SnO_2 layers are responsible for the absorption of the UV spectrum, while the *p*-Si layer is responsible for the absorption of the remaining spectrum.

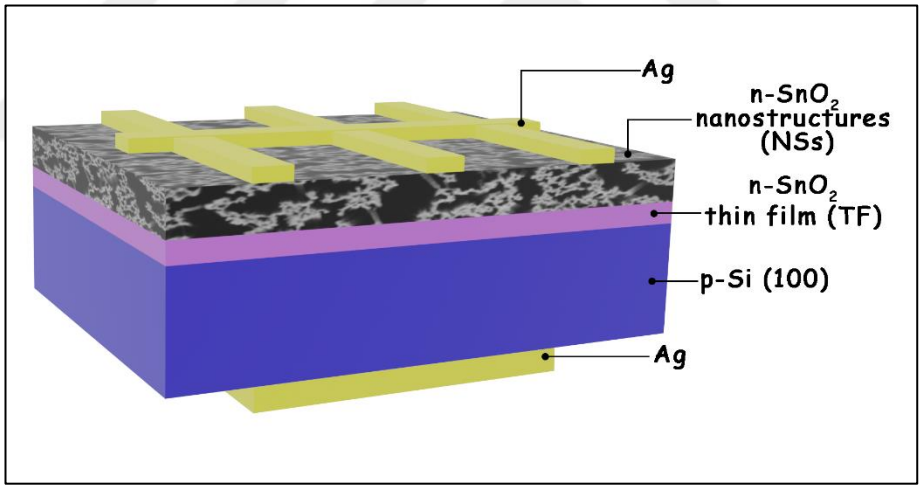


Figure 3.10 The schematic of SnO_2/*p*-Si heterostructure-based optoelectronic device

3.2 Characterization of the devices

The structural properties, surface morphologies , optical profiles of *n*-SnO_2 thin film and SnO_2 nanostructured emitter layer deposited on *p*-Si were characterized with X-ray diffraction (XRD, Rigaku Miniflex 600), Field Emission Scanning Electron Microscope (FE-SEM, Hitachi SU500) and UV-Vis measurements (UV-Vis spectrophotometer, Shimadzu-UV 1700). In addition, the thickness of the deposited

layers is estimated by cross-sectional SEM measurements. The current-voltage (*I-V*) and the time-dependent photoresponse (*I-t*) characteristics of the fabricated devices were determined with a computerized source meter unit and a photoresponse measurement system. The photovoltaic performance of the devices was evauated under simulated solar illumination (Abet Tech., 10500, AM 1.5G, 100mW/cm^2).

3.2.1 Evaluation of the properties of SnO_2 thin films and nanostructures

Herein, the detailed explanation of the characterizations for determining the structural, morphological, and optical properties of the *n*-SnO_2 (thin film)/*p*-Si, *n*-SnO_2 (Nanostructured) /*n*-SnO_2 (thin film) / *p*-Si , and *n*-SnO_2 (thin film)/glass heterostructures were reported.

i) XRD measurements for determining the structural properties

The crystal structure and the crystal quality of *n*-SnO_2 thin film and SnO_2 nanostructured emitter layer were examined by a X-Ray diffraction (XRD, Rigaku Miniflex 600) (Figure 3.11 (a)). The diffraction patterns were recorded and analyzed using PDXL software to determine the crystallinity of the coated layers.

An example of XRD patterns measured for SnO_2 thin films is shown in Figure 3.11 (b). In XRD measurements, the crystal structure and the preferred orientations of the sample are determined by detecting the diffracted lights scattered from the sample in accordance with Bragg's law.

$$n\lambda = 2dsin\theta \qquad (3.1)$$

where n, λ, d and θ denote the order of reflection, the characteristic wavelength of the X-ray (0.1542 nm), the interplanar spacing, and Bragg's angle, respectively [97].

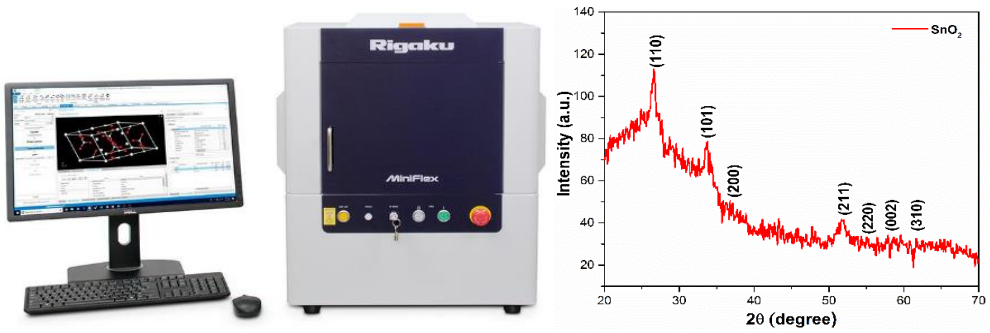


Figure 3.11. a) XRD measurement system b) An example of XRD pattern for SnO_2 film

ii) FE-SEM measurements for determining the morphological properties

The surface morphologies for *n*-SnO_2 (thin film)/*p*-Si, *n*-SnO_2 (Nanostructured) /*n*-SnO_2 (thin film) /*p*-Si heterostructures were analyzed using Hitachi SU5000 Field Emission Scanning Electron Microscope (FE-SEM) (Figure 3.12 (a)). SEM images are obtained by scanning the top-view or side-view of the samples with a focused electron beam. The nanostructure properties, grain size and thickness information of *n*-SnO_2 thin film and SnO_2 nanostructured emitter layer were determined by means of FE-SEM measurements. An example of top-view SEM images of *n*-SnO_2 (Nanostructured) /*n*-SnO_2 (thin film) /*p*-Si is illustrated in Figure 3.12 (b).



Figure 3.12 a) FE-SEM measurement system b) An example of top-view SEM images of *n*-SnO_2 (Nanostructured) /*n*-SnO_2 (thin film) /*p*-Si

iii) UV-Vis measurements for determining the optical properties

The optical absorbance and transmittance profiles of the *n*-SnO_2 (thin film)/ glass, and *n*-SnO_2 (Nanostructured)/*n*-SnO_2 (thin film) /glass samples were evaluated by Shimadzu 1700 double beam UV-Vis spectrophotometer (Figure 3.13 (a)). The bandgap energy (E_g) of the materials and penetration depth (δ (λ)) of the incident light can also be determined by UV-Vis measurements. The bandgap energy (E_g) of the SnO_2 thin films and SnO_2 nanostructured layers can be derived from the absorption-photon energy relationship [98].

$$(\alpha h\nu)^2 = A\left(h\nu - E_g\right) \qquad (3.2)$$

where α indicates the absorption coefficient, $h\upsilon$ indicates the incident photon energy, and A is a constant. In addition, the penetration depth ($\delta\ (\lambda)$) of incident light can be obtained from the absorption coefficient spectrum ($\alpha\ (\lambda)$) [99]

$$\delta\ (\lambda) = \frac{1}{\alpha\ (\lambda)} \tag{3.3}$$

$$\alpha\ (\lambda) = \left(\frac{1}{t}\right) ln\left(\frac{1}{T}\right) \tag{3.4}$$

where t and T is the thickness and transparency of coated layers. An example of optical profile of n-SnO_2 (thin film)/ glass are given in Figure 3.13 (b).

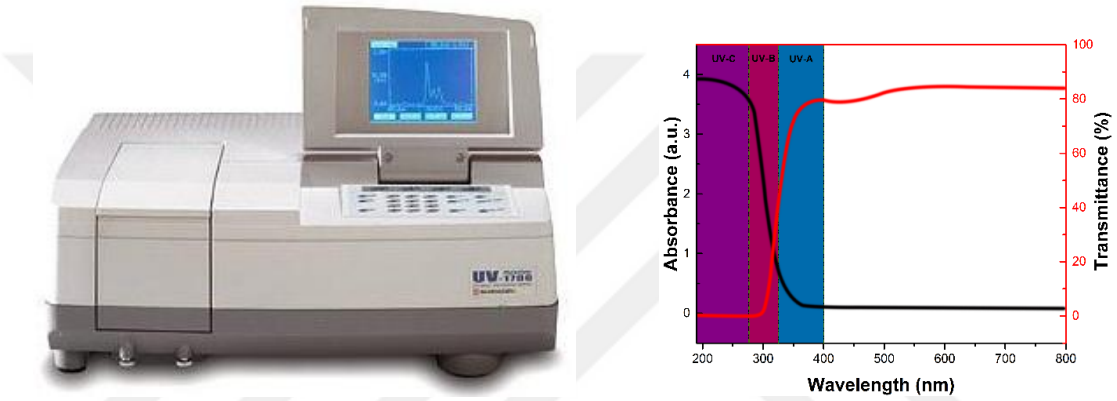


Figure 3.13 a) UV-Vis measurement system b) An example of absorbance and transmittance profile of n-SnO_2 (thin film) / glass

3.2.2 Determination of the UV photo-response and photovoltaic characteristics of the devices

In this section, the rectifying behavior and UV detection performance of Ag/n-SnO_2 (thin film)/p-Si/Ag , Ag/n-SnO_2 (Nanostructured)/n-SnO_2 (thin film)/p-Si/Ag heterostructure-based UV photodetectors were analyzed, and then, the important diode and UV photodetector parameters such as rectification ratio, photo-sensitivity, photo-responsivity, detectivity etc. were calculated. Additionally, photovoltaic performance of Ag/n-SnO_2 (Nanostructured)/n-SnO_2 (thin film)/p-Si/Ag heterostructure-based solar cells is investigated to determine the power conversion efficiency of the devices.

i) I-V measurements for evaluating the UV photo-response and photovoltaic characteristics

The current–voltage (*I–V*) characteristics of the photodetectors are measured with a Keithley 2400 source meter unit in the dark, under UV and simulated solar irradiation condition. In this measuremnt system, the back contact of the devices is connected to positive terminal of probe station, while the front contact of the devices is connected to negative terminal of probe station. Figure 3.14 shows the schematic of photoelectrical characterization system.

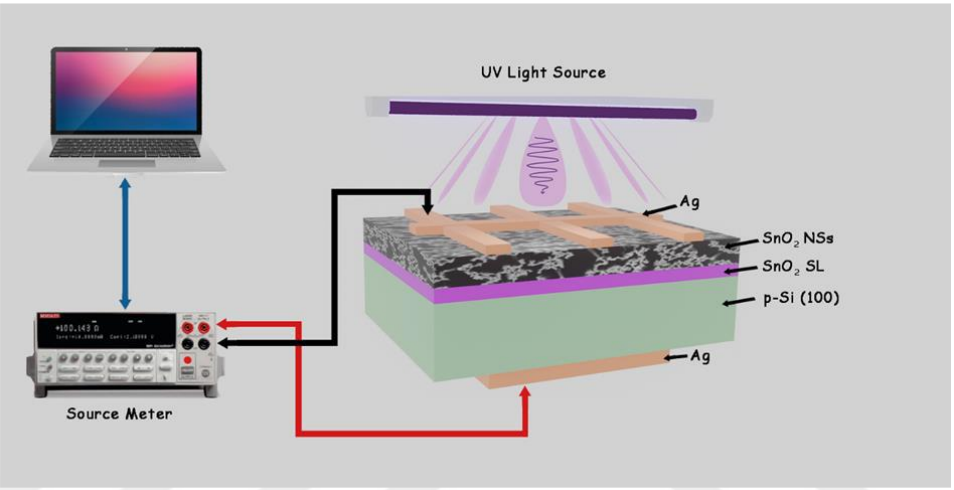


Figure 3.14 The schematic representation of *I-V* measurement system

The rectifying properties of the devices are characterized with some key parameters. From the dark *I-V* measurements, these parameters, the diode current *I*, ideality factor *n*, zero-bias barrier potential $Ø_{bi}$, and the rectification ratio ($I_{forward}/I_{reverse}$) are estimated using the general diode equations [100]. The UV photodetection properties of the devices are evaluated under UV illumination condition. The current changes of the devices working as UV photodetectors should be investigated in the third quadrant of the *I-V* curves.. The UV sensing performance of the devices is revealed by analyzing this quadrant and calculating the photodetector performance parameters. As for the analyses of photovoltaic performance, the devices are characterized under simulated solar radiation (ABET Tech. 10500, AM 1.5, 100mW/cm^2). The current-voltage changes of the devices exhibiting photovoltaic performance should be examined in the fourth quadrant of the *I-V* curves. From this quadrant, the photovoltaic performance parameters are obtained to calculate the conversion efficiency of the devices.

ii) I-t measurements for determining the transient photoresponse characteristics

The transient response (photocurrent-time (*I-t*)) characteristics of the photodetectors are measured under chopped UV light illumination condition. In this measurement system, the incident light beam is modulated with the help of a mechanical chopper affording adjustable duty cycle. The *I-t* measurements can be realized at different values of reverse applied voltage under various light power. In every cycle, a rapid increase/decrease in the amplitude of photocurrent values of the devices is monitored, as the light source is switched on/off. When the light falls on the device, the increase in the photocurrent values reaches a steady- state level in a short response time. This level depends on the illumination power, absorption and charge transport characteristics of the devices [101]. Figure 3.15 represents the schematic of the transient response characterization system.

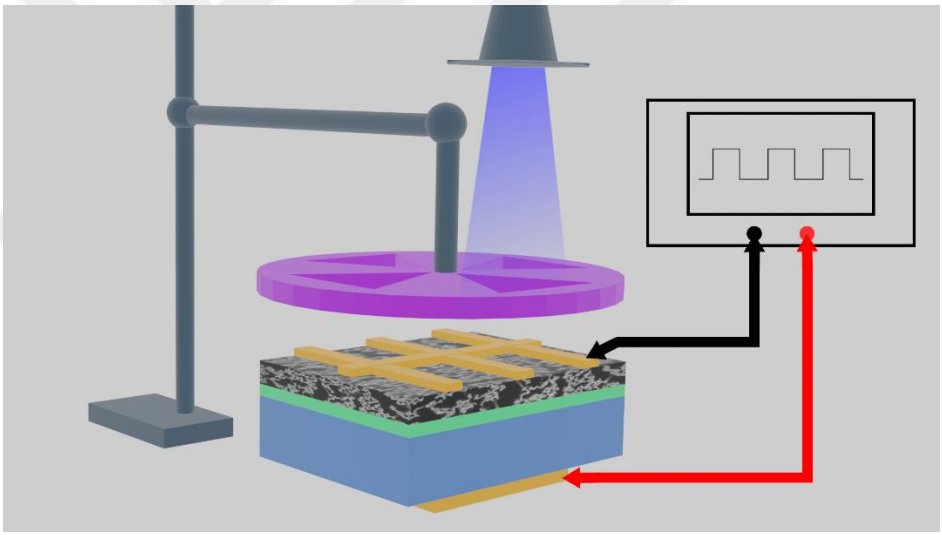


Figure 3.15 The schematic representation of *I-t* measurement system

The device transient behavior is characterized by values of rise time(t_r) and decay time (t_d). These parameters are determined by fitting the data of *I-t* characteristics. Multiple factors, including the photo-absorption speed, the magnitude of the built-in electric field, charge-carrier transport characteristics, density of trap states, the thickness of device components affect the response speed of a photodetector [102]. Also, the reproducibility and stability of the devices are investigated by this measurement.

CHAPTER 4

RESULTS AND DISCUSSION

As we mentioned in previous chapter, experimental studies include the optimization of the nanostructured SnO_2 layer growth by the hydrothermal method. The results indicate that the presence of the seed layer underneath the nanostructured layer is of utmost importance to obtain homogeneously distributed nanostructured SnO_2 layer. To investigate the effect of seed layer type on the growth of nanostructured SnO_2 layer and to determine the optimum performance of the devices, the devices designed without seeding layer or with seeding layer of SnO_2, ZnO, TiO_2 metal oxide semiconductors were fabricated. Under the sub-title of investigation of the effect of seed layer type on the performance of photodetectors, five (5) numbers of devices, having structure of SnO_2 seed layer (SL)/*p*-Si, SnO_2 nanostructured layer (NsL)/p-Si, SnO_2 nanostructured layer (NsL)/SnO_2 seed layer (SL)/p-Si, SnO_2 nanostructured layer/ZnO seeding layer (SL)/p-Si, SnO_2 nanostructured layer/TiO_2 seeding layer (SL)/p-Si, were fabricated and named as S1, S2, S3, S4, and S5, respectively. Among the fabricated devices, the best performance was found in S3. Subsequently, the solutions of seed layer and hydrothermal deposition was optimized to enhance the performance of the devices having structure of *n*-SnO_2 (Nanostructured)/*n*-SnO_2 (thin film)/*p*-Si. Under the sub-title of optimization of seed layer and hydrothermal deposition, five (5) numbers of samples, having heterostructure of *n*-$SnO_{2\text{-SL}}$/*p*-Si, *n*-$SnO_{2\text{-NSL}}$ (Sol.1)/*n*-$SnO_{2\text{-SL}}$/*p*-Si, *n*-$SnO_{2\text{-NSL}}$ (Sol.2)/*n*-$SnO_{2\text{-SL}}$/*p*-Si, *n*-$SnO_{2\text{-NSL}}$ (Sol.3)/*n*-$SnO_{2\text{-SL}}$/*p*-Si and *n*-$SnO_{2\text{-NSL}}$ (Sol.4)/*n*-$SnO_{2\text{-SL}}$/*p*-Si, were produced and designated as S6, S7, S8, S9 and S10, respectively. Among the produced samples, the highest performance was achieved by S7. Afterwards, the detailed analyses were performed to reveal the performance changes depending on the trap state density of the devices fabricated under identical experimental conditions with S7. Under sub-title of determination of performance limits of *n*-SnO_2/*p*-Si heterostructure-based UV photodetectors, five (5) number of devices were manufactured to scrutinize the maximum attainable performance limit of the device having same structure of S7. According to the performance status of the devices, fabricated samples are denoted

as S11, S12, S13, S14, and S15 from lowest to highest. Then, the photovoltaic performance of the produced samples was investigated under simulated solar irradiation. Under fair test conditions, it was observed that power conversion efficiency (PCE) value of final sample exceeds 2%, while the efficiency level of the others remained below 1%. Under sub-title of investigation of photovoltaic performance of the devices, three (3) numbers of samples with the n-SnO_2 thicknesses of 206, 304, and 391nm are fabricated to analyze the role of emitter layer thickness for the photovoltaic performance of the *n*-SnO_2/*p*-Si heterojunction based solar cells. The samples with SnO_2 thickness of 206, 304, and 391 nm are called S16, S17, and S18, respectively. The summary of the fabricated device structures is depicted in Table 4.1

Table 4.1 Summary of the fabricated device structures

Sub-title	Devices				
Investigation of the effect of seed layer type on the performance of photodetectors	S1	S2	S3	S4	S5
	Description				
	w/o *n*-SnO_2 nanostructured layer	w/o seed layer	w/ n-SnO_2 seed layer	w/ *n*-ZnO seed layer	w/ *n*-TiO_2 seed layer
	Device Structures				
	n-$SnO_{2\text{-}SL}$/*p*-Si	*n*-$SnO_{2\text{-}NsL}$ /*p*-Si	*n*-$SnO_{2\text{-}NsL}$ /*n*-$SnO_{2\text{-}SL}$ /*p*-Si	*n*-$SnO_{2\text{-}NsL}$ /*n*-$ZnO_{\text{-}SL}$ /*p*-Si	*n*-$SnO_{2\text{-}NsL}$ /*n*-$TiO_{2\text{-}SL}$ /*p*-Si
Sub-title	Devices				
Optimization of seed layer and hydrothermal deposition	S6	S7	S8	S9	S10
	Description				
	w/ optimized seed layer solution	w/ hydro-thermal solution 1	w/ hydro-thermal solution 2	w/ hydro-thermal solution 3	w/ hydro-thermal solution 4
	Device Structures				
	n-$SnO_{2\text{-}SL}$/*p*-Si	*n*-$SnO_{2\text{-}NsL}$ /*n*-$SnO_{2\text{-}SL}$ /*p*-Si	*n*-$SnO_{2\text{-}NsL}$ /*n*-$SnO_{2\text{-}SL}$ /*p*-Si	*n*-$SnO_{2\text{-}NsL}$ /*n*-$SnO_{2\text{-}SL}$ /*p*-Si	*n*-$SnO_{2\text{-}NsL}$ /*n*-$SnO_{2\text{-}SL}$ /*p*-Si
Sub-title	Devices				
Determination of performance	S11	S12	S13	S14	S15
	Description				

limits of n-SnO_2/p-Si heterostructure-based UV photodetectors	yields *PR* of 21.91 A/W	yields *PR* of 28.90 A/W	yields *PR* of 35.48 A/W	yields *PR* of 38.73 A/W	yields *PR* of 43.91 A/W
	Device Structures				
	n-$SnO_{2\text{-NsL}}$ /*n*-$SnO_{2\text{-SL}}$ /*p*-Si	*n*-$SnO_{2\text{-NsL}}$ /*n*-$SnO_{2\text{-SL}}$ /*p*-Si	*n*-$SnO_{2\text{-NsL}}$ /*n*-$SnO_{2\text{-SL}}$ /*p*-Si	*n*-$SnO_{2\text{-NsL}}$ /*n*-$SnO_{2\text{-SL}}$ /*p*-Si	*n*-$SnO_{2\text{-NsL}}$ /*n*-$SnO_{2\text{-SL}}$ /*p*-Si
Sub-title	Devices				
Investigation of photovoltaic performance of the devices	S16	S17	S18		
	Description				
	w/ *n*-SnO_2 thickness of 206 nm	w/ *n*-SnO_2 thickness of 304 nm	w/ *n*-SnO_2 thickness of 391 nm		
	Device Structures				
	n-$SnO_{2\text{-NsL}}$ /*n*-$SnO_{2\text{-SL}}$ /*p*-Si	*n*-$SnO_{2\text{-NsL}}$ /*n*-$SnO_{2\text{-SL}}$ /*p*-Si	*n*-$SnO_{2\text{-NsL}}$ /*n*-$SnO_{2\text{-SL}}$ /*p*-Si		

In summary, a route towards the determination of final device structure was revealed by evaluating the results of characterizations in this section. This chapter starts with the determination of the seed layer type, continues with the optimization of the device structure, and concludes with the determination of the achievable performance limit of the fabricated devices and the examinations for the devices exhibiting photovoltaic features.

4.1 Investigation of the effect of seed layer type on the performance of the devices

Based on the publications “A route towards enhanced UV photo-response characteristics of SnO_2/*p*-Si based heterostructures by hydrothermally grown nanorods”, K. Ozel, A. Atilgan, N. E. Koksal, A. Yildiz, Journal of Alloys and Compounds, 2020, 849, 156628 [14], and “SnO_2/ZnO/*p*-Si and SnO_2/TiO_2/*p*-Si heterojunction UV photodiodes prepared using a hydrothermal method”, K. Ozel, A. Yildiz, Sensors and Actuators A: Physical, 2020, 315, 112351 [76], this section is reproduced (or “reproduced in part") with permission from Journal of Alloys and Compounds, and Sensors and Actuators A: Physical. Copyright 2020 Elsevier Publisher.

To examine the effect of seed layer type on the performance of photodetectors, five (5) number of devices having structure of SnO_2 seeding layer (SL)/*p*-Si, SnO_2 nanostructured layer (NsL)/*p*-Si, SnO_2 nanostructured layer (NsL)/SnO_2 seeding layer (SL)/*p*-Si, SnO_2 nanostructured layer/ZnO seeding layer (SL)/*p*-Si, SnO_2 nanostructured layer/TiO_2 seeding layer (SL)/*p*-Si were fabricated and named as S1, S2, S3, S4, and S5, respectively.

The coating solutions were obtained by mixing Tin (II) chloride dehydrate ($SnCl_2.2H_2O$), monoethanolamine (C_2H_7NO) and 2-methoxyethanol ($C_3H_8O_2$) for the deposition of n-SnO_2 seed layer [30], Zinc acetate dehydrate ($Zn(CH_3COO)_2{\cdot}2H_2O$), Monoethanolamine ($C_2H_7NO$) and Ethanol($C_2H_5OH$) for the deposition of n-ZnO seeding layer, and Titanium (IV) chloride, titanium tetrachloride ($TiCl_4$) and Isopropyl alcohol (C_3H_8O) for the deposition of *n*-TiO_2 seed layer [76]. The prepared coating solutions were spin-coated (2000 rpm spin speed for 30 sec) on cleaned Si wafers to fabricate S1, S3, S4, and S5. For the fabrication of *n*-SnO_2, *n*-ZnO, and *n*-TiO_2 nanostructured layer of S2, S3, S4, and S5, *p*-Si wafers covering with/without seeding layer were loaded into a hydrothermal autoclave. Thereafter, hydrothermal deposition technique was realized at 95°C for 18 h. After taking out the samples from the hydrothermal autoclave, they were immersed in DI water to remove unwantedly grown residuals. Upon drying process in an ambient air, back contacts were obtained by applying Ag paste to the entire back surface of the samples. Next, front contacts were designed by applying Ag paste on front surface of the samples as grid-shaped of 0.08 cm width and 0.1 cm breadth, respectively. The fabrication characteristics of the photodetectors are summarized in Table 4.2.

Table 4.2 Fabrication characteristics of designed photodetectors

Devices	S1	S2	S3	S4	S5
Structure	$SnO_{2\text{-}SL}$/*p*-Si	$SnO_{2\text{-}NsL}$/*p*-Si	$SnO_{2\text{-}NsL}$/ $SnO_{2\text{-}SL}$/*p*-Si	$SnO_{2\text{-}NsL}$/ ZnO_{SL}/*p*-Si	$SnO_{2\text{-}NsL}$/ $TiO_{2\text{-}SL}$/*p*-Si
Method	Spin-coating	Hydrothermal	Hydrothermal / Spin-coating	Hydrothermal / Spin-coating	Hydrothermal / Spin-coating
Experimental Conditions	30 s, 2000 rpm	18h, 95°C	18h, 95°C/30s, 2000 rpm	18h, 95°C/30s, 2000 rpm	18h, 95°C/30s, 2000 rpm
Type of seeding layer	SnO_2	-	SnO_2	ZnO	TiO_2
Thickness of seeding layer (nm)	~80nm	-	~80nm	~80nm	~80nm

The measured optical spectra of the deposited layers on glass substrates are displayed in Figure 4.1. The transmittance spectra of the samples reveal that the deposited layers exhibit high transparency of over 70% in the visible region. Further, the band gap (E_g) values of the samples can be determined by applying Tauc model [103]. This model can be applied for direct band semiconductors like SnO_2 by giving the relation between absorption and photon energy in power law form [98].

Inset of figure 4.1 illustrates the Tauc plots of samples. The band gap values of the samples are estimated as 3.83 eV for S1, 3.60 eV for S2, 3.90 eV for S3, 3.25 eV for S4, and 3.65 eV for S5 by fitting the linear part of the of $(\alpha h\upsilon)^2$ vs. $h\upsilon$ plot. The estimated band gap values match well with the literature [104-106]. From the results, one can state that band gap values differ in size depending on the structure of the samples. These differences can be stemmed from various theoretical models including Burstein-Moss (BM) effect [107], quantum confinement effect [108], and surface states [109], etc. According to many reported studies, the Burstein-Moss (BM) effect is responsible for the band gap widening in *n*-type semiconductors. As for the samples containing ZnO and TiO_2 seed layers, the band gap shrinkage of the samples is due to the small band gap values of these seed layers compared to SnO_2.

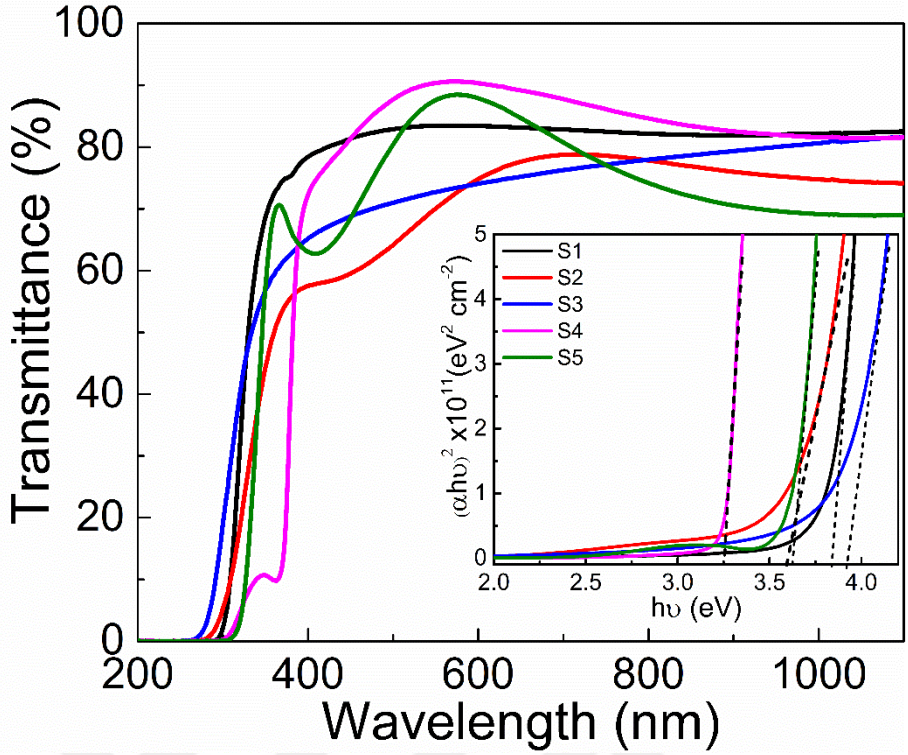


Figure 4.1 The optical transmittance profile of emitter layers of the samples. The inset figure shows the Tauc plots to determine the band gap value of samples.

The scanning electron microscopy (SEM) images of devices are given in Figure 4.2. Figure 4.2 (a) and (b) show the cross-sectional SEM images of the samples of SnO_2 nanostructured layer (NsL)/*p*-Si and SnO_2 nanostructured layer (NsL)/SnO_2 seeding layer (SL)/*p*-Si, respectively. From figure 4.2 (a) and (b), one can express that the presence of seed layer plays a key role in the growth mechanism of nanostructures [110]. Figure 4.2 (c) and (d) show the cross-sectional SEM images of the samples of SnO_2 nanostructured layer (NsL)/ZnO seed layer (SL)/*p*-Si, and SnO_2 nanostructured layer (NsL)/TiO_2 seed layer (SL)/*p*-Si, respectively. As seen from figure 4.2, one can easily state that the type of seed layer affects the nature of nanostructures. Ultimately, the obtained nanostructures can promote the detection performance of the devices by enhancing the light-matter interaction.

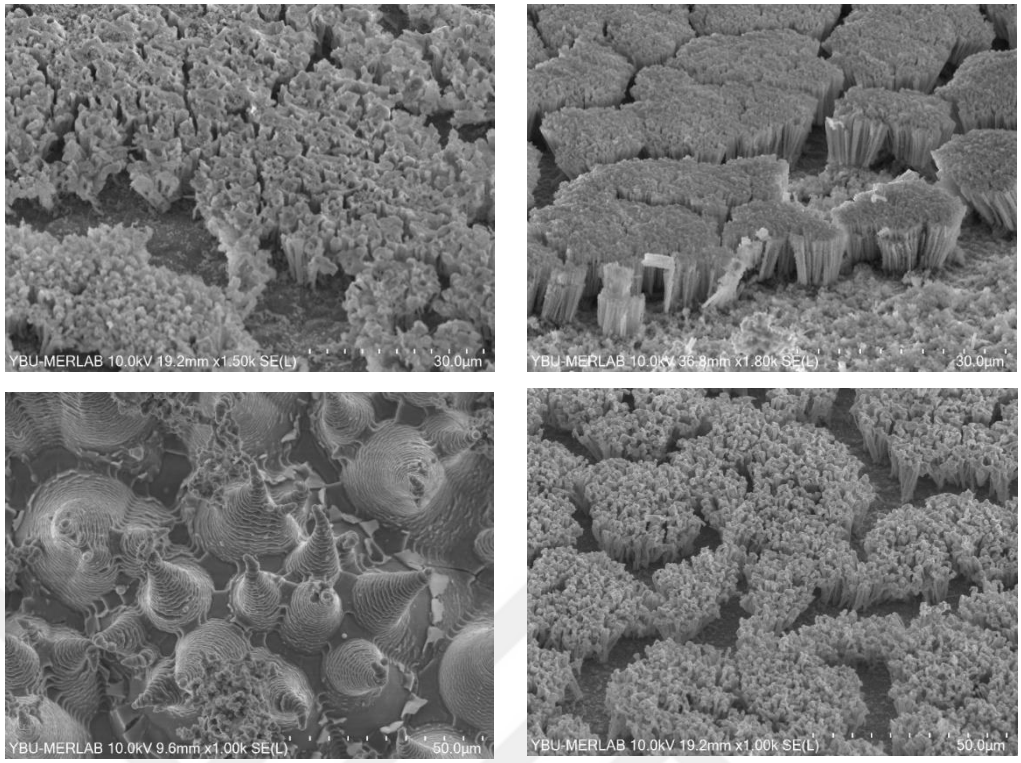


Figure 4.2 Cross-sectional SEM images of (a) SnO_2 nanostructured layer (NsL)/*p*-Si, (b) SnO_2 nanostructured layer (NsL)/SnO_2 seed layer (SL)/*p*-Si, (c) SnO_2 nanostructured layer (NsL)/ZnO seed layer (SL)/*p*-Si, and (d) SnO_2 nanostructured layer (NsL)/TiO_2 seed layer (SL)/*p*-Si

Figure 4.3 shows the semi-logarithmic plotted current-voltage (*I*-*V*) curves of the devices under dark and UV irradiation conditions. From *I*-*V* graphs, one can comprehend that fabricated photodetectors operate under reverse bias conditions. In case of the wavelength of the incident light is below the cut-off wavelength of emitter layer, photons are directly absorbed by the emitter layer. Once the wavelength of the incident light is greater than the cut-off wavelength of emitter layer, photons reach the depletion region formed at the heterointerface and absorber layer. The absorbed photons generate the electron-hole pairs, which diffuse to depletion region, therein they separated by built-in electric field and drift in opposite directions. Upon collecting of separated carriers at the output terminals, the photocurrent starts to flow throughout an external circuit.

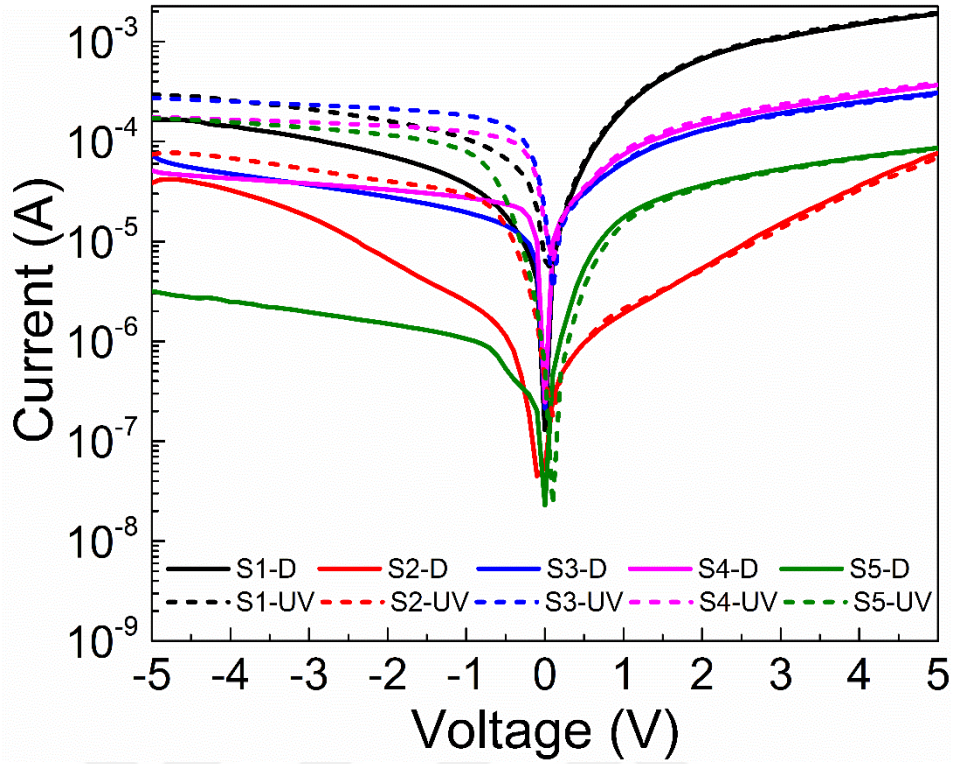


Figure 4.3 The semi-logarithmic plotted current-voltage (*I-V*) curves of the devices under dark and UV irradiation conditions.

In view of the results of *I-V* measurements, it is evident that the fabricated devices are responsive to UV light thanks to the intrinsic band gap value of SnO_2. From the *I-V* curves, the rectifying behavior obtained in the dark condition confirms the formation of p-n heterojunction at the interface of *n*-SnO_2 and *p*-Si. As mentioned before, the seed layer affects the formation of nanostructured layers, and also regulates the transport characteristics by influencing the recombination rate and transport length of carriers [111]. Hence, it is expected that the devices constructed by different seed layer have different diode and photodetection performance. Table 4.3 summarizes the important diode and photodetector parameters of the fabricated photodetectors.

Table 4.3 Comparison of the diode and photodetection parameters of the fabricated devices.

Devices	I_s (μA)	n	$Ø_{bi}$ (eV)	*PR* (mA/W)	*PS*
S1	1.700	3.5	0.70	62	1.8
S2	0.077	4.5	0.78	19	2.1
S3	0.810	2.8	0.72	110	5.3
S4	6.080	7.8	0.67	68	3.9
S5	0.210	4.8	0.76	92	63

As seen in Table 4.3, the fabricated devices have low value of leakage current and relatively high value of barrier potential, indicating the presence of high-quality junction interface. As for the obtained values of *n*, the deviation from unity is inherent for heterostructure-based devices. These non-unity values of n might be caused from the following factors; i) series resistance, ii) interface states, iii) native oxide layer, iv) defects, and v) barrier inhomogenity, etc. [112].

Let us now focus on the UV sensing performance of the fabricated photodetectors, two key figures of merits, namely, photo-responsivity (PR) and photo-sensitivity (PS) should be calculated for the evaluation of UV detection properties of the devices. The UV detection performance of the present devices are assessed under the exposure of 254 nm UV light.

It is noteworthy to say that the UV detection performance of the devices are superior to the previously reported thin film-based devices [113-115]. Among the fabricated devices, the superior performance of the S3 is drawn more attention. Such a high performance of S3 is a result of its high photocurrent value. The optical properties, especially light-material interaction and charge transport characteristics play a decisive role in the photocurrent values of the samples. Considering the performance of S3, homogeneous growth of nanostructures, ameliorated interface resistance by seeding layer and appropriate band bending provide the generation and efficacious transfer of charge carriers, which in turn, emphasize that the device makes more use of light and achieves efficient light-electricity conversion.

4.2 Optimization of seed layer and hydrothermal deposition

Based on the publication “A Self-Powered Ultraviolet Photodetector with Ultrahigh Photoresponsivity (208 mA W^{-1}) based on SnO_2 Nanostructures/Si Heterojunctions”, K. Ozel, A. Yildiz, Physica Status Solidi (RRL) – Rapid Research Letters, 2100085 [116], this section is reproduced (or “reproduced in part") with permission from Physica Status Solidi (RRL) – Rapid Research Letters. Copyright 2021 Wiley-VCH GmbH.

In the light of the results obtained in the previous section, the search for improvement in device performance was continued and the hydrothermal growth process of the fabricated UV photodetector having architecture of $SnO_{2\text{-}NsL}/SnO_{2\text{-}}$

$_{SL}$/*p*-Si was analyzed and the effect of hydrothermal solution on the UV detection performance of the devices was also investigated. In addition, the seed layer of the devices was reworked and a new thin-film solution with higher performance was produced and a device produced with this solution was reported [117]. The fabrication and characterization of five (5) numbers of samples produced using four (4) different hydrothermal solutions and a new seed layer solution will be reported in this section.

The new seed layer solution was prepared by means of dissolving 3.348 g of $SnCl_2 \cdot 2H_2O$ in 40 ml of ethanol (C_2H_6O). The solution obtained was mixed in a closed beaker at 80°C for 2 hours, then the beaker was opened and the solution was left to evaporate. As a result, the dry precipitates remaining in the beaker was mixed again in 20 ml of ethanol at 50°C for 2 hours and the final seeding solution was prepared [96]. The prepared seeding solution was spin-coated onto the surface of *p*-Si and glass substates, which were cleaned by applying cleaning procedures mentioned in chapter 3. Four (4) different hydrothermal coating solutions were prepared to investigate the effect of different hydrothermal solutions on the performance of the devices. The hydrothermal solution 1 was obtained by mixing 0.009 g $SnCl_4 \cdot 5H_2O$, 0.23 g urea, 25 ml de-ionized water (DIW), 1.25 ml hydrochloric acid (HCl). The hydrothermal solution 2 was prepared by mixing 225.63 mg of $SnCl_2 \cdot 2H_2O$, 12.5 ml of ethanol (EtOH), 10 ml of de-ionized water (DIW) and 0.02 ml of sodium hydroxide (NaOH). The hydrothermal solution 3 was obtained by mixing 0.263 g of $SnCl_4.5H_2O$, 0.01 ml of sodium hydroxide (NaOH), 5 ml of ethylen glycol, 10 ml of ethanol (EtOH). The hydrothermal Solution 4 was prepared by mixing 0.2 g of $SnCl4 \cdot 5H_2O$, 0.084 g of hexamethylenetetramine (HMT), 10 ml of de-ionized water (DIW), 10 ml of ethanol (EtOH) and 0.018 ml of sodium hydroxide (NaOH). Upon preparing solutions, 4 sets of substates consisting of 1 *p*-Si and 1 glass slides, which were previously coated with seed layer, were placed in four different hydrothermal autoclave and the prepared four different hydrothermal solutions were poured into these four different autoclaves. Hydrothermal growth process was carried out for 18 hours at 95°C. Subsequently, the front and back metallization process were accomplished by utilizing screen printing method. The photodetectors fabricated in

this section, having heterostructure of *n*-$SnO_{2\text{-}SL}$/*p*-Si, *n*-$SnO_{2\text{-}NsL}$ (Sol.1)/*n*-$SnO_{2\text{-}SL}$/*p*-Si, *n*-$SnO_{2\text{-}NsL}$ (Sol.2)/*n*-$SnO_{2\text{-}SL}$/*p*-Si, *n*-$SnO_{2\text{-}NsL}$ (Sol.3)/*n*-$SnO_{2\text{-}SL}$/*p*-Si and *n*-$SnO_{2\text{-}NsL}$ (Sol.4)/*n*-$SnO_{2\text{-}SL}$/*p*-Si are denoted as S6, S7, S8, S9 and S10, respectively.

The top-surface SEM images of the deposited *n*-SnO_2 layers are given in Figure 4.4 a-e. SEM images confirm the denser nature of seeding layer and the porous nature of nanostructured layer. The porous structure observed here increases the light-material interaction, which in turn, improves the utilization of light by the produced devices, and thus promoting the number of electron-hole (e–h) pairs to be produced [118]. In addition, the cross-sectional SEM image of the device (S7) manifests that the thickness of seed layer is estimated to be 60 nm, and the thickness of the nanostructured layers is around 200 nm.

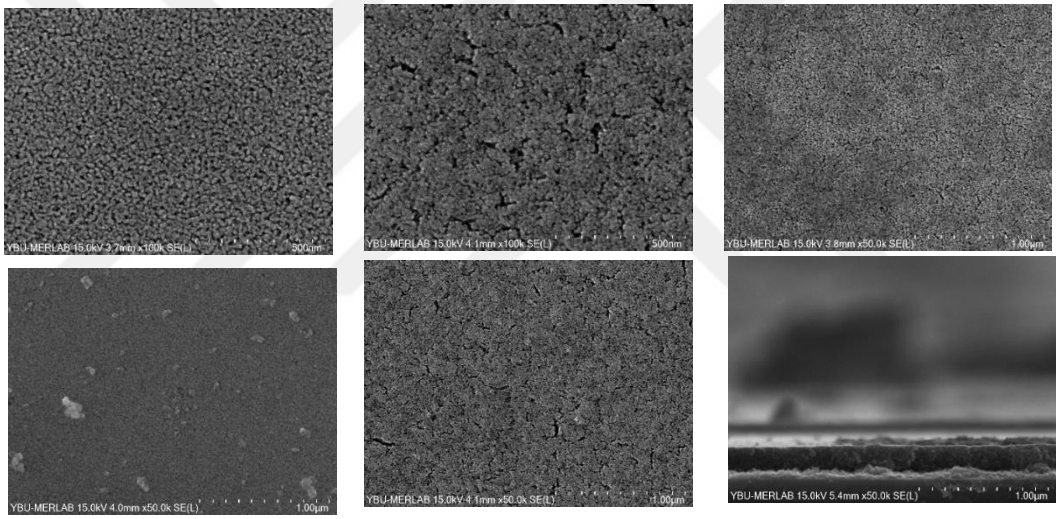


Figure 4.4 Top-surface SEM images of (a) S6, (b) S7, (c) S8, (d) S9, (e) S10, and (f) the cross-sectional SEM image of the device (S7).

The optical spectra of the samples produced by depositing aforementioned solutions on glass slides are utilized to analyze the optical properties and bandgap values of the obtained structures. From Figure 4.5, one can easily say that all fabricated structures exhibit high transmittance over 80%. The inset of Figure 4.5 shows the Tauc plots of the samples. As observed, the bandgap values of the samples are evaluated to be 3.88, 3,93, 3.83, 3.87 and 3.89 eV for S6, S7, S8, S9, and S10, respectively. Evidently, the results indicate that the fabricated structures show remarkable absorption in the UV spectrum with a sharp absorption edge at ≈320 nm, verifying the UV detection capacity of the devices.

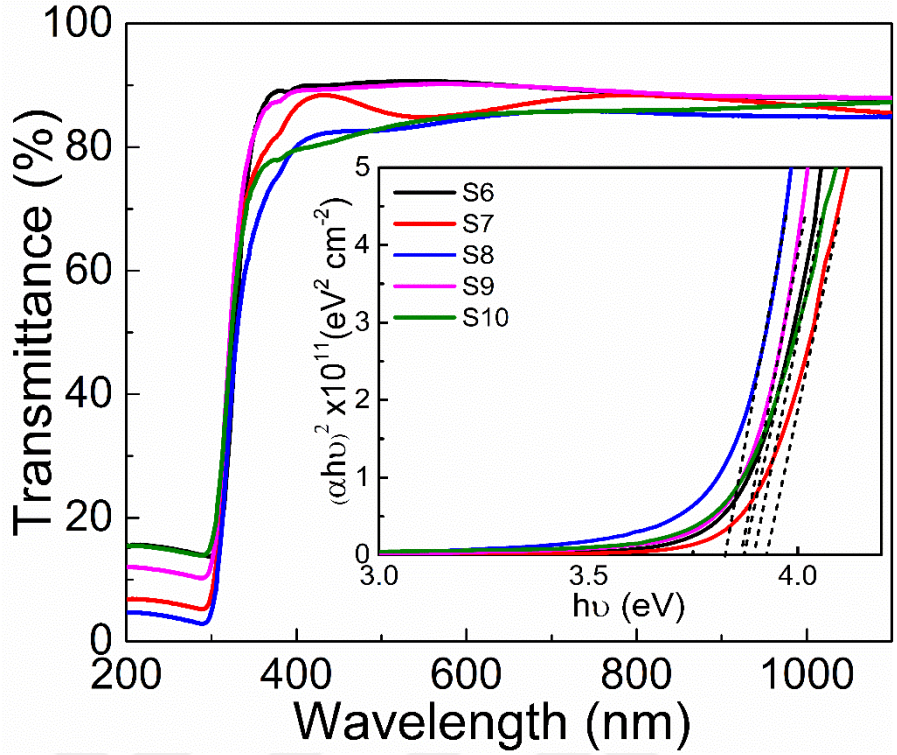


Figure 4.5 Transmittance spectra for the samples. The inset depicts the Tauc plots to extract the band gap size of samples.

Figure 4.6 illustrates the log-scale current–voltage (*I–V*) curves of the devices measured in the dark and under the exposure of 311 nm UV light (0.1 mW/cm^2). The obtained curves clearly show an excellent rectifying behavior of the devices with a low value of dark current. The values of dark current are found to be 1.38 um for S6, 6.48 um for S7, 27.3 um for S8, 55.9 um for S9, and 4.07 um for S10. In addition, the increase in the current value produced under UV light in the reverse bias region indicates the UV detection capabilities of the devices. To characterize the UV sensing performance of the samples, critical performance parameters, particularly photo-responsivity, photo-sensitivity, detectivity, external quantum efficiency, linear dynamic range, and near equivalent power are determined and summarized in Table 4.4.

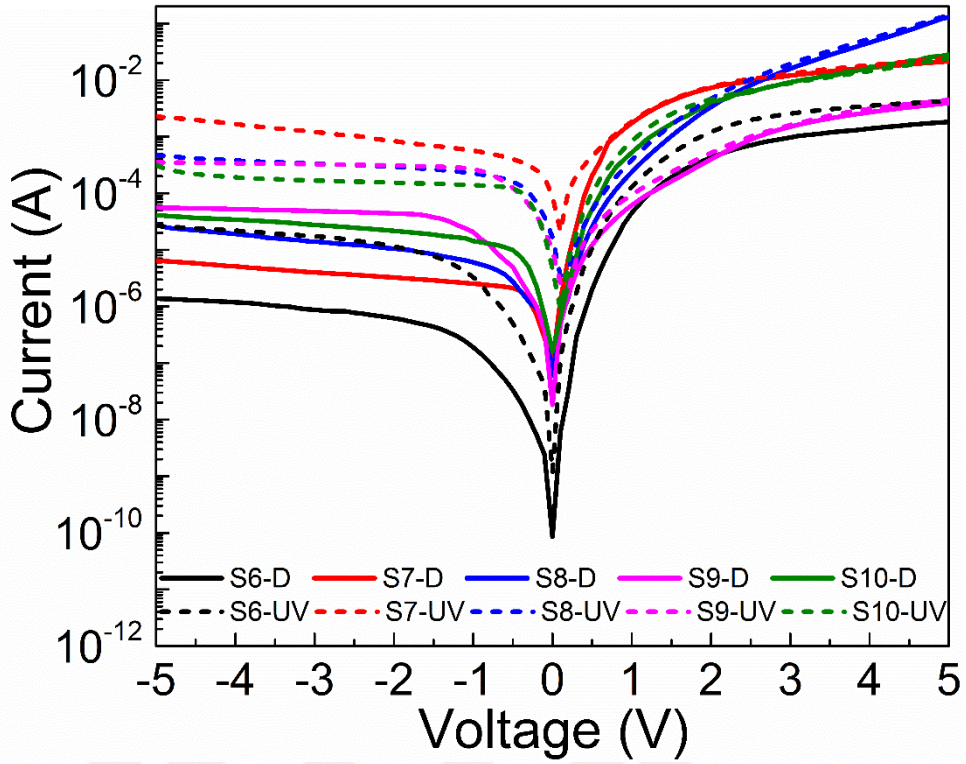


Figure 4.6 The log-scale current–voltage (*I–V*) characteristics for the samples.

Table 4.4 The performance parameters of the samples

Devices	*PR* (A/W)	*D** (Jones)	*EQE* (%)	*PS*	*LDR* (dB)	*NEP* (W)
S6	0.25	3.81×10^{11}	100.72	19.34	25.73	2.63×10^{-12}
S7	22.73	1.58×10^{13}	9064.83	351.75	50.92	6.34×10^{-14}
S8	4.45	1.50×10^{12}	1772.27	17.26	24.74	6.65×10^{-13}
S9	2.53	5.99×10^{11}	1009.94	5.54	14.88	1.67×10^{-12}
S10	2.73	7.55×10^{11}	1086.83	7.69	17.73	1.32×10^{-12}

As observed from Table 4.4, it is obvious that S7 exhibits superior performance over its counterparts. Hence, S7 deserves more discussion for further performance improvement. Hereafter, we concentrate on the performance of S7, and compare its performance with bare device (S6). The time-dependent photoresponse plots of the devices are measured under modulated UV irradiation of 311 nm. All fabricated samples display strong reproducibility in response to on/off illumination. Figure 4.7 demonstrates the time-dependent photoresponse plots of the devices (S6) and (S7). The values of rise times (t_r) and decay times (t_d) are determined to be 19 and 10 ms for S6, 37 and 27 ms for S7, respectively. As can be seen, it is clear that the increase in thickness of *n*-SnO_2 layer reduces the photoresponse speed of the devices [118].

However, high values of photo-responsivity overshadow the loss in photoresponse speed of the devices.

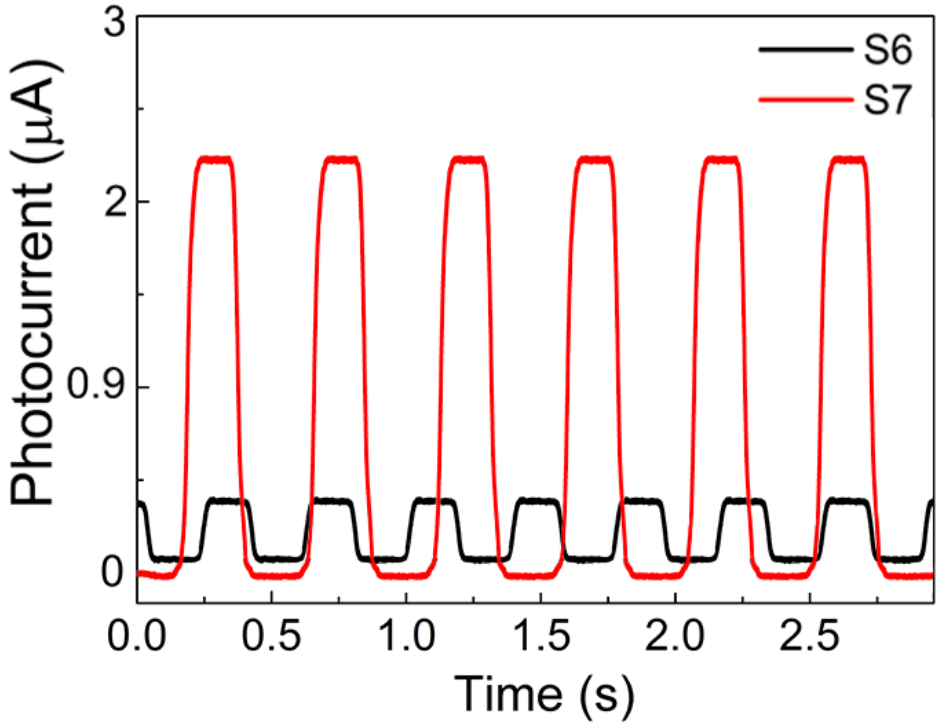


Figure 4.7 The time-dependent photoresponse plots of the devices (S6) and (S7).

Capacitance (C)- voltage (V) characteristics of the device are measured to estimate the values of built-in potential (V_{bi}) and donor concentration (N_d). The variation in depletion region capacitance can be expressed by the following equation [119].

$$C^2 = \frac{qA^2 N_a N_d \varepsilon_n \varepsilon_p}{2(N_d \varepsilon_n + N_a \varepsilon_p)} \frac{1}{V_{bi} - V} \qquad (4.1)$$

Where N_a, $\mathcal{E}_n$ and $\mathcal{E}_p$ refer to acceptor concentration, dielectric permittivity of n-SnO_2 and p-Si, respectively. Figure 4.8 shows the $1/C^2$-V characteristics of S6 and S7. The formation of heterojunction at the interface of n-SnO_2 and p-Si is verified by the linear behavior of $1/C^2$-V characteristics. From $1/C^2$-V curves, the values of N_d and V_{bi} are determined as 8.92×10^{15} cm^{-3} and 0.6 V for S6, 1.46×10^{16} cm^{-3} and 0.63 V for S7, respectively.

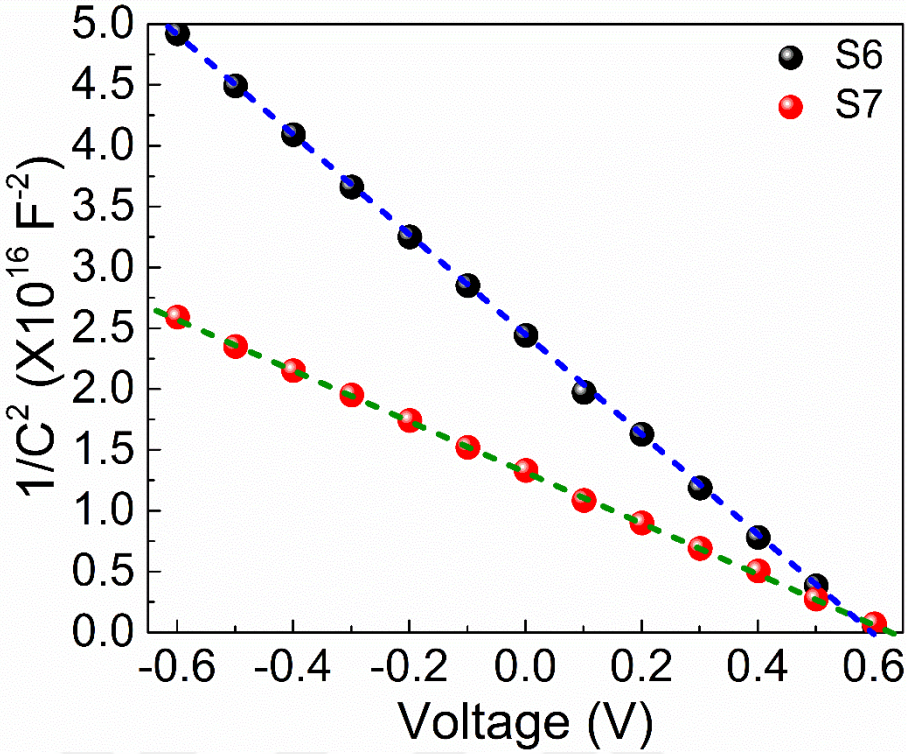


Figure 4.8 The $1/C^2$-V characteristics of S6 and S7.

Moreover, the values of potential difference of E_c-E_f for the *n*-side and E_f-E_v for the *p*-side can be evaluated by using the equations (4.2) and (4.3), respectively.

$$\frac{E_c - E_f}{q} = \frac{k_B T}{q} \ln\left(\frac{N_c}{N_d}\right) \quad (4.2)$$

$$\frac{E_f - E_v}{q} = \frac{k_B T}{q} \ln\left(\frac{N_v}{N_a}\right) \quad (4.3)$$

where N_c and N_v stand for the effective density of the conduction band and the effective density of the valence band. The values of N_c and N_v can be determined utilizing the values of effective masses of electron ($m_e^* = 0.28\, m_0; m_0$: free electron mass) and hole ($m_h^* = 0.56\, m_0$). The calculated values of N_c and N_v are found to be 3.716x10^{18} cm^{-3} and 1.04x10^{19} cm^{-3}, respectively [87, 120].

Further, the values of built-in potentials on the *n*-SnO_2 (V_{Dn}) and *p*-Si (V_{Dp}) can be determined by equations (4.4) and (4.5), respectively.

$$V_{Dn} = \frac{qN_d X_n^2}{2\varepsilon_n} \quad (4.4)$$

$$V_{Dp} = \frac{qN_a X_p^2}{2\varepsilon_p} \quad (4.5)$$

where x_n and x_p denote the components of the depletion layer width on the *n*-SnO_2 and *p*-Si. The band bending can be determined based on the calculated components. The values of the obtained parameters are specified in the energy band alignment, as shown in Figure 4.9. The results endorse that the high-performance device (S7) achieves effective charge separation due to its higher depth of band **bending [121].**

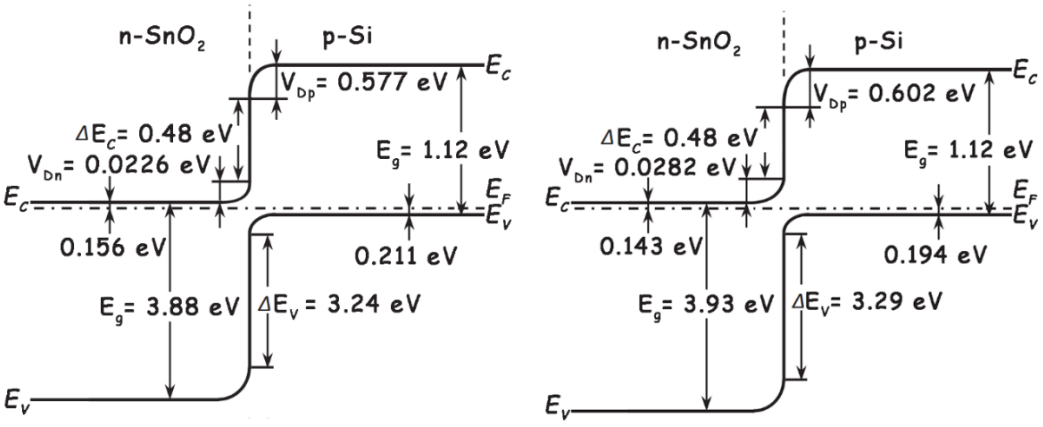


Figure 4.9 a, b) The energy band alignment of S6 (a) and S7 (b) in thermal equilibrium.

In summary, the results disclose that the high performance of the device can be attributed to the nature of nanostructures, the absorption of incident photons, the junction characteristics of *p-n* heterojunctions, and the separation efficiency of charge carriers.

4.3 Determination of performance limits of n-SnO_2/p-Si heterostructure-based UV photodetectors

Based on the publication "Estimation of Maximum Photoresponsivity of *n*-SnO_2/*p*-Si Heterostructure-based UV Photodetectors", K. Ozel, A. Yildiz, Physica Status Solidi (RRL) – Rapid Research Letters, 2100490 [88], this section is reproduced (or "reproduced in part") with permission from Physica Status Solidi (RRL) – Rapid Research Letters. Copyright 2021 Wiley-VCH GmbH.

In this section, SnO_2/*p*-Si heterostructure-based UV photodetectors fabricated under identical condition of S7 exhibiting high-performance in previous section are produced and characterized to determine the stability and performance limits of the devices. The photo-responsivity values of the devices are determined under various light power condition ranging from 0.1 to 1.2 mA /cm^2. The photocurrent values of

the samples are expected to improve with increasing light power. Nevertheless, the trend of increase of photocurrent values differs from one sample to another depending on the structural characteristics of the samples [122-123]. The relationship between increase in photocurrent values and power exponent provides sufficient information to estimate the maximum photo-responsivity values. To extract this relationship, five (5) numbers of devices are manufactured under identical condition and named as S11, S12, S13, S14, S15 from lowest performance status to highest. The fabrication process was carried out by following the manufacturing steps of the device with the highest performance produced in the previous section [116].

The XRD analysis result of the sample (S15) is presented in Figure 4.10 (a). The resulting plot has four peak, indicating polycrystalline nature of *n*-SnO_2 layer (JCPDS Card no:077-0451). The higher intensity of (110) peak demonstrates the dominant orientation of *n*-SnO_2 layer. In addition, the energy dispersive spectroscopy (EDS) spectra of the sample (S15) is given in Figure 4.10 (b). EDS measurement confirms that the *n*-SnO_2 layer deposited on *p*-Si consists of Sn and O elements.

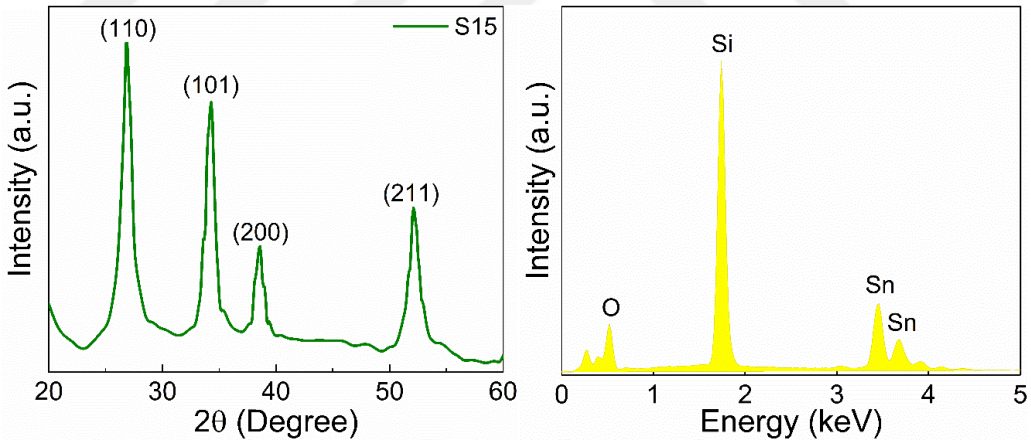


Figure 4.10 (a) XRD pattern and (**b**) EDS spectra of the sample (S15).

Figure 4.11 (a-e) presents the top-surface SEM micrographs of the produced samples. These micrographs display that each sample has different morphology than others in respect of porous nature. Different surface morphologies play a decisive role on the performance of the devices by affecting the ohmic behavior at the junction of Ag contact and *n*-SnO_2. The characteristics of the ohmic behavior can be determined by measuring the *I-V* curves at the junction of Ag contact and *n*-SnO_2. As delineated in Figure 4.11 (f), the cross-sectional SEM image of the sample (S15)

reveals that the thickness of deposited *n*-SnO_2 is around 230 nm. The measured *I-V* curves are depicted in the inset of Figure 4.12. From the *I-V* curves, one can expect that the device (S15) outperforms than others.

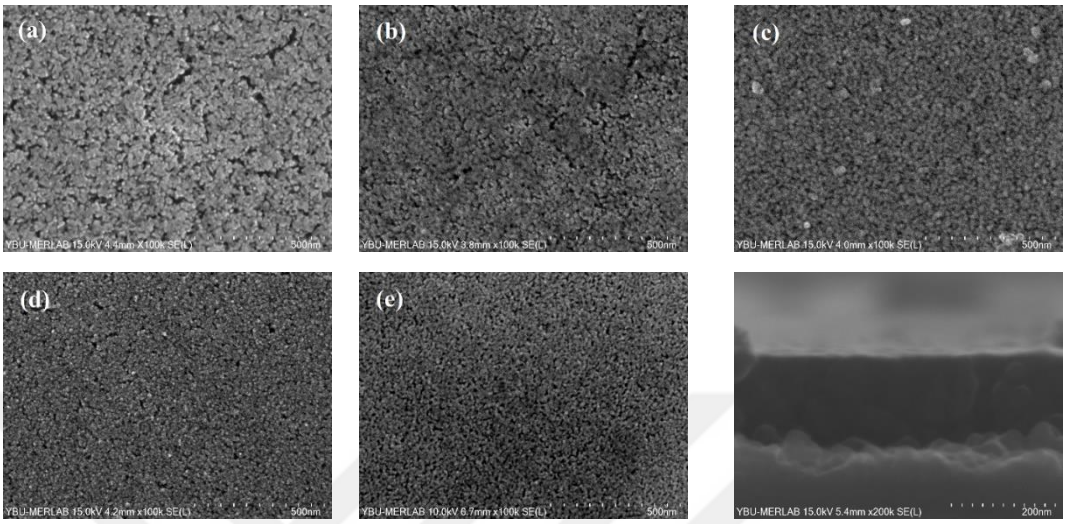


Figure 4.11 SEM micrographs of a) S11, b) S12, c) S13, d) S14, e) S15, and cross-sectional SEM images of the SnO_2 layer (S15).

The semi-logarithmic current-voltage (*I-V*) curves of the photodetectors measured under dark and UV irradiation (311 nm) conditions are displayed in Figure 4.12. As seen, all the devices perform good rectifying behavior with a high rectification ratio in the dark condition. Under excitation of UV light, the devices exhibit an outstanding photoresponse at reverse bias region. The photo-responsivity (*PR*) values of the devices are determined at 0.1 mW/cm^2 as 21.8 A/W for S11, 23.8 A/W for S12, 32.8 A/W for S13, 38,3 A/W for S14 and 43.8 A/W S15. Trap densities of the devices are responsible for the fluctuations in *PR* values of the devices.

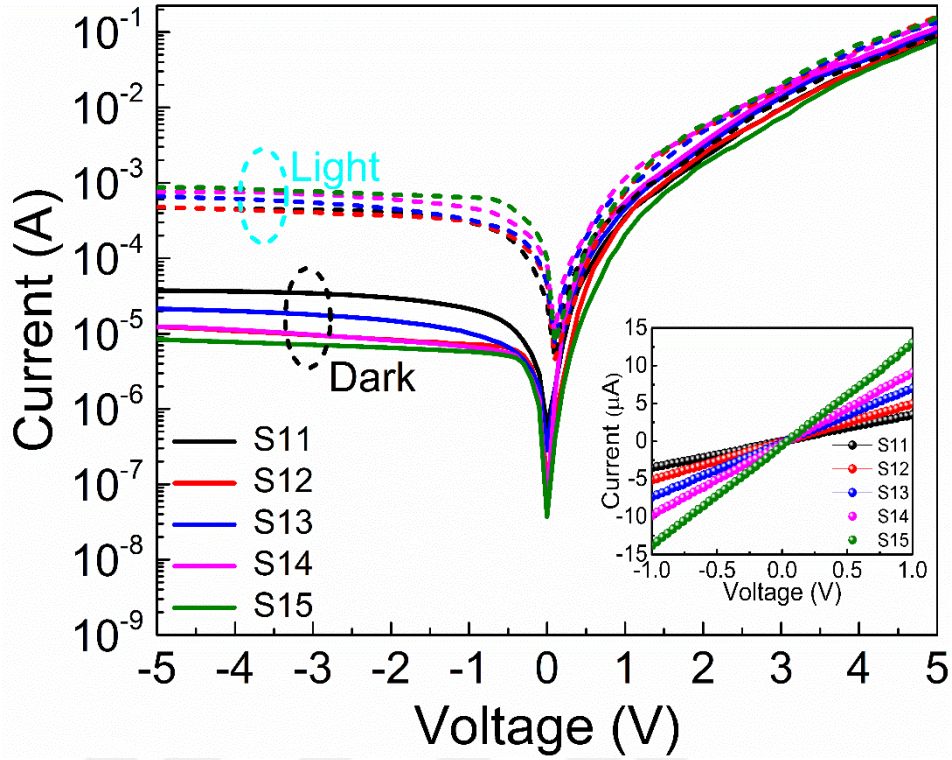


Figure 4.12 The semi-logarithmic current-voltage (*I-V*) curves of the photodetectors measured under dark and UV irradiation (311 nm) condition. Inset shows the ohmic characteristics between Ag contact and *n*-SnO_2.

The change in photocurrent values extracted from the photodetectors depending on the illumination power can give information about the trap states of the devices. To unveil the dependency of photogenerated current values of the samples on the illumination intensity, the *I-V* characteristics of the devices were obtained under various illumination intensities changing from 0.1 to 1.2 mA/cm^2. As the intensity of ilumination power increases, the high value of photocurrent is extracted from the devices, implying the more electron-hole (*e-h*) pairs generation [124]. The relationship between photogenerated current and illumination power intensity is expressed by a power law function [124]:

$$I_{light} = C.P_{in}^{\alpha} \qquad (4.6)$$

where C, P_{in} and α symbolize the scaling factor, incident power and power exponent, respectively. The value of α ranges from 0.5 and 1, indicating the trap states in a device [124-126]. For a trap-free device, the value of α is equal to 1 [127]. However, the value of α deviates from 1 depending on the device trap states. By substituting

power law formula (4.6) in *PR* formula (2.7), the following eguation is obtained for calculation of the value of *PR*.

$$PR = \frac{I_{light} - I_{dark}}{P_{in}\,A} = \frac{C.{P_{in}}^{\alpha}}{P_{in}A} - \frac{I_{dark}}{P_{in}A} \qquad (4.7)$$

If we write *y(x)* for *PR*, *x* for P_{in}, *Y1* for *C/A*, and *Y2* for I_{dark}/A, the more compact version of *PR* formula is acquired as:

$$y(x) = Y1x^{-\alpha+1} - Y2x \qquad (4.8)$$

The graph of *PR* values of the samples with respect to $1/P_{in}$ is illustrated in Figure 4.13. By fitting the plot of *PR* versus $1/P_{in}$ with equation (4.8), one can estimate the maximum limit of *PR* at $\left[\frac{dy(x)}{dx} \to 0\right]$.

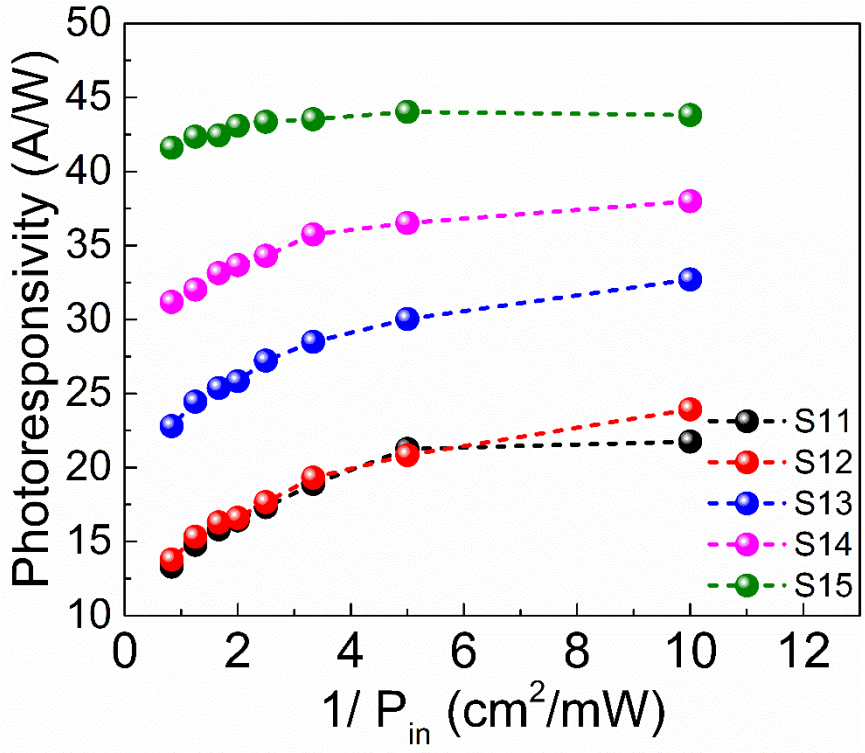


Figure 4.13 Graph of *PR* values of the samples with respect to $1/P_{in}$.

If we take the derivation of *y(x)* and find the point where *y(x)* is equal to zero, we can get the P_{in}^{*} value where *PR* will take the maximum value. The following equation (4.9) gives the value of P_{in}^{*} :

$$P_{in}^{*} = \left[\frac{Y2}{Y1(-\alpha+1)}\right]^{\frac{1}{\alpha}} \qquad (4.9)$$

Eventually, the value of P_{in}^{*} can be found by fitting the plot of *y(x)* versus *x* with equation (4.8). The obtained parameters are listed in Table 4.5.

Table 4.5 The obtained parameters displayed by each device.

Devices	Parameters		
	α	$P_{in}^{*}(\mathrm{mW/cm})$	PR^{*} (A/W)
S11	0.64	0.1020	21.91
S12	0.75	0.0205	28.90
S13	0.83	0.0300	35.48
S14	0.89	0.0535	38.73
S15	0.96	0.1330	43.91

where *PR** stands for the exhibited *PR* value by each device. Let us now focus on correlation between α and *PR* values of the devices. Figure 4.14 delineates the linear variation of *PR* values with respect to α values of the samples.

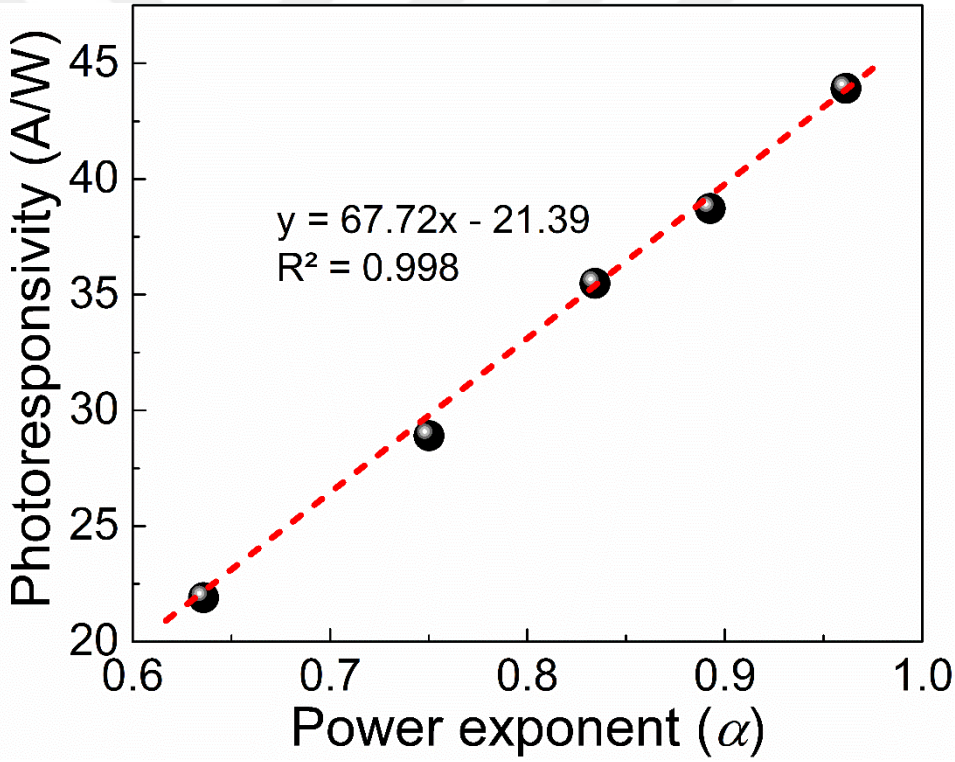


Figure 4.14 Plot of *PR* values with respect to α values of the samples

The dependency of *PR* on the value of power exponent can be obtained as the following:

$$PR = 67.72\alpha - 21.39 \qquad (4.10)$$

By knowing the value of α in Equation (7), the maximum values of *PR* of the devices can be calculated. Herein, the maximum value of *PR* for the device having *n*-SnO_2/*p*-

Si structure is found to be 46.3 A/W. The maximum attainable value of *PR* of photodetectors can be estimated for the trap free state (when α is equal to 1) [127]. For a high-performance device, the high value of α is highly desirable for efficient charge generation and transportation characteristics.

The transient-response curves of the samples are obtained under switching UV irradiation of 311 nm. The rise/decay time (t_r/t_d) of the fabricated devices is in milliseconds range. The determined transient-response characteristics of the sample (S15) are depicted in Figure 4.15. From the inset of Figure 4.15, one can observe that the sample (S15) achieves τ_r of 62 ms and τ_d of 64 ms.

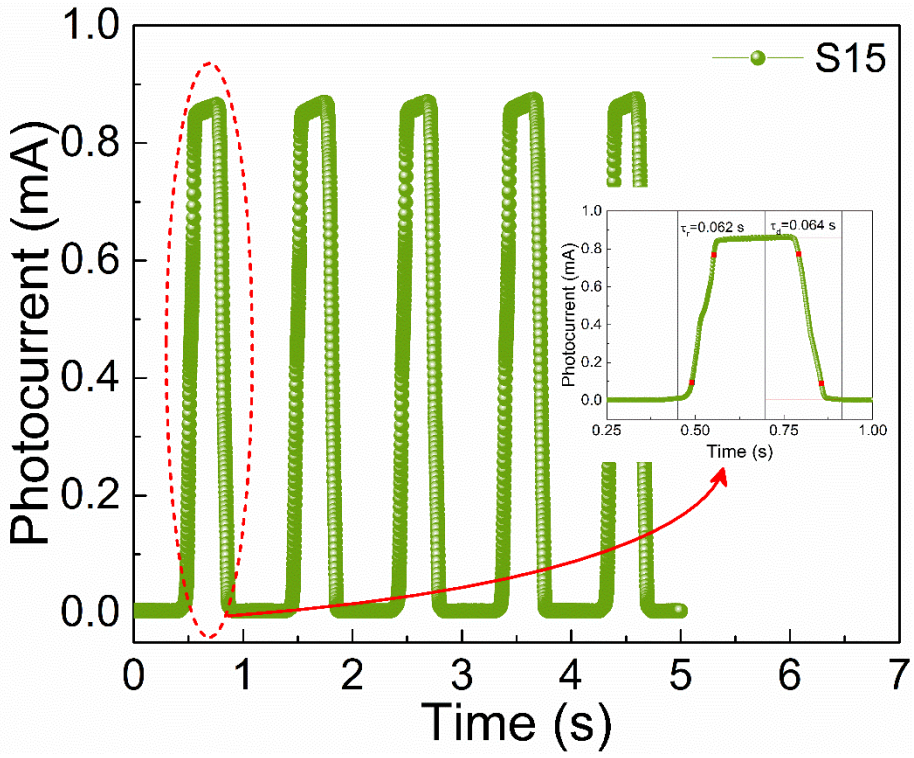


Figure 4.15 The transient-response characteristics of the sample (S15). The inset shows the enlarged figure of the response behavior of the sample (S15).

Further, we calculate the other photodetector parameters and compare the results with other reported works. Table 4.16 gives the comparison of calculated parameters of the result of sample (S15) and other reported investigations. As can be seen, our device (S15) performs comparable to other reported studies.

Table 4.6 Comparison of calculated parameters of the result of sample (S15) and other reported UV photodetectors.

Devices	Parameters						
	PR (A/W)	*D** (Jones)	*PS*	*LDR* (dB)	*NEP* (W)	t_r / t_d (ms)	Ref.
SnO_2/*p*-Si	43.91	$2.66x10^{13}$	101.72	40.15	$3.76x10^{-14}$	62/64	This study
SnO_2/*p*-Si	22.73	$1.58x\ 10^{13}$	-	51	-	37/27	[116]
SnO_2/*p*-Si	2.16	1.38×10^{13}	532	-	$7.26x10^{-14}$	40/34	[117]
TiO_2/*p*-Si	6.74	$1.31x10^{12}$	$3.86x10^{3}$	31.9	$7.62x10^{-13}$	0.13/0.12	[89]
ZnO/*p*-NiO	21.80	$1.60x10^{12}$	100	-	-	-	[90]
Ga_2O_3/NSTO	43.31	-	10.20	-	-	1080/650	[128]
WS_2/SiO_2/Si	53.30	1.22×10^{11}	-	-	-	-	[124]
$Mg_xZn_{1-x}O$/Si	0.4	$1.80x10^{10}$	-	-	$1.90x10^{-11}$	~100	[129]

As a result, it is noticed that the photocurrent values of the samples increases with different slopes with increased light power intensity. It is concluded that the trend of increase of photocurrent values differed from one sample to another depending on the trap states in the devices. Eventually, the dependency of *PR* values on the value of power exponent of the samples has been revealed. The maximum achievable *PR* limit of our devices is detemined to be 46.3 A/W.

4.4 Investigation of the photovoltaic (PV) performance of the devices

Based on the publication “Comprehensive understanding of the role of emitter layer thickness for metal-oxide semiconductors-based solar cells”, K. Ozel, A. Yildiz, IEEE Journal of Photovoltaics, 2021 [78], this section is reproduced (or “reproduced in part") with permission from IEEE Journal of Photovoltaics. Copyright 2021 IEEE.

Constructed with a metal oxide (MO_x) emitter layer, *p-n* heterojunction solar cells challenge their homojunction counterparts as they efficiently enable electricity generation from solar energy. The convenience of deposition of MO_x semiconductors on the *p*-Si absorber layer has offered an easy route for the fabrication of *p-n* heterojunction based solar cells. A variety of deposition methods have been adopted by researchers for the deposition of MO_x layer [130-134]. Among them,

hydrothermal route allows homogeneous coating of the MO_x layer in a feasible and cost-effective way [135]. To date, notable efforts have been devoted to fabricating heterostructure-based solar cells. Narzary et al. achieved to fabricate Al/ZnO/*p*-Si/Al heterojunction photovoltaic cell exhibiting *PCE* of 2.22% [136]. Elsaeedy et al. investigated the effect of TiO_2 emitter thickness on the photovoltaic performance of In/TiO_2/*p*-Si/Al heterojunction photovoltaic cells [137]. Pietruszka et al. reported that the optimal thickness of the emitter layer of heterojunction solar cells should be between 300 nm and 500 nm [138].

The photovoltaic properties of the devices with the final device structure (S7) designed within the scope of this thesis were evaluated under simulated solar irradiation. Herein, the photovoltaic properties of three devices with the *n*-SnO_2 thicknesses of 206, 304 and 391 nm were demonstrated. Investigation of PV properties for samples having the 206, 304 and 391 nm thick emitter layer has been provided important information about understanding the role of emitter thickness on device performance in heterojunction based solar cells.

As in the previous sections, the basic structure of the devices was designed using sol-gel spin coating and hydrothermal method. The *n*-SnO_2 layer thickness of the devices having structured of n-$SnO_{2\text{-NS}}$/n-$SnO_{2\text{-TF}}$/p-Si was adjusted as 206, 304 and 396 nm by optimization of the hydrothermal deposition process. The devices with 206, 304 and 396 nm thick SnO_2 layer were named S16, S17, and S18, respectively.

The top-view and side-view SEM images of the resultant layers are manifested in Figure 4.16. As delineated in inset of Figure 4.16, the values of *n*-SnO_2 thickness of the cells are estimated to be 206, 304 and 391 nm. The surface morphologies of the samples have dense structure, endowing the cells with enhanced light harvesting capability.

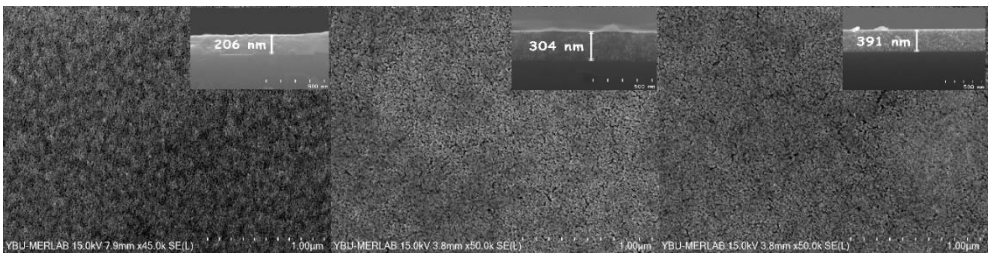


Figure 4.16 Top-view and side-view SEM images of *n*-SnO_2 layer of the cells.

The absorbance and transmittance profiles of the deposited *n*-SnO_2 (206 nm), *n*-SnO_2 (304 nm), and *n*-SnO_2 (396 nm) layers are shown in Figure 4.17. The light harvesting capacity of the cells is improved with the increase in the thickness of *n*-SnO_2 layer. From transmittance spectra, one can notice that the average transmittance of *n*-SnO_2 layers is in the range of 82%-84% within the wavelength range of 300–1000 nm. In addition, the Tauc plots of the samples are given in the inset of Figure 4.17. The band gap values of the samples are found to be 3.93 eV for *n*-SnO_2 (206 nm), 3.89 eV for *n*-SnO_2 (304 nm) and 3.86 eV for *n*-SnO_2 (391 nm) emitter layers, respectively.

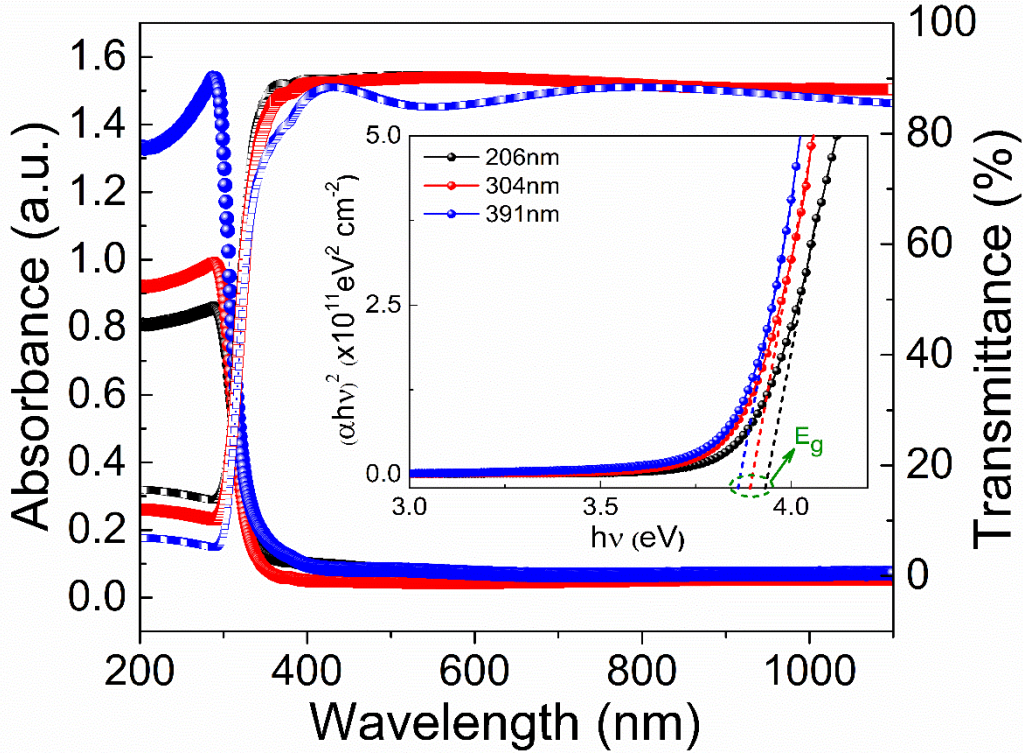


Figure 4.17 The absorbance and transmittance profiles of *n*-SnO_2 (206 nm), *n*-SnO_2 (304 nm), and *n*-SnO_2 (396 nm). The inset shows the Tauc plots of the samples.

The dark current-voltage (*I-V*) curves of the samples are measured to analyze the nature of *p-n* junction. Figure 4.18 shows the dark current-voltage (*I-V*) curves of the fabricated devices. The values of leakage current (I_o), ideality factor (*n*), and p-n junction barrier height ($Ø_{bi}$) are estimated from Figure 4.18. The values of these parameters are determined as 136 nA, 3.8, and 0.75 eV for S16; 303 nA, 4, and 0.73 eV for S17; 378 nA, 4.1, and 0.72 eV for S18. As the *n*-SnO_2 layer becomes thicker, the values of I_o and *n* increase, but the value of $Ø_{bi}$ diminishes. These changes limit the maximum achievable *PCE* values of the cells.

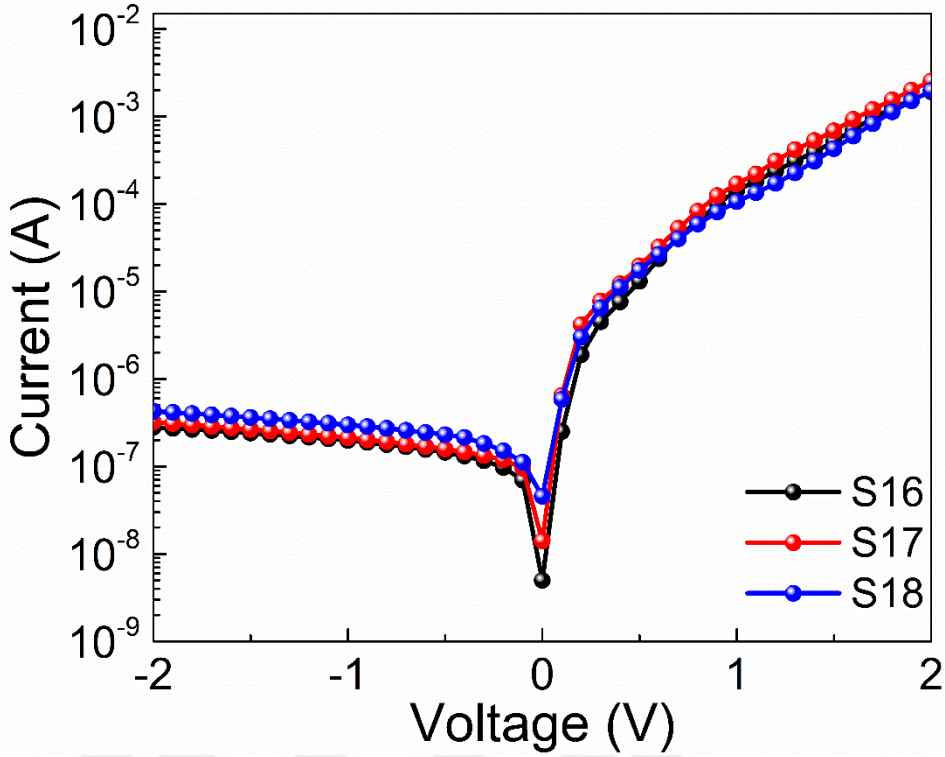


Figure 4.18 The dark current-voltage (*I-V*) plots of the samples

The photovoltaic properties of the fabricated cells are investigated under standard one (1) sun AM1.5 irradiation conditions. The curves of power-voltage (*P-V*) and current density-voltage (*J-V*) are illustrated in Figure 4.19. Based on the *P-V* curves, the highest power density (3.09 mW/cm^2) is delivered by S18.

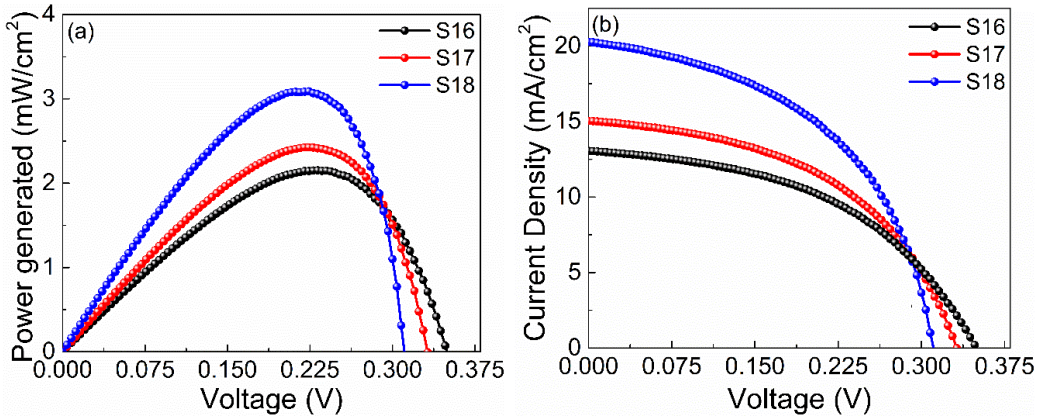


Figure 4.19 *P-V* and *I-V* characteristics of cells.

Table 4.6 gives the photovoltaic parameters i.e, short-circuit current density (J_{sc}), open-circuit voltage (V_{oc}), fill factor (*FF*), and power conversion efficiency (*PCE*) of the cells. As observed, the J_{sc} values of the cells increase with increasing thickness of

n-SnO_2 layer. The increased absorption property and decreased band gap size provides to extract the enhanced J_{sc} values from the samples. However, the decrease in band gap size results in decreased V_{oc} values of the samples.

Table 4.7 Photovoltaic parameters of the cells.

Devices	Thickness (nm)	J_{sc} (mA/cm^2)	V_{oc} (V)	*FF* (%)	*PCE* (%)
S16	206	13.05	0.348	47.36	2.15
S17	304	15.03	0.332	48.58	2.42
S18	391	20.28	0.312	48.84	3.09

Figure 4.20 depicts $1/C^2$-V graphs of the fabricated devices. The values of acceptor concentration (N_a) and built-in potential (V_{bi}) of the devices are estimated from the slope and x-intercept of $1/C^2$-V graphs, respectively. The values of N_a and V_{bi} are determined to be 7.18x10^{15} cm^{-3}, 0.69 V for S16; 7.44x10^{15} cm^{-3}, 0.68 V for S17; 7.63X10^{15} cm^{-3}, 0.67 V for S18.

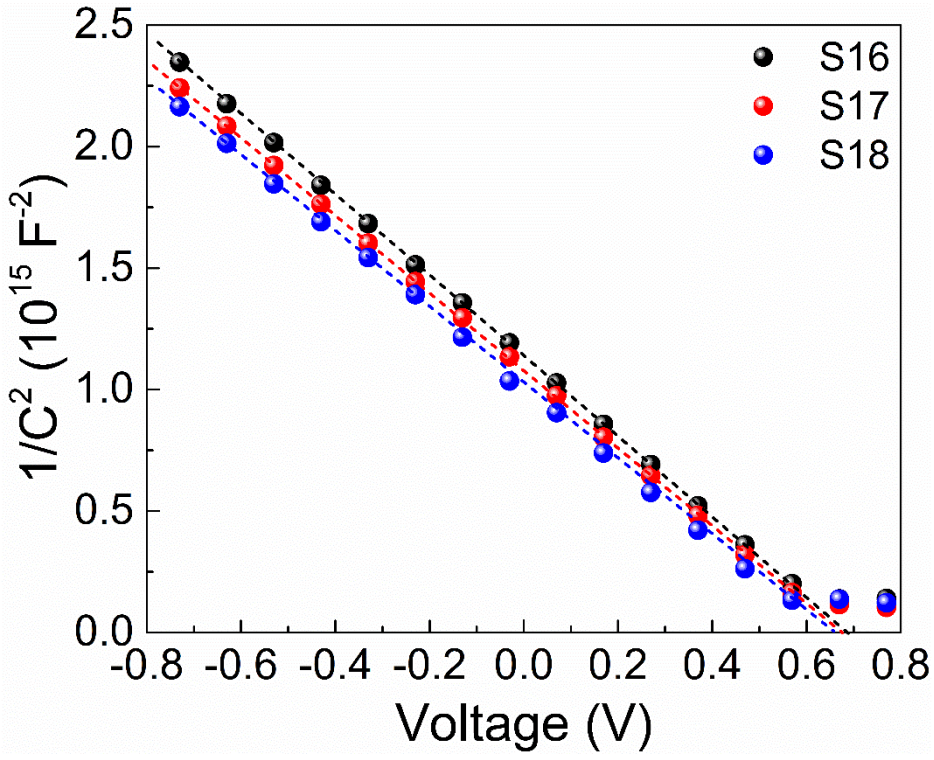


Figure 4.20 $1/C^2$-V graphs of the fabricated devices.

In addition, the values of donor concentration (N_d) and depletion region width of the samples can be obtained by utilizing the determined values of N_a and V_{bi}. The depletion region plays an important role in the generation and separation of charge

carriers (See Figure 4.21). The width of depletion region (W) of the fabricated cells can be determined using the following equation [84].

$$W = \left[\frac{2\varepsilon_n\varepsilon_p(N_a+N_d)^2V_{bi}}{qN_aN_d(\varepsilon_nN_d+\varepsilon_pN_a)}\right]^{1/2} \quad (4.11)$$

Here, the values of $\mathcal{E}_n$ and $\mathcal{E}_p$ are 9.86 and 11.7, respectively. the values of W for the samples are calculated to be 432 nm for S16, 461 nm for S17, and 504 nm for S18. Note that the values of W are increased as the n-SnO_2 layer becomes thicker. The change in the values of W significantly affects the J_{sc} values of the cells. The high values of W increase the probability of generation of charge carriers, yielding to higher values of J_{sc}. Utilizing the W values of the samples, the J_{sc} values can be obtained by the following equation [87].

$$J_{sc} = q\ G\ (L_n + W + L_P) \quad (4.12)$$

where G stands for the generation rate. L_n and L_p represent the diffusion length of electrons and holes, respectively. As can be clearly seen from the equation (4.12), the variation in W values will directly reflect on the J_{sc} values.

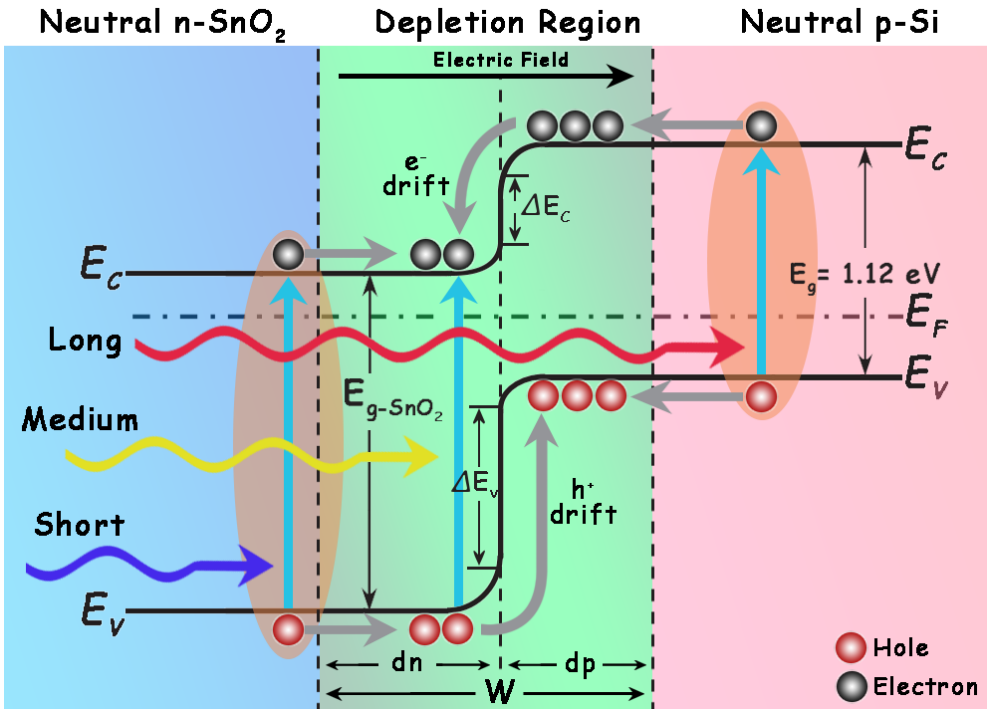


Figure 4.21 Energy band diagram of n-SnO_2/p-Si heterojunction based solar cell under equilibrium condition.

Ultimately, our findings manifest that *n*-$SnO_{2\text{-}NS}$/*n*-$SnO_{2\text{-}SL}$/*p*-Si heterostructures have potentials for the fabrication of solar cells. The nature and thickness of *n*-SnO_2 layer plays a vital role in determining the photovoltaic performance of the *n*-SnO_2/*p*-Si heterostructure-based solar cells. The photovoltaic parameters of the devices vary with the change in the values of *n*-SnO_2 thickness.

CHAPTER 5

CONCLUSIONS

The design, fabrication, and characterization of *n*-SnO_2/*p*-Si heterostructures for UV photodetectors and photovoltaic applications have been presented in this thesis. The heterostructures were fabricated by utilizing spin-coating and hydrothermal deposition techniques. The structural, morphological, optical and electrical properties of the *n*-SnO_2 layers and *n*-SnO_2/*p*-Si heterostructures were investigated by measurements of X-ray diffraction (XRD) measurements, scanning electron microscopy (SEM), UV-Vis spectroscopy, current–voltage (*I*-*V*) and capacitance-voltage (*C*-*V*). The design process includes the creation of the architecture of the devices, the integration of the seed layer and the nanostructured layer into the basic p-n heterojunction structure. Firstly, the effect of seed layer type on the performance of the photodetectors are investigated by characterizing five number of devices. Metal oxide semiconductors such as *n*-SnO_2, *n*-ZnO and *n*-TiO_2 were used as the seed layer. The results reveal that the deposition of seed layer underneath the nanostructured layer is of utmost importance in achieving high-performance devices. Additionally, it is noteworthy to say that the presence of nanostructured layer enhances the light harvesting properties of the devices. The device constructed with a *n*-SnO_2 nanostructured layer integrated *n*-SnO_2/*p*-Si heterostructure (S3) exhibited superior performance than others. This device (S3) delivered the photo-responsivity of 110 mA/W, but the performance limit of this device needed to improve. The obtained results revealed that (i) *n*-SnO_2 (Nanostructured) /*n*-SnO_2 (thin film)/*p*-Si heterostructures have potentials for the fabrication of UV photodetectors, (ii) the growth mechanism of a nanostructured layer is affected by the nature of the seed layer, (iii) introducing the *n*-SnO_2 nanostructured layer onto the deposited seed layer improves the device performance. After designing basic structure, the seed and nanostructured layer of the devices were optimized to improve the performance of the devices having structure of *n*-SnO_2 (Nanostructured)/*n*-SnO_2 (seed layer)/*p*-Si. The seed layer solution of the devices was revised, and the performance levels of the devices have reached the A/W level. Subsequently, the nanostructured layer of the

devices was examined and four different devices with different nanostructured layer were fabricated and the best-performing device (S7) was determined. This device (S7) yielded a photo-responsivity of 22.73 A/W, a photo-sensitivity of 351.75, a detectivity of 1.58×10^{13} Jones. It is notable to state that the performance level of this device is comparable to its counterparts and even surpasses the level of those devices. The findings manifest that (i) the maximum response of our devices corresponds to UV-B spectrum, (ii) the porous nature of nanostructured layer ameliorates the absorption characteristics of the samples by enhancing the light-matter interaction, (iii) the depth of band bending affects the separation of photogenerated carriers. In the light of the obtained results, the performance limit of the final device (S7) was probed in terms of the trap states in device structure. The photo-response properties of the fabricated photodetectors were obtained under different values of illumination power intensity to extract the maximum photo-responsivity values of the devices. The best performing device (S15) with a power exponent value of 0.96 exhibited an outstanding photo-responsivity of 43.91 A/W at a low incident power of 0.133 mW/cm^2. The results of this section unveil that (i) the presence of trap states in device structure deteriorates the performance of the devices, (ii) the photocurrent extracted from devices sub-linearly rises up with increasing incident light power, (iii) maximum achievable photo-responsivity of our devices is found to be 46.3 A/W. Afterwards, the photovoltaic performance of the produced devices was investigated under simulated solar irradiation. As only the devices having final structure showed *PCE* over 2%, the samples with the *n*-SnO_2 thicknesses of 206, 304, and 391nm were fabricated to analyze the role of emitter layer thickness on the photovoltaic performance of the *n*-SnO_2/*p*-Si heterojunction based solar cells. The device with *n*-SnO_2 thickness of 391 nm supplied the largest *PCE* of 3.09% (J_{sc} of 20.28 mA/cm^2, V_{oc} of 0.312 V, and *FF* of 48.84%). The outcomes disclose that (i) the photovoltaic performance of heterojunction based solar cells is firmly dependent on the thickness of *n*-type top layer, (ii) the change in thickness of *n*-type layer directly affects the photovoltaic parameters of the devices, (iii) the increase in thickness of *n*-SnO_2 and the width of depletion region enhances the J_{sc} values of the devices, (iv) the deterioration in leakage current values results in decreased V_{oc} values of the samples.

In conclusion, eighteen (18) number of devices have been fabricated and characterized in this thesis. The optimum device architecture was determined for UV photodetectors and heterojunction based solar cells. Eventually, this work has revealed a route for the fabrication of *n*-SnO_2/*p*-Si heterostructures for UV photodetector and photovoltaic cell applications.

For further investigation on *n*-SnO_2/*p*-Si heterostructure-based optoelectronic devices, the following modifications can be applied in purpose of enhancing photodetection and photovoltaic performance of the devices.

- The structural and optical properties of *n*-SnO_2 seed layer can be optimized to minimize the trap states and recombination rate of the devices. In principle, the presence of a high-quality SnO_2 layer improves the charge transport characteristics of the devices, as it reduces the interface resistance values of the devices.

-The performance of the devices can be improved by designing multilayer structured emitter layer. Multilayer structured design provides high light harvesting performance to the devices thanks to its property of absorption of different spectra with different layers.

- Light trapping approaches such as surface texturing, anti-reflection coating can be applied to reduce the reflection of incident light. These approaches endow the devices with superior absorption properties, thus contributing to their performance.

- Plasmonic nanoparticles can be used to improve light harvesting characteristics of the devices. Depending on the shape, type, location and concentration of these nanoparticles, an improvement in the absorption and scattering characteristics of the devices can be achieved.

REFERENCES

[1] Wu, C., Du, B., Luo, W., Liu, Y., Li, T., Wang, D., et al. Highly Efficient and Stable Self-Powered Ultraviolet and Deep-Blue Photodetector Based on $Cs_2AgBiBr_6/SnO_2$ Heterojunction. Advanced Optical Materials, 6(22), 1800811. 2018

[2] Qin, Y., Li, L., Zhao, X., Tompa, G. S., Dong, H., Jian, et al. Metal–semiconductor–metal ε-Ga2O3 solar-blind photodetectors with a record-high responsivity rejection ratio and their gain mechanism. ACS Photonics, 7(3), 812-820. 2020

[3] Ko, K. B., Ryu, B. D., Han, M., Hong, C. H., Doan, T. A., & Cuong, T. V. Inserting dome shape microstructure for enhancement of ultraviolet photodetector performance of n-ZnO nanorods/p-Si heterojunction. Journal of Alloys and Compounds, 823, 153884. 2020

[4] Al-Hardan, N. H., Hamid, M. A., Ahmed, N. M., Shamsudin, R., & Othman, N. K. Ag/ZnO/p-Si/Ag heterojunction and their optoelectronic characteristics under different UV wavelength illumination. Sensors and Actuators A: Physical, 242, 50-57. 2016

[5] Sang, L., Liao, M., & Sumiya, M. A comprehensive review of semiconductor ultraviolet photodetectors: from thin film to one-dimensional nanostructures. Sensors, 13(8), 10482-10518. 2013

[6] Chen, T. P., Young, S. J., Chang, S. J., Hsiao, C. H., & Hsu, Y. J. Bending effects of ZnO nanorod metal–semiconductor–metal photodetectors on flexible polyimide substrate. Nanoscale research letters, 7(1), 1-6. 2012

[7] Ma, G., Du, R., Cai, Y. N., Shen, C., Gao, X., Zhang, Y., et al. Improved power conversion efficiency of silicon nanowire solar cells based on transition metal oxides. Solar Energy Materials and Solar Cells, 193, 163-168. 2019

[8] Chen, Y. C., Lu, Y. J., Liu, Q., Lin, C. N., Guo, J., Zang, J. H., et al. Ga_2O_3 photodetector arrays for solar-blind imaging. Journal of Materials Chemistry C, 7(9), 2557-2562. 2019

[9] Mardare, D., Yildiz, A., Girtan, M., Manole, A., Dobromir, M., Irimia, M., et al. Surface wettability of titania thin films with increasing Nb content. Journal of Applied Physics, 112(7), 073502. 2012

[10] Yildiz, A., Lisesivdin, S. B., Kasap, M., & Mardare, D. High temperature variable-range hopping conductivity in undoped TiO_2 thin film, Optoelectron. Adv. Mater.-Rapid Commun. 1 (10), 531–533. 2007

[11] Yildiz, A., Yurduguzel, B., Kayhan, B., Calin, G., Dobromir, M., & Iacomi, F. Electrical conduction properties of Co-doped ZnO nanocrystalline thin films. Journal of Materials Science: Materials in Electronics, 23(2), 425-430. 2012

[12] Ozel, K., Kosalay, I., Atilgan, A., Atli, A., Yildiz, Z. K., & Yildiz, A. Performance improvement of dye-sensitized solar cells with AZO and BZO blocking layers. J. New Mater. Electrochem. Syst. 21(4), 227–231. 2018

[13] Serin, N., Yildiz, A., Alsaç, A. A., & Serin, T. Estimation of compensation ratio by identifying the presence of different hopping conduction mechanisms in SnO_2 thin films. Thin Solid Films, 519(7), 2302-2307. 2011

[14] Ozel, K., Atilgan, A., Koksal, N. E., & Yildiz, A. A route towards enhanced UV photo-response characteristics of SnO_2/p-Si based heterostructures by hydrothermally grown nanorods. Journal of Alloys and Compounds, 849, 156628. 2020

[15] Sbeta, M., & Yildiz, A. Optical response enhancement of GZO/p-Si heterostructures via metal nanoparticles. Materials Research Express, 6(8), 085018. 2019

[16] Yildiz, Z. K., Atilgan, A., Atli, A., Özel, K., Altinkaya, C., & Yildiz, A. Enhancement of efficiency of natural and organic dye sensitized solar cells using thin film TiO_2 photoanodes fabricated by spin-coating. Journal of Photochemistry and Photobiology A: Chemistry, 368, 23-29. 2019

[17] Atli, A. Atilgan, A. & Yildiz, A. Multi-layered TiO_2 photoanodes from different precursors of nanocrystals for dye-sensitized solar cells, Solar Energy, 173, 752–758. 2018

[18] Tharsika, T., Thanihaichelvan, M., Haseeb, A. S. M. A., & Akbar, S. A. Highly sensitive and selective ethanol sensor based on ZnO nanorod on SnO_2 thin film fabricated by spray pyrolysis. Frontiers in Materials, 6, 122. 2019

[19] Liu, J., Wang, T., Wang, B., Sun, P., Yang, Q., Liang, X., et al. Highly sensitive and low detection limit of ethanol gas sensor based on hollow ZnO/SnO_2 spheres composite material. Sensors and Actuators B: Chemical, 245, 551-559. 2017

[20] Singh, K., Malakar, R., Narzary, R., Kakoty, P., & Mondal, B. Hydrogen sensing properties of pure and composites of ZnO and SnO_2 particles: Understanding sensing mechanism. Sensor Letters, 15(9), 771-778. 2017

[21] Lee, S. J., Hwang, C. S., Pi, J. E., Yang, J. H., Byun, C. W., Chu, H. Y., et al. High-Performance Amorphous Multilayered ZnO-SnO_2 Heterostructure Thin-Film Transistors: Fabrication and Characteristics. Etri journal, 37(6), 1135-1142. 2015

[22] Bakr, Z. H., Wali, Q., Yang, S., Yousefsadeh, M., Padmasree, K. P., Ismail, J., et al. Characteristics of ZnO–SnO_2 composite nanofibers as a photoanode in dye-sensitized solar cells. Industrial & Engineering Chemistry Research, 58(2), 643-653. 2018

[23] Ali, A., Ammar, M., Yahya, Z., Waqas, M., Jamal, M. A., & Salhabi, E. H. M. A honeycomb-like ZnO/SnO_2 nanocomposite on nickel foam for high-performance asymmetric supercapacitors. New Journal of Chemistry, 43(26), 10583-10589. 2019

[24] Faisal, M., Ibrahim, A. A., Harraz, F. A., Bouzid, H., Al-Assiri, M. S., & Ismail, A. A. SnO_2 doped ZnO nanostructures for highly efficient photocatalyst. Journal of Molecular Catalysis A: Chemical, 397, 19-25. 2015

[25] Zeng, W., Zhang, H., Li, Y., Chen, W., & Wang, Z. Hydrothermal synthesis of hierarchical flower-like SnO_2 nanostructures with enhanced ethanol gas sensing properties. Materials Research Bulletin, 57, 91-96. 2014

[26] Sharma, A., Tomar, M., & Gupta, V. SnO_2 thin film sensor with enhanced response for NO2 gas at lower temperatures. Sensors and actuators B: chemical, 156(2), 743-752. 2011

[27] Sinha, S. K., Rakshit, T., Ray, S. K., & Manna, I. Characterization of ZnO–SnO_2 thin film composites prepared by pulsed laser deposition. Applied surface science, 257(24), 10551-10556. 2011

[28] Martínez, D. T., Pérez, R. C., Delgado, G. T., & Ángel, O. Z. Structural, morphological, optical and photocatalytic characterization of ZnO–SnO_2 thin films prepared by the sol–gel technique. Journal of Photochemistry and Photobiology A: Chemistry, 235, 49-55. 2012

[29] Liu, Y., Koep, E., & Liu, M. A highly sensitive and fast-responding SnO_2 sensor fabricated by combustion chemical vapor deposition. Chemistry of materials, 17(15), 3997-4000. 2005

[30] Caglar, Y., Caglar, M., Ilican, S., & Yakuphanoglu, F. Determination of the electronic parameters of nanostructure SnO_2/p-Si diode. Microelectronic engineering, 86(10), 2072-2077. 2009

[31] Nagatomo, T., Endo, M., & Omoto, O. Fabrication and characterization of SnO_2/n-Si solar cells. Japanese Journal of Applied Physics, 18(6), 1103. 1979

[32] Peršin, M., Vlahović, B., & Urli, N. Some electrical and photovoltaic properties of poly-Si/SnO_2 heterojunction. Vacuum, 40(1-2), 209-211. 1990

[33] Altındal, Ş., Karadeniz, S., Tuğluoğlu, N., & Tataroğlu, A. The role of interface states and series resistance on the I–V and C–V characteristics in Al/SnO_2/p-Si Schottky diodes. Solid-State Electronics, 47(10), 1847-1854. 2003

[34] Ling, T. R., & Tsai, C. M. Influence of nano-scale dopants of Pt, CaO and SiO_2, on the alcohol sensing of SnO_2 thin films. Sensors and Actuators B: Chemical, 119(2), 497-503. 2006

[35] Juybari, H. A., Bagheri-Mohagheghi, M. M., Ketabi, S. A., & Shokooh-Saremi, M. Fabrication and characterization of transparent p–n and p–i–n heterojunctions prepared by spray pyrolysis technique: Effect of post-annealing process and intrinsic middle layer. Physica E: Low-dimensional Systems and Nanostructures, 43(1), 93-96. 2010

[36] Maleki, M., & Rozati, S. M. Dependence of Si/SnO_2 Heterojunction Properties on Growth Temperature and Type of Silicon. Chemical Vapor Deposition, 19(7-8-9), 290-294. 2013

[37] Lou, Z., Yang, X., Chen, H., & Liang, Z. Flexible ultraviolet photodetectors based on ZnO–SnO_2 heterojunction nanowire arrays. Journal of Semiconductors, 39(2), 024002. 2018

[38] Jiang, Q., Zhang, X., & You, J. SnO_2: a wonderful electron transport layer for perovskite solar cells. Small, 14(31), 1801154. 2018

[39] DiMarco, B. N., Sampaio, R. N., James, E. M., Barr, T. J., Bennett, M. T., & Meyer, G. J. Efficiency Considerations for SnO_2-Based Dye-Sensitized Solar Cells. ACS applied materials & interfaces, 12(21), 23923-23930. 2020

[40] Yuan, Z., Li, D., Wang, M., Chen, P., Gong, D., Cheng, P., et al. Electroluminescence of SnO_2/p-Si heterojunction. Applied Physics Letters, 92(12), 121908. 2008

[41] Karadeniz, S., Tuğluoğlu, N., Serin, T., & Serin, N. The energy distribution of the interface state density of SnO_2/p-Si (1 1 1) heterojunctions prepared at different substrate temperatures by spray deposition method. Applied surface science, 246(1-3), 30-35. 2005

[42] Savioli, J., Gavin, A. L., Lucid, A. K., & Watson, G. W. The structure and electronic structure of tin oxides. In Tin Oxide Materials, pp. 11-39, Elsevier. 2020

[43] Lu, Y., SnO_2 Thin Films- Chemical Vapor Deposition and Characterization, Doctoral Dissertation, University of Giessen, 2015

[44] Nagasawa, M., Shionoya, S., & Makishima, S. Vapor reaction growth of SnO_2 single crystals and their properties. Japanese Journal of Applied Physics, 4(3), 195. 1965

[45] Dawar, A. L., & Joshi, J. C. Semiconducting transparent thin films: their properties and applications. Journal of Materials Science, 19(1), 1-23. 1984

[46] Choudhary, R. J., Ogale, S. B., Shinde, S. R., Kulkarni, V. N., Venkatesan, T., Harshavardhan, K. S., et al. Pulsed-electron-beam deposition of transparent conducting SnO_2 films and study of their properties. Applied physics letters, 84(9), 1483-1485. 2004

[47] Yang, G., Qin, P., Fang, G., & Li, G. Tin oxide (SnO_2) as effective electron selective layer material in hybrid organic–inorganic metal halide perovskite solar cells. Journal of energy chemistry, 27(4), 962-970. 2018

[48] Shewale, P. S., Sim, K. U., Kim, Y. B., Kim, J. H., Moholkar, A. V., & Uplane, M. D. Structural and photoluminescence characterization of SnO2: F thin films deposited by advanced spray pyrolysis technique at low substrate temperature. Journal of luminescence, 139, 113-118. 2013

[49] Caravaca, M. A., Kosteski, L. E., Miño, J. C., D'Ambra, R. B., Uberti, B., & Casali, R. A. Model for Vickers microhardness prediction applied to SnO_2 and TiO_2 in the normal and high pressure phases. Journal of the European Ceramic Society, 34(15), 3791-3800. 2014

[50] Mun, H., Yang, H., Park, J., Ju, C., & Char, K. High electron mobility in epitaxial SnO_{2-x} in semiconducting regime. APL Materials, 3(7), 076107. 2015

[51] Turkes, P., Pluntke, C., & Helbig, R. Thermal conductivity of SnO_2 single crystals. Journal of Physics C: Solid State Physics, 13(26), 4941. 1980

[52] Ji, Y. C., Zhang, H. X., Zhang, X. H., & Li, Z. Q. Structures, optical properties, and electrical transport processes of SnO_2 films with oxygen deficiencies. physica status solidi (b), 250(10), 2145-2152. 2013

[53] Islam, M. N., & Hakim, M. O. Electron affinity and work function of polycrystalline SnO 2 thin film. Journal of materials science letters, 5(1), 63-65. 1986

[54] Summitt, R. Infrared Absorption in Single-Crystal Stannic Oxide: Optical Lattice-Vibration Modes. Journal of Applied Physics, 39(8), 3762-3767. 1968

[55] Altinkaya, C., Aydin, E., Ugur, E., Isikgor, F. H., Subbiah, A. S., De Bastiani, M., et al. Tin Oxide Electron-Selective Layers for Efficient, Stable, and Scalable Perovskite Solar Cells. Advanced Materials, 33(15), 2005504. 2021

[56] Kim, J. Y., Kim, E. R., Han, Y. K., Nam, K. H., & Ihm, D. W. Highly transparent tin oxide films prepared by DC magnetron sputtering and its liquid crystal display application. Japanese journal of applied physics, 41(1R), 237. 2002

[57] Jakob, M. H., Dong, B., Gutsch, S., Chatelle, C., Krishnaraja, A., Weber, W., et al. Label-free SnO_2 nanowire FET biosensor for protein detection. Nanotechnology, 28(24), 245503. 2017

[58] Gotlib-Vainstein, K., Gouzman, I., Girshevitz, O., Bolker, A., Atar, N., Grossman, E., et al. Liquid phase deposition of a space-durable, antistatic SnO_2 coating on Kapton. ACS applied materials & interfaces, 7(6), 3539-3546. 2015

[59] Lin, J. Y., Lien, S. Y., Liao, H. Z., Wang, C. C., Nautiyal, A., & Lin, Y. H. Titanium-doped Indium-Tin-Oxide Anti-Reflection Coating for Poly-Si Solar Cells. Applied Mechanics and Materials, 284, 250-254. 2013

[60] Ma, Y., Qu, Y., & Zhou, W. Surface engineering of one-dimensional tin oxide nanostructures for chemical sensors. Microchimica Acta, 180(13-14), 1181-1200. 2013

[61] Hudaya, C., Jeon, B. J., & Lee, J. K. High thermal performance of SnO_2: F thin transparent heaters with scattered metal nanodots. ACS applied materials & interfaces, 7(1), 57-61. 2015

[62] Karadeniz, S., Tuğluoğlu, N., & Serin, T. Substrate temperature dependence of series resistance in Al/SnO_2/p-Si (111) Schottky diodes prepared by spray deposition method. Applied surface science, 233(1-4), 5-13. 2004

[63] Krebsbach, P., Schlisske, S., Strobel, N., Seiberlich, M., Ruiz-Preciado, L. A., Rainer, C., et al. Inkjet-Printed Tin Oxide Hole-Blocking Layers for Organic Photodiodes. ACS Applied Electronic Materials, 3(11), 4959-4966. 2021

[64] Serin, T., Serin, N., Karadeniz, S., Sarı, H., Tuğluoğlu, N., & Pakma, O. Electrical, structural and optical properties of SnO_2 thin films prepared by spray pyrolysis. Journal of Non-Crystalline Solids, 352(3), 209-215. 2006

[65] Wang, Y., Brezesinski, T., Antonietti, M., & Smarsly, B. Ordered mesoporous Sb-, Nb-, and Ta-doped SnO_2 thin films with adjustable doping levels and high electrical conductivity. Acs Nano, 3(6), 1373-1378. 2009

[66] Pan, J., Shen, H., & Mathur, S. One-dimensional SnO_2 nanostructures: synthesis and applications. Journal of nanotechnology, 2012.

[67] Leite, E. R., Weber, I. T., Longo, E., & Varela, J. A. A new method to control particle size and particle size distribution of SnO_2 nanoparticles for gas sensor applications. Advanced materials, 12(13), 965-968. 2000

[68] Shanker, G., Prathap, P., Srivatsa, K. M. K., & Singh, P. Effect of balanced and unbalanced magnetron sputtering processes on the properties of SnO_2 thin films. Current Applied Physics, 19(6), 697-703. 2019

[69] Gordillo, G., Moreno, L. C., De la Cruz, W., & Teheran, P. Preparation and characterization of SnO2 thin films deposited by spray pyrolysis from $SnCl_2$ and $SnCl_4$ precursors. Thin Solid Films, 252(1), 61-66. 1994

[70] Jiang, J., Lu, Y., Kramm, B., Michel, F., Reindl, C. T., Kracht, M. E., et al. Nitrogen incorporation in SnO_2 thin films grown by chemical vapor deposition. physica status solidi (b), 253(6), 1087-1092. 2016

[71] Ikhmayies, S. J., & Ahmad-Bitar, R. N. An investigation of the bandgap and Urbach tail of vacuum-evaporated SnO_2 thin films. Renewable Energy, 49, 143-146. 2013

[72] Serin, T., Yildiz, A., & Serin, N. Electrical Properties of Polycrystalline SnO_2 Thin Films. Applied Physics Express, 4(12), 121101. 2011

[73] Zhang, X., Liu, X., Ning, H., Yuan, W., Deng, Y., Zhang, X., et al. Characterization studies of the structure and properties of Zr-doped SnO_2 thin films by spin-coating technique. Superlattices and Microstructures, 123, 330-337. 2018

[74] Talebian, N., & Jafarinezhad, F. Morphology-controlled synthesis of SnO_2 nanostructures using hydrothermal method and their photocatalytic applications. Ceramics International, 39(7), 8311-8317. 2013

[75] Sbeta, M., Atilgan, A., Atli, A., & Yildiz, A. Influence of the spin acceleration time on the properties of ZnO: Ga thin films deposited by sol–gel method. Journal of Sol-Gel Science and Technology, 86(2), 513-520. 2018

[76] Ozel, K., & Yildiz, A. SnO_2/ZnO/p-Si and SnO_2/TiO_2/p-Si heterojunction UV photodiodes prepared using a hydrothermal method. Sensors and Actuators A: Physical, 315, 112351. 2020

[77] Tao, Y., Fu, M., Zhao, A., He, D., & Wang, Y. The effect of seed layer on morphology of ZnO nanorod arrays grown by hydrothermal method. Journal of alloys and Compounds, 489(1), 99-102. 2010

[78] Ozel, K., & Yildiz, A. Comprehensive Understanding of the Role of Emitter Layer Thickness for Metal–Oxide–Semiconductors Based Solar Cells. IEEE Journal of Photovoltaics. 2021

[79] Benhaliliba, M., Benouis, C. E., Ayeshmariam, A., & Mouffak, Z. Light effect on IV and profile of C/ω-V and G/ω-V characteristics of In-doped SnO_2/Si heterojunction for photodiode applications. Optik, 206, 164032. 2020

[80] Ling, C., Guo, T., Lu, W., Xiong, Y., Zhu, L., & Xue, Q. Ultrahigh broadband photoresponse of SnO_2 nanoparticle thin film/SiO_2/p-Si heterojunction. Nanoscale, 9(25), 8848-8857. 2017

[81] Lee, S. J., Hwang, C. S., Pi, J. E., Yang, J. H., Byun, C. W., Chu, H. Y., et al. High-Performance Amorphous Multilayered ZnO-SnO_2 Heterostructure Thin-Film Transistors: Fabrication and Characteristics. Etri journal, 37(6), 1135-1142. 2015

[82] Baco, S., Chik, A., & Yassin, F. M. Study on optical properties of tin oxide thin film at different annealing temperature. Journal of Science and Technology, 4(1). 2012

[83] Xin, Y., Wang, X., Chen, Z., Weller, D., Wang, Y., Shi, L., et al. Polarization-sensitive self-powered type-II GeSe/MoS_2 van der Waals heterojunction photodetector. ACS applied materials & interfaces, 12(13), 15406-15413. 2020

[84] Neamen, D. A. Semiconductor physics and devices: basic principles. London: Mcgraw hill higher education, 2012.

[85] Hussain, B., Aslam, A., Khan, T. M., Creighton, M., & Zohuri, B. Electron affinity and bandgap optimization of zinc oxide for improved performance of ZnO/Si heterojunction solar cell using PC1D simulations. Electronics, 8(2), 238. 2019

[86] Ozel, K., & Yildiz, A. The potential barrier-dependent carrier transport mechanism in n-SnO_2/p-Si heterojunctions. Sensors and Actuators A: Physical, 113141. 2021

[87] Jäger, K. D., Isabella, O., Smets, A. H., van Swaaij, R. A., & Zeman, M. Solar Energy: Fundamentals, Technology and Systems. UIT Cambridge. 2016

[88] Ozel, K., & Yildiz, A. Estimation of maximum photoresponsivity of n-SnO_2/p-Si heterojunction-based UV photodetectors. physica status solidi (RRL)–Rapid Research Letters, 2100490, 2021

[89] Chauhan, K. R., & Patel, D. B. Functional nanocrystalline TiO_2 thin films for UV enhanced highly responsive silicon photodetectors. Journal of Alloys and Compounds, 792, 968-975. 2019

[90] Park, N., Sun, K., Sun, Z., Jing, Y., & Wang, D. High efficiency NiO/ZnO heterojunction UV photodiode by sol–gel processing. Journal of Materials Chemistry C, 1(44), 7333-7338. 2013

[91] Liu, H. Y., & Liu, G. J. Investigation of bandgap engineering of gallium zinc oxide-based ultraviolet photodetector by mist atmospheric pressure chemical vapor deposition. IEEE Transactions on Electron Devices, 66(5), 2256-2262. 2019

[92] Osi optoelectronics Retrieved September 10, 2021, from http://www.osioptoelectronics.com/application-notes/AN-Photodiode-Parameters-Characteristics.pdf

[93] Johnson, M. Photodetection and measurement: maximizing performance in optical systems, McGraw-Hill Education, 2003

[94] da Cunha, M. R. P., Amorim, D. R. B., Faria, G. C., Coutinho, D. J., & Faria, R. M. Analysis of electrical transients in the fourth quadrant of thin films photovoltaics: The case of organic bulk heterojunction solar cell. Solar Energy Materials and Solar Cells, 231, 111313. 2021

[95] Narzary, R., Maity, S., & Sahu, P. P. Coupled ZnO–SnO_2 Nanocomposite for Efficiency Enhancement of ZnO–SnO_2/p-Si Heterojunction Solar Cell. IEEE Transactions on Electron Devices, 68(2), 610-617. 2020

[96] Alsac, A. A., Yildiz, A., Serin, T., & Serin, N. Improved conductivity of Sb-doped SnO_2 thin films. Journal of Applied Physics, 113(6), 063701. 2013

[97] Cullity, B. D. Elements of X-Ray Diffraction (8th ed.), Addison-Wesley Publishing Company. 1978

[98] Prabakar, K., Venkatachalam, S., Jeyachandran, Y. L., Narayandass, S. K., & Mangalaraj, D. Microstructure, Raman and optical studies on Cd0. 6Zn0. 4Te thin films. Materials Science and Engineering: B, 107(1), 99-105. 2004

[99] Koksal, N. E., Sbeta, M., & Yildiz, A. GZO/Si photodiodes exhibiting high photocurrent-to-dark-current ratio. IEEE Transactions on Electron Devices, 66(5), 2238-2242. 2019

[100] Cheung, S. K., & Cheung, N. W. Extraction of Schottky diode parameters from forward current-voltage characteristics. Applied physics letters, 49(2), 85-87. 1986

[101] Liu, P., Cosentino, S., Le, S. T., Lee, S., Paine, D., Zaslavsky, A., et al. Transient photoresponse and incident power dependence of high-efficiency germanium quantum dot photodetectors. Journal of Applied Physics, 112(8), 083103. 2012

[102] Mukherjee, B., Zulkefli, A., Hayakawa, R., Wakayama, Y., & Nakaharai, S. Enhanced Quantum Efficiency in Vertical Mixed-Thickness n-ReS_2/p-Si Heterojunction Photodiodes. ACS Photonics, 6(9), 2277-2286. 2019

[103] Serin, T., Yildiz, A., Uzun, Ş., Çam, E., & Serin, N. Electrical conduction properties of In-doped ZnO thin films. Physica Scripta, 84(6), 065703. 2011

[104] Oshima, T., Okuno, T., & Fujita, S. UV-B sensor based on a SnO_2 thin film. Japanese Journal of Applied Physics, 48(12R), 120207. 2009

[105] Srikant, V., & Clarke, D. R. On the optical band gap of zinc oxide. Journal of Applied Physics, 83(10), 5447-5451. 1998

[106] Guang-Lei, T., Hong-Bo, H. E., & Jian-Da, S. Effect of microstructure of TiO_2 thin films on optical band gap energy. Chinese physics letters, 22(7), 1787. 2005

[107] Yang, Y. H., Chen, X. Y., Feng, Y., & Yang, G. W. Physical mechanism of blue-shift of UV luminescence of a single pencil-like ZnO nanowire. Nano letters, 7(12), 3879-3883. 2007

[108] Lv, Y., Xiao, W., Li, W., Xue, J., & Ding, J. Controllable synthesis of ZnO nanoparticles with high intensity visible photoemission and investigation of its mechanism. Nanotechnology, 24(17), 175702. 2013

[109] Chen, C. W., Chen, K. H., Shen, C. H., Ganguly, A., Chen, L. C., Wu, J. J., et al. Anomalous blueshift in emission spectra of ZnO nanorods with sizes beyond quantum confinement regime. Applied Physics Letters, 88(24), 241905. 2006

[110] Sannakashappanavar, B. S., Byrareddy, C. R., Kumar, P. S., & Yadav, A. B. Seed layer effect on different properties and UV detection capability of hydrothermally grown ZnO nanorods over SiO_2/p-Si substrate. Superlattices and Microstructures, 117, 503-514. 2018

[111] Samadpour, M. Improving the parameters of electron transport in quantum dot sensitized solar cells through seed layer deposition. RSC advances, 8(46), 26056-26068. 2018

[112] Faraz, S. M., Ashraf, H., Arshad, M. I., Hageman, P. R., Asghar, M., & Wahab, Q. Interface state density of free-standing GaN Schottky diodes. Semiconductor science and technology, 25(9), 095008. 2010

[113] Luo, L., Zhang, Y., Mao, S. S., & Lin, L. Fabrication and characterization of ZnO nanowires based UV photodiodes. Sensors and Actuators A: Physical, 127(2), 201-206. 2006

[114] Sani, S. R. Analysis of optoelectronic properties of TiO_2 nanowiers/Si heterojunction arrays. Chinese Physics B, 23(10), 107302. 2014

[115] Lee, J. Y., Choi, Y. S., Kim, J. H., Park, M. O., & Im, S. Optimizing n-ZnO/p-Si heterojunctions for photodiode applications. Thin Solid Films, 403, 553-557. 2002

[116] Ozel, K., & Yildiz, A. A Self-Powered Ultraviolet Photodetector with Ultrahigh Photoresponsivity (208 mA W^{-1}) based on SnO_2 Nanostructures/Si Heterojunctions. physica status solidi (RRL)–Rapid Research Letters, 2100085. 2021

[117] Ozel, K., & Yildiz, A. High-detectivity ultraviolet-B photodetector based on SnO_2 thin film/Si heterojunction. Semiconductor Science and Technology, 36(9), 095001. 2021

[118] Cao, R., Xu, J., Shi, S., Chen, J., Liu, D., Bu, Y., et al. High-performance self-powered ultraviolet photodetectors based on mixed-dimensional heterostructure arrays formed from NiO nanosheets and TiO_2 nanorods. Journal of Materials Chemistry C, 8(28), 9646-9654. 2020

[119] Al-Hardan, N. H., Jalar, A., Hamid, M. A., Keng, L. K., Ahmed, N. M., & Shamsudin, R. A wide-band UV photodiode based on n-ZnO/p-Si heterojunctions. Sensors and Actuators A: Physical, 207, 61-66. 2014

[120] Chen, R. S., Wang, W. C., Lu, M. L., Chen, Y. F., Lin, H. C., Chen, K. H., et al. Anomalous quantum efficiency for photoconduction and its power dependence in metal oxide semiconductor nanowires. Nanoscale, 5(15), 6867-6873. 2013

[121] Gong, Y., Yang, Z., Lari, L., Azaceta, I., Lazarov, V. K., Zhang, J., et al. Optimizing the Electronic Structure of In_2O_3 through Mg Doping for NiO/In_2O_3 p–n Heterojunction Diodes. ACS Applied Materials & Interfaces, 12(47), 53446-53453. 2020

[122] Zhao, Q., Wang, W., Carrascoso-Plana, F., Jie, W., Wang, T., Castellanos-Gomez, A., et al. The role of traps in the photocurrent generation mechanism in thin InSe photodetectors. Materials Horizons, 7(1), 252-262. 2020

[123] Zheng, L., Hu, K., Teng, F., & Fang, X. Novel UV–visible photodetector in photovoltaic mode with fast response and ultrahigh photosensitivity employing Se/TiO_2 nanotubes heterojunction. Small, 13(5), 1602448. 2017

[124] Zeng, L., Tao, L., Tang, C., Zhou, B., Long, H., Chai, Y., et al. High-responsivity UV-vis photodetector based on transferable WS_2 film deposited by magnetron sputtering. Scientific reports, 6(1), 1-8. 2016

[125] Wu, D., Jiang, Y., Zhang, Y., Li, J., Yu, Y., Zhang, Y., et al. Device structure-dependent field-effect and photoresponse performances of p-type ZnTe: Sb nanoribbons. Journal of Materials Chemistry, 22(13), 6206-6212. 2012

[126] Liu, Y., Wu, X., Guo, W., Li, M., Niu, X., Yao, J., et al. Self-powered and high responsivity photodetector based on a n-Si/p-GaTe heterojunction. Nanotechnology, 32(22), 225204. 2021

[127] Kumar, M., Rani, S., Vashistha, P., Pandey, A., Gupta, G., Husale, S., et al. Low bias operated, fast response SnSe thin film Vis-NIR photodetector on glass substrate using one-step thermal evaporation technique. Journal of Alloys and Compounds, 879, 160370. 2021

[128] Guo, D., Liu, H., Li, P., Wu, Z., Wang, S., Cui, C., et al. Zero-power-consumption solar-blind photodetector based on β-Ga_2O_3/NSTO heterojunction. ACS applied materials & interfaces, 9(2), 1619-1628. 2017

[129] Bhardwaj, R., Sharma, P., Singh, R., Gupta, M., & Mukherjee, S. High Responsivity $Mg_xZn_{1-x}O$ Based Ultraviolet Photodetector Fabricated by Dual Ion Beam Sputtering. IEEE Sensors Journal, 18(7), 2744-2750. 2018

[130] Martínez, D. T., Pérez, R. C., Delgado, G. T., & Ángel, O. Z. Structural, morphological, optical and photocatalytic characterization of ZnO–SnO_2 thin films prepared by the sol–gel technique. Journal of Photochemistry and Photobiology A: Chemistry, 235, 49-55. 2012

[131] Tharsika, T., Thanihaichelvan, M., Haseeb, A. S. M. A., & Akbar, S. A. Highly sensitive and selective ethanol sensor based on ZnO nanorod on SnO_2 thin film fabricated by spray pyrolysis. Frontiers in Materials, 6, 122. 2019

[132] Kim, J. H., Mirzaei, A., Kim, H. W., & Kim, S. S. Low power-consumption CO gas sensors based on Au-functionalized SnO_2-ZnO core-shell nanowires. Sensors and Actuators B: Chemical, 267, 597-607. 2018

[133] Xue, X. Y., Chen, Y. J., Wang, Y. G., & Wang, T. H. Synthesis and ethanol sensing properties of $ZnSnO_3$ nanowires. Applied Physics Letters, 86(23), 233101. 2005

[134] Yildiz, A., Cansizoglu, H., Turkoz, M., Abdulrahman, R., Al-Hilo, A., Cansizoglu, M. F., et al. Glancing angle deposited Al-doped ZnO nanostructures with different structural and optical properties. Thin solid films, 589, 764-769. 2015

[135] Chen, Q., Qian, Y., Chen, Z., Zhou, G., & Zhang, Y. Fabrication of ultrafine SnO_2 thin films by the hydrothermal method. Thin Solid Films, 264(1), 25-27. 1995

[136] Narzary, R., Phukan, P., Maity, S., & Sahu, P. P. Enhancement of power conversion efficiency of Al/ZnO/p-Si/Al heterojunction solar cell by modifying morphology of ZnO nanostructure. Journal of Materials Science: Materials in Electronics, 31(5), 4142-4149. 2020

[137] Elsaeedy, H. I., Qasem, A., Yakout, H. A., & Mahmoud, M. The pivotal role of TiO_2 layer thickness in optimizing the performance of TiO_2/p-Si solar cell. Journal of Alloys and Compounds, 867, 159150. 2021

[138] Pietruszka, R., Witkowski, B. S., Gieraltowska, S., Caban, P., Wachnicki, L., Zielony, E., et al. New efficient solar cell structures based on zinc oxide nanorods. Solar Energy Materials and Solar Cells, 143, 99-104. 2015